High temperature thermochemical energy storage using iron-manganese oxide particles in a packed-bed reactor

Marziyeh Hamidi

A thesis submitted for the degree of

Doctor of Philosophy at

The Australian National University

July 2019

Abstract

The rising demand for electricity coupled with concerns about globally increasing greenhouse gas emissions has prompted greater interest in using renewable energy sources. One of the main drawbacks of renewable energy sources is their intermittency. For instance, solar energy experiences regular daily and annual cycles due to the earth's rotation, motion and axis inclination which leads to variations in solar irradiance. Furthermore, solar energy is unavailable during cloudy weather. One particularly promising solution to the intermittency of solar energy is implementing thermochemical energy storage (TCES) technology in the future concentrated solar power (CSP) plants. This would help to achieve the primary objective of providing non-intermittent clean electricity.

In this thesis, a reactor packed with iron–manganese oxide particles is considered as the TCES system. First, the reduction reaction of particles is studied under non-isothermal conditions in argon and air atmospheres using a thermogravimetric analyzer (TGA). A shrinking core model along with a non-linear regression technique is used to model the thermal reduction of particles. Then, heat transfer of the reactor is studied when no chemical reaction occurs. The spatial temperature distribution in both axial and radial directions of a packed-bed reactor are measured experimentally. A two-dimensional, pseudo-homogeneous model is developed for the reactor, and effective thermal transport parameters are determined as functions of temperature by solving an inverse problem. Finally, these results are combined and used to describe the thermochemical performance of the particles in the packed-bed reactor during the reduction reaction. Results from the simulation are validated with the experimental data.

Declaration of authorship

Dr. Alicia Bayon of CSIRO Energy, Newcastle, assisted with the TGA–DSC experimental runs in chapter 4. Mr. Mark Wallace of the University of Colorado, Boulder, assisted with the material synthesis in section 3.2. Mr. Xiang Gao of the Australian National University, Canberra, assisted with BET surface area measurement in section 3.5. Ms. Linda McMorrow of the Australian National University, Canberra, assisted with ICP analysis in section 3.5.

Except where otherwise indicated, this thesis is my own original work. I certify the material in this thesis has not been previously published by others or submitted in whole or in part for the purpose of obtaining a degree from any university or tertiary education institution.

Marziyeh Hamidi

July 2019

Acknowledgments

I would like to thank Prof. Alan Weimer and Dr. Vincent Wheeler who have improved the quality of this research through their guidance, support, and criticisms. I would like to express my greatest appreciation to Prof. Kylie Catchpole, the chair of my PhD panel, for her massive and relentless support during my PhD journey.

I appreciate the support by Dr William Wong and his assistance with proofreading.

I want to thank the members of the Solar Thermal Group at ANU for their roles in helping me complete this body of work, in particular, Dr. John Pye, Dr. Peter Kreider, Dr. Charles-Alexis Asselineau, Dr. Mahesh Venkataraman, Mr. Johannes Pottas, and Dr. Juan Felipe Torres. The assistance provided by our support staff, specially Colin Carvolth and David Tychsen-Smith, is also gratefully acknowledged. In addition, I would also like to thank the many fellow students at for their help and advice along the way. In alphabetical order: E. Abbasi, F. Azimi, Z. Fusco, X Gao, A.R. Rahbari, A. Riaz, M. Taheri, and B. Wang, and J. Yeoh.
The technical advice by A/Prof. Takuya Tsuzuki and experimental data provided by Dr. Alicia Bayon have been vital for chapter 4 of this thesis.

Financial support from the Australian Renewable Energy Agency (ARENA) that was administrated by Prof Wojciech Lipinski is gratefully acknowledged.

List of publications and presentations

1. **M. Hamidi**, A. Bayon, V.M. Wheeler, P. Kreider, M.A. Wallace, T. Tsuzuki, K. Catchpole, A.W. Weimer, "Reduction kinetics for large spherical 2:1 iron–manganese oxide redox materials for thermochemical energy storage" *Chemical Engineering Science*, 201 (2019) 74-81
2. **M. Hamidi**, V.M. Wheeler, P. Kreider, K. Catchpole, A.W. Weimer, "Effective thermal conductivity of a bed packed with granular iron–manganese oxide for thermochemical energy storage" *Chemical Engineering Science*, 207 (2019) 490–494
3. **M. Hamidi**, V.M. Wheeler, Xiang Gao, J. Pye, K. Catchpole, A.W. Weimer, "Reduction reaction of iron-manganese oxide particles in a lab-scale packed-bed reactor for thermochemical energy storage" (under review, *Chemical Engineering Science*)
4. **M. Hamidi**, A. Bayon, M. Wallace, P. Kreider, V.M. Wheeler, T. Tsuzuki, K. Catchpole, A.W. Weimer, "Manganese–iron binary oxide for solar thermochemical energy storage", *2018 ICREN*, April 25-28 2018, Barcelona, Spain

5. **M. Hamidi**, A. Bayon, P Kreider, V.M. Wheeler, T. Tsuzuki, K. Catchpole, A.W. Weimer, "Solar Thermochemical Energy Storage Based on Iron–Manganese Oxide in a Packed-Bed Reactor", *2018 APSRC*, December 4-6, 2018, Sydney, Australia

Contents

List of Figures

List of Tables

Nomenclature

$A_r = 2\pi r \Delta z$, area normal to r direction (m^2)

$A_z = 2\pi r \Delta r$, area normal to z direction (m^2)

C_i , molar concentration of component i in the gas phase (mol/m^3)

$c_{p,g}$, specific heat capacity of the gas phase at constant pressure (J/kg.k)

$c_{p,s}$, specific heat capacity of the solid phase at constant pressure (J/kg.k)

D , reactor tube diameter (m)

D_{AB} , binary diffusivity for system A-B (m^2/s)

D_{eff} , effective diffusivity (m^2/s)

D_{im} , diffusivity of component i in the gas mixture (m^2/s)

d_p , particle diameter (m)

E , internal energy (J)

F_{21} , radiation shape factor (-)

F_E^* , radiation exchange factor (-)

H , reactor height (m)

ΔH_i , enthalpy of reaction (J/mol)

h_w , wall heat transfer coefficient ($W/m^2.K$)

h_{rs} , heat transfer coefficient for thermal radiation, solid surface to solid surface ($W/m^2.K$)

h_{rv} , heat transfer coefficient for thermal radiation, void space to void space ($W/m^2.K$)

j , molecular(diffusive) molar flux ($mol/ m^2.s$)

j' , convective molar flux ($mol/m^2.s$)

k_{eff} , effective thermal conductivity (W/m.K)

k_{eff}^r , effective thermal conductivity due to radiation (W/m.K)

k_g, thermal conductivity of the gas phase (W/m.K)

k_s, thermal conductivity of the solid phase (W/m.K)

k_c, thermal conductivity due to conduction (W/m.K)

k_r, thermal conductivity due to radiation (W/m.K)

M, molecular weight (g/mol)

p, total pressure (atm)

p_c, critical pressure (atm)

r_{O_2}, reaction rate of oxygen generation (mol/kg.s)

q, conductive heat flux (based on Fourier's law) (W/m^2)

q', convective heat flux (W/m^2)

q'', radiative heat flux (W/m^2)

R, universal gas constant (kJ/mol.K)

R, radius of cylindrical packed bed (m)

r, coordinate in the r direction (m)

r_i, reaction rate (mol/kg.s)

S, residual sum of squares

t, time (s)

T, temperature (K)

T_c, critical temperature (K)

T_{disc}, alumina disc temperature (K)

T_w, wall temperature (K)

u, gas velocity (m/s)

u^s, superficial gas velocity (m/s)

V, volume (m^3)

$\dot{V}$, volumetric gas flowrate (m^3/s)

y_i, measured experimental data point

$\hat{y}_i$, predictor data point

z, coordinate in the z direction (m)

α, reaction conversion (-)

ρ_g, mass density of the gas phase (kg/m^3)

ρ_s, mass density of the solid phase (kg/m^3)

ε_b, void fraction of the bed (m^3/m^3)

$\varepsilon_{r,w}$, emissivity of the wall (-)

$\varepsilon_{r,s}$, emissivity of the solid (-)

σ, Stefan–Boltzmann constant (W/m^2K^4)

Λ_f, dimensionless solid conductivity (-)

Abbreviations

ANU, Australian National University

B&B, Breitbach and Barthels correlation

CSP, concentrated solar power

CST, concentrated solar thermal

CU, University of Colorado Boulder

D&B, Deissler and Boegli correlation

DSC, differential scanning calorimetry

Fe, iron

ICP-AES, inductively-coupled plasma atomic emission spectrometer

IR, infrared radiation

K&S, Kunii and Smith correlation

LES, latent energy storage

MFC, mass flow controller

Mn, manganese

MS, mass spectrometer

ODE, ordinary differential equation

PCM, phase change material

PV, photovoltaic

SEM, scanning electron microscope

SES, sensible energy storage

TCES, thermochemical energy storage

TES, thermal energy storage

TGA, thermogravimetric analysis

XRD, X-ray diffraction

1 Introduction

Renewable energy sources such as wind and solar are unlimited with limited or no negative impact on the environment. Nevertheless, these energy sources have the issue of intermittency. A solution to the intermittency of solar energy is thermal energy storage which makes the solar source dispatchable and reliable on demand. At large scale, thermal energy storage is cheaper and more efficient than most electric storage systems. Among three types of thermal energy storage, sensible energy is the only one currently used in concentrated solar power (CSP) plants. However, this technology is expensive and requires huge amount of molten salts. With respect to the two other types of thermal energy storage for CSP technology, latent energy storage is at the prototype stage while thermochemical storage is still at the pending proof-of-concept. Packed-bed thermal storage systems are promising alternatives for molten salt tanks that can reduce storage costs and improve the development of solar energy.[1]

This research investigates thermochemical energy storage (TCES) in packed-bed reactors. Although TCES is less developed and presents higher technical complexity than sensible or latent energy storage, it has the advantage of having higher operational flexibility and higher energy density. In TCES, energy is kept in the chemical bonds of the molecules that are formed and decomposed in a reversible reaction. During the charging step, an endothermic reaction occurs using solar energy. Therefore, the thermal energy is converted and stored as chemical energy. In the discharging step, the reverse exothermic reaction takes place and the energy releases. The energy stored can be completely recovered if the reaction is fully reversible. This type of energy can be stored for a long time without heat loss concerns.

Redox reaction of iron–manganese oxide has been considered as the TCES system in this work. Both iron and manganese oxides are abundant, economical and non-toxic materials, making the mixture an acceptable candidate for energy storage in industrial TCES applications. The

binary system of iron–manganese oxide with a molar ratio of Fe/Me 2:1 forms the reactive and stable cubic spinel structure of $MnFe_2O_4$ during its reduction. This combination of manganese oxide and iron oxide has previously been used for chemical-looping combustion[2] and water splitting[3]. In this work, this mixture is investigated as a potential TCES material for the first time. The chemical reaction is as follows:

$$6(Mn_{0.33}Fe_{0.67})_2O_3(s)+\Delta H_r \leftrightarrow 4(Mn_{0.33}Fe_{0.67})_3O_4(s)+O_2(g), \quad (1.1)$$

The redox reaction of an iron–manganese oxide mixture involves thermal reduction of the oxide using concentrated solar irradiation, releasing oxygen, followed by oxidation. Obtaining a reaction rate equation for these types of reactions is challenging as the chemical process occurs through a range of mechanisms and intermediate stages. Considering a general form for the reaction rate combined with experimental thermogravimetric analysis (TGA) provides for a robust method to investigate the reaction kinetics. In TGA experiments, sample material is heated by a furnace with a desired temperature program and its mass change is measured during the reaction using a microbalance. Using TGA data, one can identify reaction kinetics and evaluate the reversibility of the reaction.

A lab-scale packed-bed reactor heated with an IR furnace is designed and fabricated to simulate a solar driven reduction reaction. Packed-bed reactors have been employed in solar-driven high temperature solid–gas reactions[4, 5] and thermal decomposition processes[6 7, 8]. Understanding the behavior of a metal oxide redox reaction in a packed-bed reactor supports the design and operation of commercial scale CSP reactors and advances the field of solid-gas heterogeneous reactions and TCES.

The temperature profile is an important consideration when designing a packed-bed TCES reactor since high temperatures drive local endothermic reactions as well as thermal losses.

Thermal models of the packed bed are generally based on a pseudo-homogeneous approach where the solid and fluid are considered one continuous, single phase. Pseudo-homogeneous models have been shown to accurately predict the temperature profile in packed-bed reactors while using an effective thermal conductivity and a wall heat transfer coefficient as the adjustable parameters.[9,10]

1.1 Motivation

This doctoral thesis contributes to a broader research project sponsored by Australian Renewable Energy Agency (ARENA).[11] The latter project consists of four tasks which are shown in Figure 1.1. The goal of task 1 is to obtain manganese oxide-based mixed metal oxide materials capable of undergoing thousands of redox cycles without significant reduction in their reaction performance and physical and chemical stability. In task 2, the aim is to develop a solar thermochemical reactor to realize the reduction step. A 1 kW_{th} solar thermochemical reactor prototype will be designed, fabricated and evaluated in the high flux solar simulator to obtain realistic prediction of solar reduction reactor at a pilot plant level. An optical field will be designed in task 3 to match the reduction reactor at the pilot plant level. A techno-economic analysis of the solar power plant with the integrated high-temperature solar thermal energy storage system via manganese-based metal oxide redox cycling will be conducted in task 4. To fulfil this ARENA project, the Australian National University (ANU), the University of Colorado Boulder (CU), and IT Power (ITP) are collaborating together in several aspects.

Task 1 of the project is accomplished by collaboration of CU and ANU. CU evaluated the effect of Al_2O_3, ZrO_2, and Fe_2O_3 as secondary metal oxides to increase structural robustness and chemical reactivity of manganese oxide.[12] They used spray drying and intensive mixing methods to synthesize the particles. Then, they tested the mixed metal oxide particles in a thermogravimetric analyser (TGA) over six consecutive redox cycles to evaluate the impact of

the secondary metal oxides. Their study showed that iron oxide with manganese oxide in a molar ratio of 2:1 synthesized via intensive mixing method outperformed the other tested mixed-metal oxides. The oxidation kinetics of this mixture was also investigated in their work.[12]

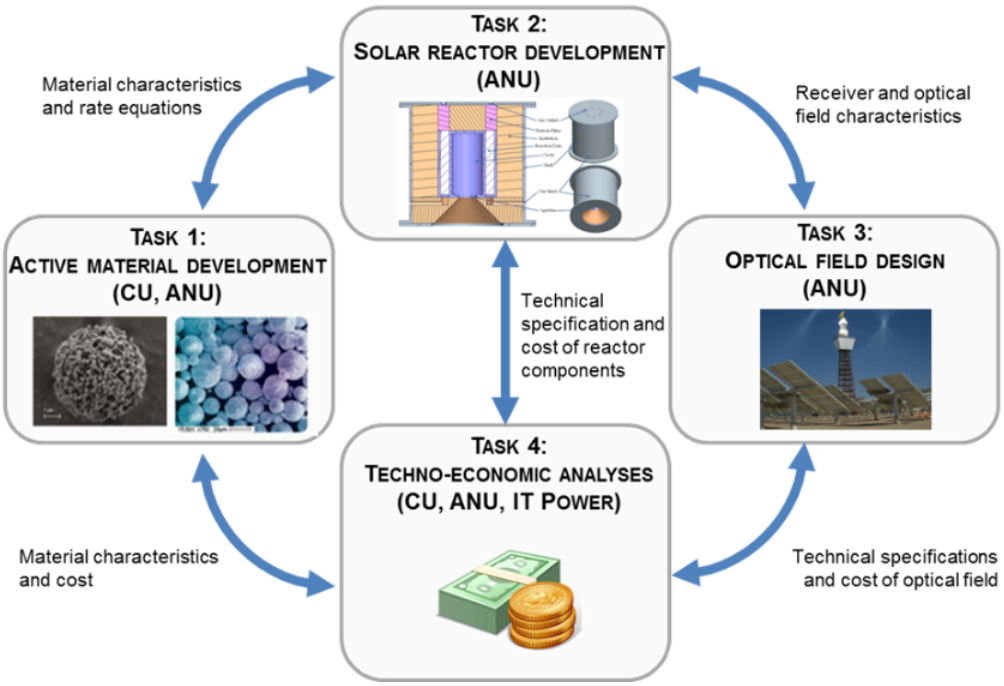

Figure 1.1 ARENA project tasks[11]

This doctoral research continues the work done by CU in task 1 of the ARENA project. This thesis contributes to the ARENA project by 1) investigating the reduction kinetics of the iron-manganese oxide particles (with molar ratio of 2:1) using TGA and 2) obtaining a realistic prediction of the solar driven reduction reactor using a packed-bed reactor heated by an IR furnace.

1.2 Objectives

The goals of this research are to 1) understand the reduction reaction of iron-manganese oxide, and 2) obtain a realistic prediction of the thermochemical performance of the metal oxide in a lab-scale direct packed-bed reactor. The tasks to achieve these goals include:

- thermodynamic modelling of Fe-Mn-O system to theoretically identify operating conditions of the reduction reaction
- investigating the reduction kinetics of iron-manganese oxide particles using a TGA under air and inert atmospheres
- physical and chemical characterization of the material before and after the reaction
- determination of the reduction enthalpy using Differential Scanning Calorimetry (DSC)
- design and fabrication of a lab-scale packed-bed reactor heated by an IR furnace
- experimental measurement of the spatial temperature distribution in both axial and radial directions of the packed bed under steady state and transient conditions
- heat transfer modelling of the packed-bed reactor and obtaining the effective heat transfer parameters of the bed
- investigating the thermochemical performance of the mixed-metal oxide material in the packed-bed reactor while the exit gas is analysed using a mass spectrometer

1.3 Structure of thesis

In this thesis, background information about solar energy, thermochemical energy storage and kinetics of solid–gas reactions is first given in chapter 2.

In chapter 3, FactSage7 software package is first used to identify the effect of temperature, total pressure and partial pressure of oxygen on the equilibrium composition of metal oxide material in the redox reactions. Then, the stability and cyclability of metal oxide is examined using TGA.

Finally, the physical and chemical characteristics of the material at oxidized and reduced states are investigated.

In chapter 4, kinetics of the reduction step for the redox process are studied. Kinetic analysis is performed by non-linear regression applied to non-isothermal data recorded using thermogravimetric analysis (TGA) at four heating rates along with differential scanning calorimetry (DSC). The thermal reduction is carried out in both argon and air atmospheres.

In chapter 5, a lab-scale packed-bed reactor is designed and fabricated to obtain a realistic prediction of the reduction reaction of the metal oxide. The reactor is directly heated by an IR furnace. The experimentally measured temperature in both axial and radial directions of the bed is presented. A two-dimensional transient heat transfer model considering conductive, convective and radiative heat transfer is developed. The governing equations, initial and boundary conditions are presented in this chapter. Effective thermal transport parameters are determined as functions of temperature—at fixed particle size, porosity and Reynolds number—by solving an inverse problem using the model at steady-state. The measured parameters are validated with the transient experimental data and are compared with reported correlations for effective thermal conductivity.

In chapter 6, the reaction rate and effective thermal parameters obtained from chapters 4 and 5 are used to describe the thermochemical performance of metal oxide in the packed-bed reactor. The reactor modelling results are compared with the experimental data. The primary experimental data are the concentration of oxygen at the outlet of the reactor which is measured using mass spectrometry.

Chapter 7 is a summary of this research findings and their contribution to the field. The prospects of the field are also briefly discussed in this chapter.

2 Literature review

In this chapter, background information on solar energy, thermochemical energy storage (TCES), packed bed reactors in TCES, and kinetics in solid–gas reactions is given.

2.1 Solar energy

The rising demand for energy coupled with concerns about globally increasing greenhouse gas emissions has prompted greater interest in using renewable energy sources. The current energy industry is based on sources such as oil, natural gas, and coal while a renewable energy industry would likely be based on wind, biofuel, geothermal and solar sources. Solar energy is an abundant resource that is technically capable of delivering the world's energy needs with harvesting the irradiance on only 1% of the earth's surface with a 10% efficiency.[13]

Two promising families of solar technologies are photovoltaic (PV) and concentrated solar thermal (CST). PV technology is the direct conversion of sunlight into electricity by means of solar panels. PV devices are easy to design, require low maintenance and can give outputs from microwatts to megawatts. These are the reasons why they can be used as the power source in a broad range of applications such as calculators, watches, buildings, satellites, and power plants. Thus, the demand for PV is rapidly increasing, alongside lowering costs.[13]

In 1954, the first practical PV solar cell for converting sunlight into electrical power was invented at RCA and Bell Laboratories with a conversion efficiency of approximately 6%. The importance of this invention was quickly recognized and the technology was rapidly developed for powering satellites from 1958.[13] In the early stages of this technology (1960s and 1970s), the energy required for the manufacturing was more than the energy delivered by the cell during its entire lifetime. Dramatic improvements have occurred since then: efficiency has improved, cell lifetime has increased, energy payback periods and the cost of the panels have decreased.[13]

PV is now a cost-effective technology. While theoretical efficiency of a solar cell with a single junction is approximately 33%, efficiency of up to 44% has been achieved in the laboratory for multijunction solar cells.[13] The price of solar panels has also come down from $30/W to $0.5/W over the last three decades.[13]

The photovoltaic effect of semiconductors is used in solar cell technology. When the semiconductor is exposed to sunlight, the photons are absorbed by the valence electron of atom and the energy level of the electron increases. If the energy gain is more than the band gap of the semiconductor, the electron jumps into the conduction band of the atom where it can move freely. This electron movement generates electron-hole pairs in the semiconductor. In PV solar cells, using p-n junction results in channeling the free electrons through an external resistance before they recombine with the holes. This phenomenon leads to the generation of electricity.[13]

Solar radiation is a form of thermal radiation having a particular wavelength distribution. Its intensity depends on atmospheric conditions, time of the year, and the angle of radiation incidence on the surface of the earth. Solar irradiation is 1395W m^{-2} at the outer layer of atmosphere when the earth is at its closest distance to the sun. However, not all of this energy reaches the earth's surface, because of strong absorption by water vapour and carbon dioxide in the atmosphere. Furthermore, the solar irradiance reduces on the earth's surface due to the atmospheric content of dust and other pollutants.[14] Therefore, for solar thermal power plants or other high-temperature solar thermal applications, there would be an essential requisite of employing optical concentration devices.[15] In concentrating solar thermal technology, solar radiation is collected, concentrated and then stored in form of high-temperature thermal energy. This thermal energy can be used for a variety of applications such as chemical processes, cooling and heating, and electricity generation. In most CST technologies, the thermal energy can be stored and dispatched when needed. [16]

The commercially available CST technologies can be categorized into two groups based on the type of the collector; linear-focusing technologies and point-focusing technologies. Linear optical concentrators track the sun by rotating on a single axis. This type of concentrator reflects the solar radiation onto a linear receiver. Parabolic troughs and linear Fresnels are two dominant systems of this technology. Point focus concentrators, on the other hand, require two-axis sun tracking. This type of concentrator reflects the solar radiation onto a single point. Parabolic dishes and central receiver systems (also known as solar towers) are the two dominant concentrators of this technology.[16]

Figure 2.1 shows schematic diagrams of these four CST systems.

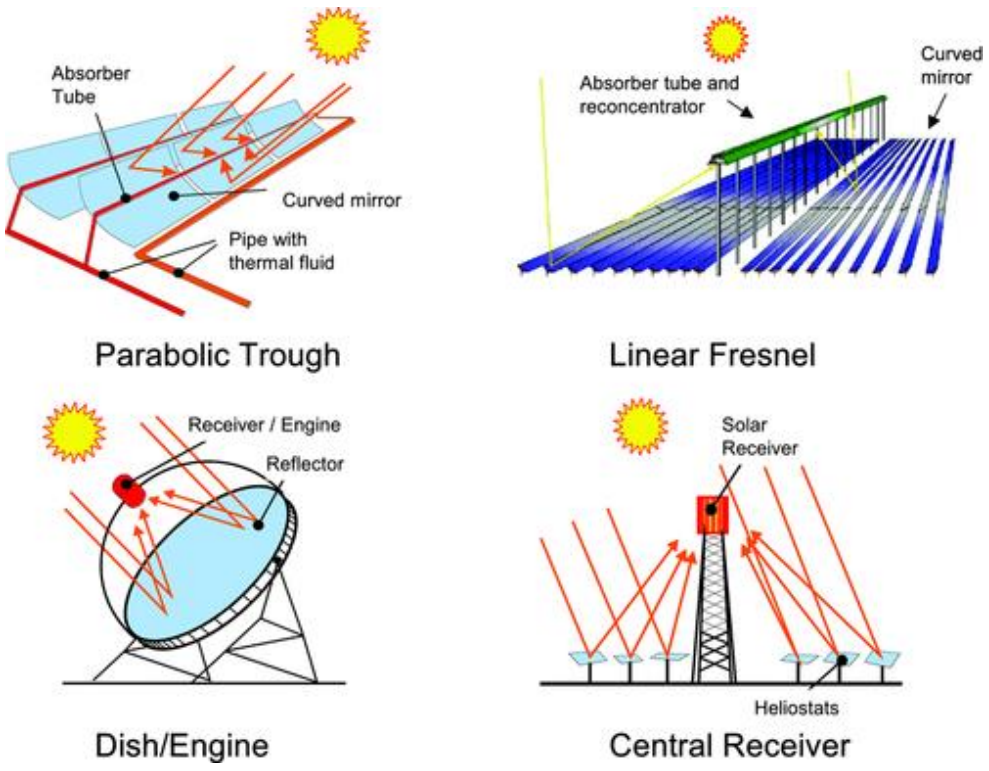

Figure 2.1 Schematic diagram of CST systems[15]

A parabolic trough is composed of a parabolic-trough-shaped reflector and a receiver tube that is installed at the focus of the reflector. Each reflector concentrates the solar radiation on its

receiver tube. A heat transfer fluid circulates through the tube and stores the thermal energy in the form of latent or sensible heat. The stored thermal energy can later be used in industrial processes or in electricity generation. Parabolic troughs can achieve concentration ratios of up to 80 suns (equal to 80 kW/m^2, assuming solar flux to be 1000 W/m^2) and deliver useful energy up to 398 °C.[17]

A linear Fresnel is composed of many long reflectors and a linear receiver that is installed parallel to the reflectors' rotational tracking axis. Unlike the parabolic trough, the linear Fresnel's receiver is fixed in space. The reflectors rotate independently at different angles and concentrate the solar radiation onto the fixed receiver. The working fluid inside the receiver can reach temperatures up to 350 °C. This technique is commercially less mature compared to parabolic troughs.[17]

A parabolic dish is made of one or several small reflectors attached to a dish frame. The reflectors concentrate solar radiation into a receiver that is fixed at the focal point of the dish. The dish frame and the receiver move bi-axially together in the way that the optical axis of the system is always pointing to the sun. The heat transfer fluid in the receiver captures the high temperature thermal energy. Parabolic dishes have the highest concentration ratios (up to 4000), highest optical efficiencies, and highest overall conversion efficiencies among all CST technologies.[17]

A central receiver consists of a field of two-axis, independently tracking reflectors that concentrates solar radiation onto an elevated central receiver. The receiver is fixed in place, avoiding the need for energy transport networks and allows for more cost-effective investment. However, the fixed position of the receiver means that the reflectors do not directly point at the sun, which causes reduction of solar radiation on the reflectors. The energy absorbed by the receiver is transferred to a working fluid or storage material and stored in the form of thermal

energy. A central receiver achieves concentration ratios of up to 1000 and provides fluid temperatures of 1000 °C.[17]

2.2 Thermal energy storage

One of the main drawbacks of renewable energy sources is their intermittency. For instance, solar energy has regular daily and annual cycles due to the earth's rotation, motion and axis inclination which leads to variations in solar irradiance. Furthermore, direct solar energy is unavailable during cloudy weather. Owing to its intermittency, solar energy fails to meet the requirements of a viable energy source that can be used in industrial plants. Thermal energy storage (TES) is believed to be a prospective and valid option to overcome this limitation of solar energy.[13, 18]

In a CST power plant, sunlight is converted into thermal energy prior to generation of electricity. Compared to other renewable energy technologies such as wind and photovoltaic, CST has the distinct advantage of integrating cost-effective TES into its system. The integration of TES systems into CST power plants extends the operation of a solar power plant, providing more versatility and dispatchable operation to the plant and even reducing the levelized cost of electricity.

TES systems are divided into three types: sensible energy storage (SES), latent energy storage (LES) and thermochemical energy storage (TCES).

2.2.1 Sensible energy storage

In SES technology, the thermal energy is stored and released through temperature change of a storage material. The storage capacity depends on the specific heat of the material and follows the formula below

$$Q = m.\int_{T1}^{T2} C_p.\mathrm{d}T\,, \tag{2.1}$$

where m is the mass of the material, C_p is the specific heat capacity of the material and $\mathrm{d}T$ is the temperature change.[19]

The storage materials in SES technology can be in a solid, liquid, or gaseous state and are usually kept in a storage tank with high thermal insulation. Water is a SES medium that has both residential and industrial applications.[20] Oil, molten salt, liquid metal, and concrete are the main materials used in the CST field. Molten salt has a general melting point of 200 °C and its operation temperature is usually below 600 °C. Temperatures lower than melting point lead to the solidification and inactivation of the entire system. Therefore, heat tracking is usually required to avoid this issue, although this technology causes intense energy loss. Furthermore, molten salt becomes a corrosive fluid at high operational temperatures which causes equipment damage. Liquid sodium is another storage material with a melting point of about 98 °C that has high thermal and hydraulic properties. This material does not have the solidification problem faced by molten salt. Although liquid sodium has been successfully applied into CSP plants, low thermal capacity and safety aspects of using this material warrant further improvements.[19] A number of sensible TES materials along with their operating temperatures, specific heat, and energy storage density are presented in Table 2.1.

Table 2.1 Sensible energy storage materials[19]

Material	**Temperature range (°C)**		**Average specific capacity (kJ/kg.K)**	**Energy storage density (kW.h/m^3)**
	Cold side	Hot side		
Synthetic oil	250	350	2.3	57
Silicone oil	300	400	2.1	52
Liquid nitrite	250	450	1.5	152
Liquid nitrate	265	565	1.6	249

Liquid sodium	270	530	1.3	80
Sand rock + mineral oil	200	300	1.3	60
Reinforced concrete	200	400	0.85	100
Cast iron	200	400	0.56	160
Silica refractory	200	700	1	150

2.2.2 Latent energy storage

In LES, energy is stored and released based on a phase transition process. This technology is also known as phase-change energy storage and the storage medium is called phase change material (PCM). The phase transition can be between solid–liquid, solid–solid, or liquid–gas states. For CST applications, the transition between solid and liquid is mostly considered due to its low volumetric expansion and high volumetric energy density compared to the other forms of the transitions. The energy storage capacity of LES technology is calculated via the following formula

$$Q = m.L\,, \tag{2.2}$$

where m is the mass of the material and L is latent heat per unit of mass.[19]

Phase change materials can be organic or inorganic. Organic PCMs, such as paraffin and fatty acids, are combustible and relatively expensive. Salt hydrates and ice are examples of inorganic PCMs. Salt hydrates have high latent heat but can phase separate and have a large degree of subcooling. Selection of PCMs depends on their application but, in general, they must meet a number of criteria such as; thermodynamic properties (high latent heat, high thermal conductivity, and appropriate transition temperature), kinetic properties (low undercooling degree and high crystallization rate), physical properties (high density, small volume variations, and low vapor pressure), and chemical properties (nontoxic, not combustible, noncorrosive,

and long term stability). Suitable PCMs should also have economic feasibility and availability.[19]

LES systems are able to release thermal energy at a constant temperature and create an isothermal operation for the power block which leads to a higher power cycle efficiency. Low thermal conductivity, low rate of energy release and storage, and lack of thermal stability are the main disadvantages of this system. [21]

2.2.3 Thermochemical energy storage

In TCES, energy is stored based on the chemical properties of the storage materials unlike SES and LES systems where it is stored based on their physical properties. In this technology, energy is kept in the chemical bonds of the molecules that are formed and decomposed in a reversible reaction during the charge and discharge stages. This technology is less developed and presents higher technical complexity than sensible or latent energy storage. However, it has higher operational flexibility as numerous reversible reactions covering a wide range of temperatures are available. High energy density and long-term seasonal storage are other advantages of this system. TCES hasn't reached a proven design for commercial scale.[20, 22] A comparison between the advantages and disadvantages of three TES systems are shown in Figure 2.2. A number of technical characteristics of TES systems are also presented in Table 2.2.

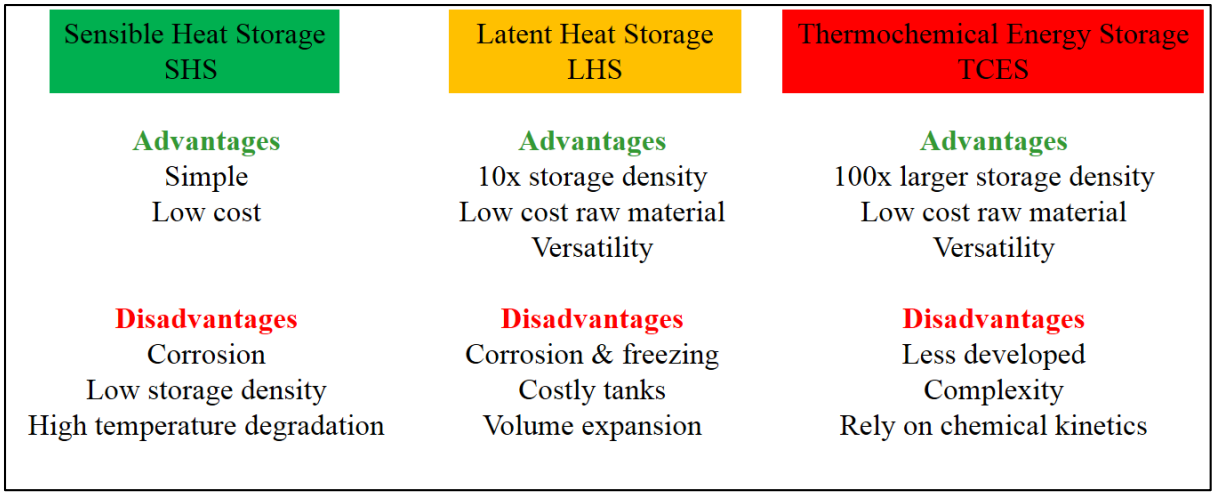

Figure 2.2 Comparison of three TES systems

Table 2.2 Technical characteristics of TES systems[23]

Storage technology	Thermal efficiency (%)	Energy cost (USD/k.Wh)	Durability (years)	Energy storage density (k.Wh/m^3)
SES	50-90	0.1-13	10-30+	25
LES	75-90	10-56	10-30+	100
TCES	75-100	8-100	10-30+	~500

TCES cycle uses a reversible reaction to store energy. This cycle consists of two processes, charging and discharging. During the charging process, an endothermic reaction occurs using the concentrated solar energy. Therefore, the thermal energy is converted and stored as chemical energy. In the discharging process, the reverse exothermic reaction takes place and the energy is released. The stored energy can be completely recovered if the reaction is fully reversible. This type of energy can be stored indefinitely without losses as waste heat. TCES reversible reactions can be generally describe by

$$A \leftrightarrow B + C \ (\Delta H > 0). \tag{2.3}$$

Reactant A absorbs thermal energy and decomposes into B and C components during the charging step. Later in the discharging step, B and C react with each other and release the

thermal energy.[23] Long term storage and transport of this energy is possible by storing the B and C products. The basic principle of a TCES system is illustrated in Figure 2.3.

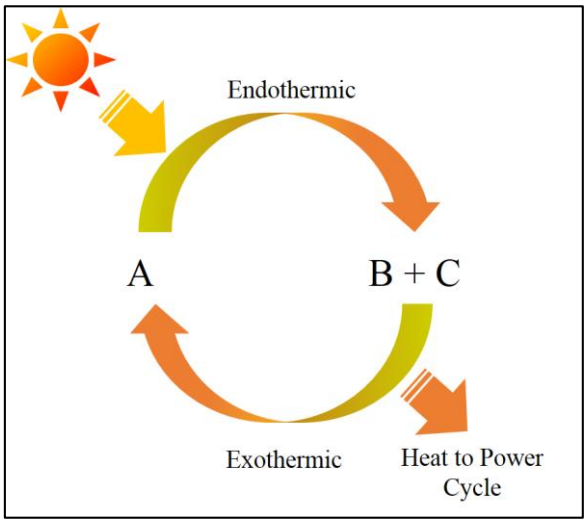

Figure 2.3 Schematic diagram of a TCES system

The total energy stored in a TCES system can be defined by

$$Q = mC_p\Delta T + mL + m\Delta H\ , \tag{2.4}$$

where m is the mass of the material, C_p is the specific heat capacity of the material, L is latent heat per unit of mass, and ΔH is the heat of reaction.[22]

The candidate materials for high-temperature thermochemical energy storage must have key criteria such as low material cost, storage feasibility, cycle robustness, non-toxic, non-corrosive, non-flammable, environmentally friendly, long term stability, suitable thermodynamics, fast reaction kinetics, complete reaction reversibility, appropriate reaction temperature, high reaction enthalpy, and no side reactions or by-products.[20, 24]

A wide range of materials have been studied as storage media for TCES technology.[20, 24, 25] A classification of TCES candidate materials investigated so far is shown in Figure 2.4. Although many of these materials are available for energy storage, not all of them are suitable for TCES.

For instance, some are harmful to human such as $PbCO_3$. Metal sulfates produce toxic and corrosive gases, so there will not be any further investigation on this group. A number of metal hydroxides and carbonates (such as $Mg(OH)_2$, $Mn(OH)_2$, $ZnCO_3$, and $MgCO_3$) have reaction temperatures lower than the suitable temperature range for TCES. In carbonates, hydroxides, and organic systems, the components require separation, which represents another obstacle for the storage system. Furthermore, ammonia energy storage systems suffer from high pressure requirements and high exergy losses.[23]

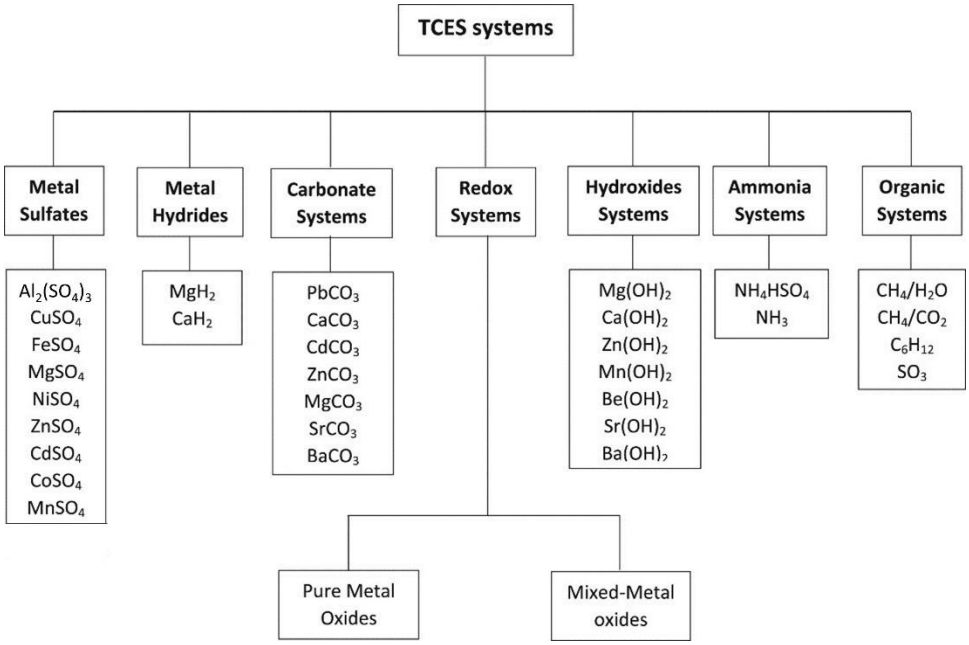

Figure 2.4 TCES systems[26]

A redox system is one of the most promising means of converting thermal energy from CST to chemical energy via reduction-oxidation reactions.[18] This system has less technical issues compared to the other TCES systems. It also has advantages such as high operating temperature, high energy density, no need for gas storage and products separation, and comparatively smaller environmental impact.[23] The general formula for reduction and oxidation reactions of metal oxides is

$$M_xO_{y+z}(s) + \Delta H_r \leftrightarrow M_xO_y(s) + z/2\,O_2(g) \quad (2.5)$$

where M is a metal. In the first step, the endothermic reduction reaction occurs where the metal oxide reduces at high temperatures. To discharge the stored energy off-sun, the reduced metal oxide is re-oxidized in air and heat is released.

A metal oxide redox reaction was first proposed for energy storage applications by Wentworth and Chen in 1976.[27] Later that year, Simmons implemented theoretical calculations for barium oxide as a TCES material which was followed by an in-depth experimental study of this material. In another study, Fahim and Ford determined the reaction kinetics of the barium oxide redox reaction in 1983.[28] Copper oxide was the next metal oxide that was investigated as TCES material by Chadda et al. in 1989.[29] For the next two decades, very few studies were published, probably due to reduction in the fossil fuel prices. However, the interest in the metal redox reactions for TCES has increased again in the last six years.[23]

Two main technologies that are used for characterization of redox reactions are thermogravimetric analysis (TGA) and differential scanning calorimetry (DSC). TGA records the mass change of the sample while the reaction is taking place at high temperatures. Using TGA data, one can calculate the reaction kinetics and check the reversibility of the reaction. DSC is a thermo-analytical technique that can measure the capacity of metal oxides for energy storage and release. Some other methodologies frequently applied in TCES studies are; X-ray diffraction (XRD) for determining crystalline structure of metal oxides, scanning electron microscope (SEM) for examining microstructure of the material, and FactSage for investigating the thermodynamics of reactions.

Pure and mixed metal oxides can be used for redox TCES. While producing pure metal oxides is easier, mixed oxides have the advantages of better reversibility and lower cost.[23] Pure metal oxides have been intensively investigated for TCES applications. The most promising ones are

BaO_2/BaO,[25, 28, 30] Co_3O_4/CoO,[31-38] Mn_2O_3/Mn_3O_4,[38-43] Fe_2O_3/Fe_3O_4,[24, 44] CuO/Cu_2O[25, 45] and perovskite-based[46-49] systems.

Manganese oxide is an abundant and inexpensive material with low toxicity that is considered as one of the most promising metal oxides for TCES purposes.[20, 24, 50] The manganese-oxygen system has five different stable forms: MnO_2, α-Mn_2O_3, β-Mn_2O_3, Mn_3O_4 and MnO. In this system, oxygen is released with increasing temperature, leading to reduced manganese oxide compounds:

$$MnO_2 \xrightarrow{1} Mn_2O_3 \xrightarrow{2} \alpha\text{-}Mn_3O_4 \xrightarrow{3} \beta\text{-}Mn_3O_4 \xrightarrow{4} MnO \qquad (2.6)$$

Table 2.3 shows a summary of conditions for manganese oxide reduction reactions under nitrogen, air and oxygen atmospheres.

Table 2.3 Manganese oxide reduction reactions in nitrogen, air and oxygen obtained with FactSage7[51]

	$T_{transition}$ (°C)			Δh(kJ kg^{-1})
	N_2	Air	O_2	
MnO_2/Mn_2O_3	280-350	430	467	481
Mn_2O_3/β-Mn_3O_4	700	870	963	214
α-Mn_3O_4/β-Mn_3O_4	1173	1173	1174	80
β-Mn_3O_4/MnO	1450	1580	1580	897
Slag	1625	1580	1580	

The first reduction step is not considered for thermochemical storage purposes as no re-oxidation of Mn_2O_3 into MnO_2 has been observed at ambient pressure.[44] Furthermore, the reaction temperature of Mn_3O_4 into MnO is too high for TCES applications. Therefore, only the reaction of Mn_2O_3 into Mn_3O_4 has the potential to be used for thermochemical energy storage. Cycle stability of Mn_2O_3/Mn_3O_4 redox couple has been widely investigated recently.

Carrillo studied the effect of the initial particle size,[39] Co doping,[40] Fe doping[42] and Fe–Cu co-doping[41, 43] on cycle stability, energy storage capacity and redox hysteresis of this couple. Their results show that the addition of iron to manganese oxide enhances the re-oxidation rate, increases energy storage capacity and decreases redox hysteresis. Thermodynamic studies of the Mn–O[52-55] and Fe–Mn–O systems[2, 56, 57] have also been reported in the literature to predict the equilibrium composition of solid phases as a function of temperature.

Fe_2O_3/Fe_3O_4 is another promising redox couple for TCES. The main advantages of this system are in its abundance, low cost, and high energy storage density of about 560 J g^{-1} [58]. The studies on this material for energy storage are very limited. In a TGA experimental study, Andre et al. reported that reduction temperature of Fe_2O_3 to Fe_3O_4 is 1145 °C and 1361 °C under inert and air atmospheres, respectively. They also found that the oxidation reaction can reach 92% conversion. In another work at lower oxidation temperature of 900 °C, lower conversion of 80% was reported.[59] Strong sintering has been reported for this material after 3 redox cycles.[24]

None of the pure metal oxide systems are ideal for high temperature energy storage due to limitations that each one has. For instance, some may have high energy storage density and reaction temperature but slow kinetics and high cost, while others may have low cost and low energy density. A solution to overcome these shortcomings and enhance the performance of the storage material is by mixing metal oxides together. The material mixing can improve reaction reversibility and cycling stability, adjust reaction temperature, enhance reaction kinetics, and limit the issue of sintering. High-temperature TCES materials are likely to become more economical using this method.[23, 26]

A summary of reported reaction temperature ranges and energy storage densities for various pure and mixed metal oxide systems is shown in Figure 2.5. The temperature ranges include theoretical and experimental reduction and oxidation temperatures. The energy density ranges

also cover both the theoretical and practical data reported in the literature. The changes in reaction temperatures and energy densities are due to variations in chemical and physical properties as well as the experimental conditions. The majority of the tested redox cycles have reaction temperatures in the range of 600 °C to 1100 °C. Pure iron oxide has the highest operating temperature followed by iron oxide doped with cobalt oxide. In terms of the energy storage density, cobalt, copper and iron oxide systems are the most reactive ones. Therefore, adding these metal oxides to other systems can increase the overall energy storage of the system. For commercial scale applications, the economical perspective of the material should be considered as well. For instance, cobalt oxide is expensive (32*1000 USD/metric tonne in December 2019) and costs six times more than iron oxide.

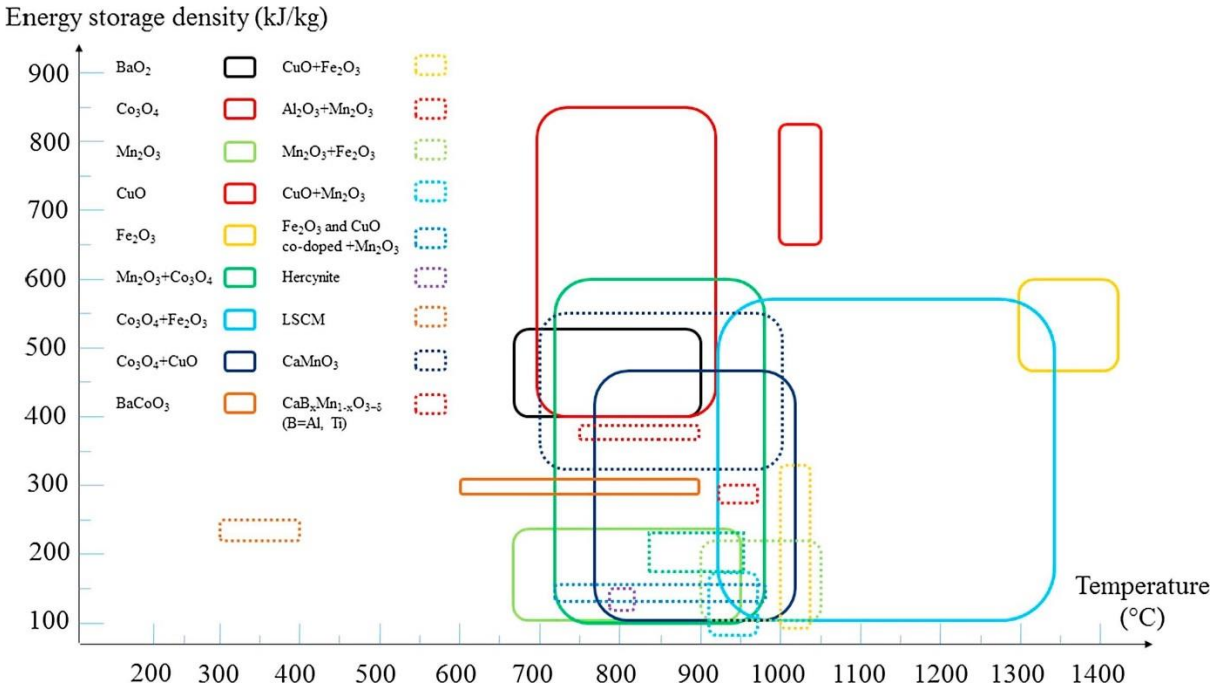

Figure 2.5 Reaction temperatures and energy storage densities for metal oxide systems[23]

In TCES technology, the heating system and the reactor design have two types; direct and indirect. In the indirect heating system, heat is first absorbed by a heat transfer fluid. A heat exchanger is needed in this system to transfer the heat from the heat transfer fluid to the reactant.

This heating system usually has high exergy losses because of the temperature difference between the reactant and the fluid. In a direct solar TCES system, the reactant is directly heated in the receiver. The receiver and the endothermic chemical reactor are basically the same devices in this system. For metal oxide redox systems, the direct heating system has advantages over the indirect heating system. For example, the reactants can easily reach high temperatures due to being heated directly. Furthermore, there is no need for a heat exchanger in this system since air can be used as both the reactant and the heat transfer fluid. Figure 2.6 shows schematic diagrams of direct and indirect heating systems in TCES technology.

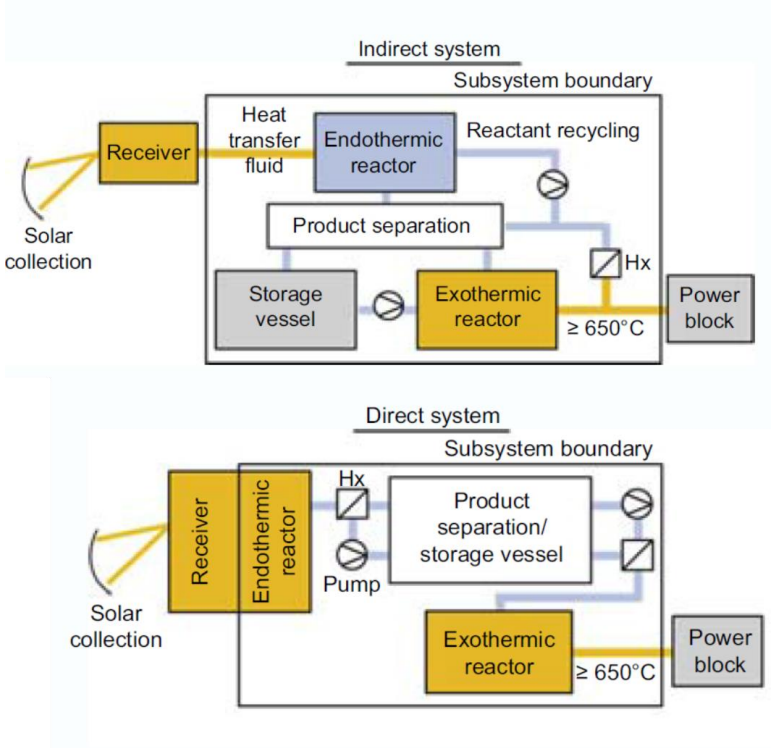

Figure 2.6 Schematic diagrams for direct and indirect heating systems in high temperature TCES [22]

Several reactor types have been considered and tested for the direct TCES system. Among them, packed-bed reactors have been used more than others due to their relatively simple design and operation. However, this type of reactor suffers from high pressure drop and poor heat and mass transfer. The aspect ratio of the reactor, physical properties of the particles, and the shape

and size of the material have been reported as the parameters affecting energy storage of the system. Rotary kilns are another type of reactor considered for TCES. Low sintering has been reported in this reactor due to the continuous movement of the material. Fluidized-bed reactors, cascade reactors, and moving packed beds are other types of reactors that have been considered for energy storage. In general, an ideal reactor should have a number of criteria such as; low pressure drop, high heat and mass transfer, low energy consumption, suitable cost, and simple design and operation.[23]

TCES technology can be applied not only in power plants for electricity generation but also in high temperature industries as a heat recovery system. In a power generation system, TCES provides the required heat for CSP plants, helping to maintain a stable electricity output. In industrial processes, TCES can be used for waste heat recovery. Adding TCES to the industrial processes not only decreases the CO_2 emissions, but is also energy saving and cost effective compared to the traditional industrial plants.[18]

2.3 Packed-bed reactors in TCES

Thermochemical reactors facilitate chemical reactions and utilize the reaction heat. While many studies have focused on constructing and modeling of low temperature thermochemical reactors[60], few studies on high temperature thermochemical reactors, including experimental tests and modeling of lab-scale reactors, have been carried out.[61] Packed-bed reactors have been employed in solar-driven high temperature solid-gas reactions[4, 5] and thermal decomposition processes[6 7, 8]. Recent experimental studies have considered this type of reactor as a TCES component for integration with a concentrated solar power plant.[61] For instance, Wokon et al.[62] employed a packed-bed reactor for an experimental study of charging and discharging of TCES materials. In another work, Preisner et al.[63] used this type of reactor to identify chemical and physical stability of the TCES materials over 30 cycles.

The temperature profile is an important consideration when designing a packed-bed TCES reactor since high temperatures drive local endothermic reactions as well as thermal losses. Models of the packed bed behavior are generally based on a pseudo-homogeneous approach where the solid and fluid are considered one continuous, single phase. Pseudo-homogeneous models have been shown to accurately predict the temperature profile in packed-bed reactors while using an effective thermal conductivity and a wall heat transfer coefficient as the adjustable parameters.[9,10] However, there are only a few studies on packed-bed heat transfer at high temperature conditions where thermal radiation becomes dominant.[64] For this case, the thermal transport within the bed is more complex than at lower temperatures and involves: radiation heat transfer between the surfaces of particles, conduction heat transfer between the particles due to physical contact at points on the surfaces, conduction heat transfer through the gas and solid phases, and the effects of convection heat transfer via the fluid. Although the phenomena involved are complex, employing an effective thermal conductivity based on a simple Fourier law has been shown to be effective.[65]

2.4 Kinetics in solid–gas reactions

An understanding of reaction rates and how the reaction rate is influenced by different parameters is essential for successful reactor modelling and development. Reaction kinetics along with mass and heat transfer phenomena are employed to describe the behavior of the storage reactor in TCES technology. For metal oxide redox reactions, understanding both the reduction and oxidation steps is critical. Reduction and oxidation of metal oxides are solid–gas reactions, also known as solid–state reactions. For that reason, this section is allocated to the study of reaction kinetics in solid–gas reactions.

The general objective of the analysis and prediction of reactions is to develop a description of the reaction progress that is valid for any operational conditions. Measuring changes in physical

and chemical properties of the sample on heating or cooling as a function of time leads to derivation of kinetic models which gives us the reaction rate. Kinetic studies of solid–gas reactions can be conducted using thermogravimetric analysis (TGA) based methods or techniques based on flow reactor data. In TGA experiments, sample material is heated by a furnace with a desired temperature program and its mass change is measured during the reaction by a microbalance. Kinetic parameters are then derived from these data. For the flow reactor method, the setup might be a packed-bed (gas is passed over the solid) or a fluidized-bed reactor (particle–gas flow passes the reactor). In flow reactors, many factors can influence the kinetic parameters. These include process conditions, heat and mass transfer limitations, physical and chemical heterogeneity of the sample and experimental errors. For that reason, a mathematical model and computer simulation need to be developed to model the mass and energy balance (and, if applicable, the momentum balance) equations for gas and solid phases in the reaction zone. Experimental factors such as detector time lag and the dispersion and mixing of gases in the line between the exit of the flow reactor and the gas analyzer also need to be taken into consideration during modeling.[66] Furthermore, the effect of mass diffusion needs to be accounted in the model with the purpose of obtaining intrinsic kinetics of the redox reaction. This will ensure the applicability of the kinetic model to new reactors and process designs.

TGA is experimentally easier and requires less modelling compared to flow reactors. As a result, TGA analysis is used in this doctoral thesis as the main method to identify reaction kinetics of the metal oxide. TGA is an excellent method in identifying potential reaction mechanisms for solid–state reactions. The instrument consists of a heating chamber, a microbalance, and a temperature measuring system. While sample material is heated by a furnace with a desired temperature program, the instrument records mass change traces and

sample temperature as a function of time. A schematic diagram of a TGA equipment is shown in Figure 2.7.

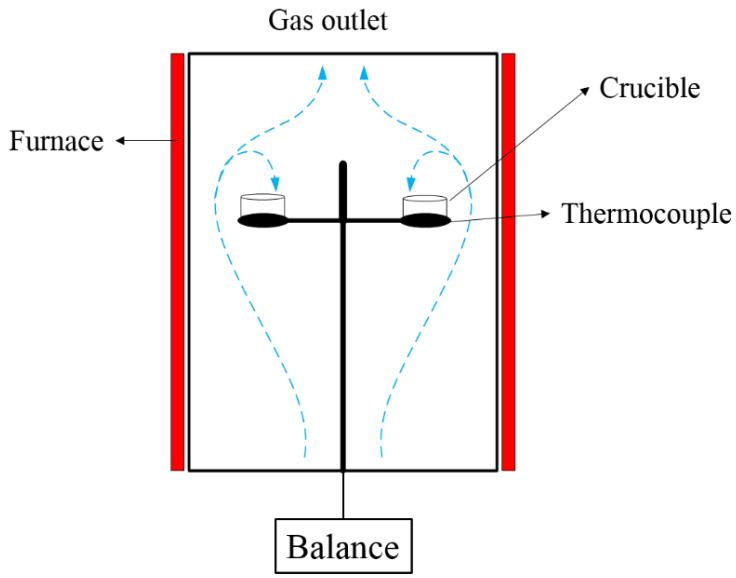

Figure 2.7 Schematic diagram of a thermogravimetric device

TGA data can be obtained via two experimental approaches; isothermal and non-isothermal methods. The isothermal method is based on maintaining the sample at a constant temperature and obtaining a set of conversion-time points for each temperature. The non-isothermal method employs a heating rate (usually a constant heating rate) to raise the temperature. The main disadvantage of the isothermal method for high temperature reactions is that the heat-up time is long, which means that a significant extent of conversion might be reached before the isothermal regime sets in.

This part of the thesis focuses on deriving a reaction rate equation for solid–gas processes based on experimental TGA data. The reaction rate will be valid for any thermal treatment, be it isothermal, linear non-isothermal or any other non-isothermal treatment. Nevertheless, the experimentally determined kinetic parameters are appropriate to be called “effective”,

"apparent", "empirical" or "global". This is because that they can be different from the "intrinsic" parameters which are based on reaction rate that is not affected by mass transfer limitations.[67] To obtain the reaction kinetics as close as possible to intrinsic kinetics, it is desirable to select the experimental conditions such that the chemical reaction becomes the controlling step of the process.

2.4.1 Reaction rate equation

For solid–gas reactions, obtaining the reaction rate equation is not easy since these reactions occur through a range of mechanisms and intermediate stages. Considering a general form for the reaction rate is optimal for identifying kinetics. This general form is a product of three functions

$$\frac{\mathrm{d}\alpha}{\mathrm{d}t} = k(T)\, f(\alpha) h(P), \tag{2.7}$$

where t is time, T is temperature, α is conversion, and P is pressure. For a gravimetric measurement, conversion (also called extent of reaction) is defined by

$$\alpha = \frac{m_i - m_t}{m_i - m_f}, \tag{2.8}$$

where m_i, m_t, and m_f are initial sample mass, sample mass at time t, and sample mass at the completion of the reaction, respectively.

In equation (2.7), $k(T)$ is the kinetic constant and depends only on temperature, $f(\alpha)$ is the reaction model and is a function of just conversion, and $h(P)$ is the pressure dependence function. The pressure dependence term is usually ignored in solid–gas kinetics and the majority of kinetic methods consider the reaction rate as a function of only temperature and conversion,

$$\frac{\mathrm{d}\alpha}{\mathrm{d}t} = k(T)\, f(\alpha). \tag{2.9}$$

The kinetic constant is typically given by Arrhenius equation

$$k(T) = A\exp\left(-\frac{E}{RT}\right), \tag{2.10}$$

where *A* is the pre-exponential factor (also called frequency factor), *E* is the activation energy, and *R* is the universal gas constant. The pre-exponential factor and activation energy are usually called Arrhenius parameters.[68] Combining equations (2.9) and (2.10) yields

$$\frac{\mathrm{d}\alpha}{\mathrm{d}t} = A\exp\left(-\frac{E}{RT}\right) f(\alpha). \tag{2.11}$$

Equation (2.11) is applicable to isothermal temperature programs, non-isothermal temperature programs, or even the actual sample temperature. For linear non-isothermal treatment (constant heating rate), this equation is usually written based on the heating rate

$$\beta\frac{\mathrm{d}\alpha}{\mathrm{d}T} = A\exp\left(-\frac{E}{RT}\right) f(\alpha), \tag{2.12}$$

where $\beta = \frac{\mathrm{d}T}{\mathrm{d}t}$ is the constant heating rate.

The reaction rate equation can also be reported based on an integral form. By integrating equation (2.12):

$$g(\alpha) \equiv \int_0^{\alpha} \frac{\mathrm{d}\alpha}{f(\alpha)} = A\int_0^{t} \exp\left(-\frac{E}{RT}\right)\mathrm{d}t \ , \tag{2.13}$$

where $g(\alpha)$ is the integral form of the kinetic rate equation. Equation (2.13) is the foundation for most of the kinetic analysis integral methods. This equation can be employed for any

temperature programs that have the temperature as a function of time. For the processes with constant heating rate, where the sample temperature does not deviate significantly from the reference temperature, the independent variable of time in equation (2.13) is usually replaced with temperature using the heating rate value β

$$g(\alpha) = \frac{A}{\beta}\int_0^T \exp\left(-\frac{E}{RT}\right)\mathrm{d}T\,. \tag{2.14}$$

The integral part in the above equation has no analytical solution. Therefore, a number of approximation and numerical integration methods are offered to deal with this problem.

From the computational point of view, the aim of kinetic analysis of thermally stimulated processes is to establish a mathematical relationship between the reaction rate, conversion, and temperature. The most straightforward method is to determine the kinetic triplet which is the pre-exponential factor A, activation energy E, and reaction model $f(\alpha)$ and replace them in equation (2.11), (2.12) or (2.14). Each of these kinetic triplet components has its own fundamental theoretical concept; E is associated with the energy barrier, A with the frequency of vibrations of the activated complex, and $f(\alpha)$ with the reaction mechanism.[67]

In this part, we first investigated possible reaction models in solid–state kinetics. Then, we introduce a model-fitting method to determine the kinetic triplet. This technique will be used in chapter 5 to investigate the reaction kinetics of iron–manganese oxide particles. Other kinetic computational techniques including isoconversional methods, Kissinger method, the compensation effect technique, and master plots are described in appendix A of this thesis.

2.4.2 Reaction models in solid–gas kinetics

Most of the reaction models proposed for solid–gas reactions have been developed based on certain mechanistic assumptions. Notably, some are empirical-based and do not have

mechanistic meaning.[69] Reaction models can be classified based on the kinetic curves or mechanistic assumptions.

In kinetic curve classification, reaction models have three types; accelerating, decelerating, and sigmoidal. This classification is based on the shape of the reaction profiles which is described as conversion or time derivative of conversion, versus time or temperature. This type of model classification is recognized mainly for isothermal processes where the kinetic curves depend only on the reaction and not the temperature. For non-isothermal data, the kinetic curves are usually in sigmoidal profiles since both $k(T)$ and $f(\alpha)$ change at the same time.[67, 69]

In accelerating models, the reaction rate increases continuously as the conversion increases. The reaction rate reaches its maximum value at the end of the process. The reaction model is usually described with a power-law equation

$$f(\alpha) = n\alpha^{(n-1)/n}, \tag{2.15}$$

where n is a constant.

In decelerating models, the reaction rate decreases as the conversion increases. The reaction rate has its maximum value at the beginning of the process. The most common example of these models is a reaction-order model

$$f(\alpha) = (1-\alpha)^n, \tag{2.16}$$

where n is the order of the reaction.

In sigmoidal models, the first and second halves of the reaction represent the accelerating and decelerating behaviors, respectively. The reaction rate reaches its maximum value at an intermediate stage of the process. A typical example of this behavior is Avrami-Erofeev models[67]

$$f(\alpha) = n(1-\alpha)[-\ln(1-\alpha)]^{(n-1)/n}. \quad (2.17)$$

Sestak and Berggren suggested a mathematical equation that represents all reaction models in a single expression

$$f(\alpha) = \alpha^m (1-\alpha)^n (-\ln(1-\alpha))^p, \quad (2.18)$$

where m, n and p are constants. By considering different values for these constants, any model can be represented.

Reaction models can also be classified based on mechanistic assumptions, which divide models into nucleation, geometrical contract, diffusion, and reaction order.[69] Table 2.4 shows the most commonly used mathematical models for each reaction mechanism. Although these solid–gas kinetic models are based on the experimental data fitting on complex mathematical equations, they also have theoretical meanings that describe the mechanisms involved in the reaction.

Table 2.4 kinetic models in the solid–gas reactions [69, 70]

Reaction model	**code**	$f(\alpha)$	$g(\alpha)$
Nucleation models			
Power law	P2/3	$2/3\alpha^{-1/2}$	$\alpha^{3/2}$
Power law	P2	$2\alpha^{1/2}$	$\alpha^{1/2}$
Power law	P3	$3\alpha^{2/3}$	$\alpha^{1/3}$
Power law	P4	$4\alpha^{3/4}$	$\alpha^{1/4}$
Avrami-Erofeev	A2	$2(1-\alpha)\left[-\ln(1-\alpha)\right]^{1/2}$	$\left[-\ln(1-\alpha)\right]^{1/2}$
Avrami-Erofeev	A3	$3(1-\alpha)\left[-\ln(1-\alpha)\right]^{2/3}$	$\left[-\ln(1-\alpha)\right]^{1/3}$
Avrami-Erofeev	A4	$4(1-\alpha)\left[-\ln(1-\alpha)\right]^{3/4}$	$\left[-\ln(1-\alpha)\right]^{1/4}$

Diffusion models			
1-D diffusion	D1	$1/2\,\alpha^{-1}$	α^2
2-D diffusion	D2	$\left[-\ln\left(1-\alpha\right)\right]^{-1}$	$(1-\alpha)\ln(1-\alpha)+\alpha$
3-D diffusion (Jander)	D3	$\frac{3(1-\alpha)^{2/3}}{2[1-(1-\alpha)^{1/3}]}$	$\left[1-(1-\alpha)^{1/3}\right]^2$
3-D diffusion (Ginstling–Brounshtein)	D4	$\frac{3}{2[(1-\alpha)^{-1/3}-1]}$	$1-2/3\alpha-(1-\alpha)^{2/3}$
Reaction order models			
Zero order	F0	1	α
First order(Mampel)	F1	$1-\alpha$	$-\ln(1-\alpha)$
Second order	F2	$(1-\alpha)^2$	$(1-\alpha)^{-1}-1$
Third order	F3	$(1-\alpha)^3$	$1/2[(1-\alpha)^{-2}-1]$
Geometrical contraction models			
Contracting cylinder	R2	$2(1-\alpha)^{1/2}$	$1-(1-\alpha)^{1/2}$
Contracting sphere	R3	$3(1-\alpha)^{2/3}$	$1-(1-\alpha)^{1/3}$

2.4.3 Model fitting methods

Model fitting methods compute Arrhenius parameters for a specific reaction model. Since the estimated Arrhenius parameters are inevitably tied up with the considered reaction model, one of the most important steps in model fitting is employing the appropriate reaction model. The master plot techniques (described in appendix A) are sometimes used to pick the best reaction model for the model fitting methods.

All model fitting approaches involve minimizing the difference between the experimental data and modelling results. Minimization can be accomplished by employing linear or non-linear

regression methods. Non-linear regression is more accurate than linear regression in many ways, but it needs initial estimates for Arrhenius parameters. The linear regression method is usually used to find the initial values for non-linear regression. Thereafter, the non-linear regression is employed to achieve the ultimate values of Arrhenius parameters.

Linear model fitting makes use of linear regression techniques. The reaction rate equation needs to be converted to a linear form in this method. One of the popular linear model fitting methods which is based on an approximation for the temperature integral in equation (2.14) is the Coats-Redfern method

$$\ln\left(\frac{g(\alpha)}{T^2}\right) = \ln\left[\left(\frac{AR}{\beta E}\right)\left(1-\frac{2R\bar{T}}{E}\right)\right] - \frac{E}{RT}. \tag{2.19}$$

Plotting $\ln(\frac{g(\alpha)}{T^2})$ versus $1/T$ gives the activation energy and the pre-exponential factor. The main problem with the Coats-Redfern method is that different reaction models are able to fit the experimental data well while the calculated Arrhenius parameters are crucially different.[71] Although this method is unable to analyze the reaction kinetics accurately, many papers have been published using this method due to its simplicity.[72]

Non-linear model fitting makes use of non-linear regression techniques. The method of least squares which minimizes the summed square of residuals is usually used in non-linear regression

$$\min(SSE) = \sum_{i=1}^{n}(y_i - \hat{y}_i)^2 , \tag{2.20}$$

where n is the number of data points, y_i is an experimental data point, and $\hat{y}_i$ is a predictor data point. Considering the assumption that the reaction model is independent of the heating

rate, all the TGA experimental data under different heating rates can be fitted simultaneously using this technique. Therefore, unique values of E and $\ln A$ for a specific reaction function can be obtained for the reaction under different heating rates.

2.4.4 Conversion calculation

The reaction rate equation is obtained when the kinetic triplet (E, A and $f(\alpha)$) is determined. For experimental data with constant heating rate, the rate equation can be defined in two different forms, differential form (equation (2.12)) and integral form (equation(2.14)). To find the value of conversion for a given temperature (or time), the reaction rate equation must be solved. Depending on which form of the reaction rate is used, different methods can be employed.

When the reaction rate is in its differential form, ordinary differential equation (ODE) solvers can be used. Although this method is fast compared to the integral methods, it has a few obstacles. For instance, in some reaction functions when the conversion approaches 1, ODE solvers do not converge properly and they give imaginary values for conversion. The other problem with ODE solvers is the requirement for an initial value for conversion at the initial state. This value can be considered zero when the initial state is a temperature lower than the reaction temperature.

When the reaction rate equation is defined based on the integral form, the integral part in the right-hand side of equation (2.14) has to be calculated first. Numerical integration or an approximation method (such as equation(A.26)) can be used in this regard. Then, values of $g(\alpha)$ are calculated for each temperature. Finally, the conversion can be computed based on the reaction mechanism and the correlation between $g(\alpha)$ and conversion (see Table 2.4).

3 Material synthesis and characterization [1]

3.1 Introduction

None of the pure metal oxide systems are ideal for high temperature TCES due to limitations that each one has. For instance, manganese oxide (Mn_2O_3/Mn_3O_4) is an inexpensive material, reacts at 948 °C and has a moderate reaction enthalpy of 184 J g^{-1} [42] (under air atmosphere with total pressure of 100 kPa), but its re-oxidation reaction is slow[24]. On the other hand, iron oxide (Fe_2O_3/Fe_3O_4) with a relatively high reaction enthalpy of 560 J g^{-1} [58] (under air atmosphere with total pressure of 100 kPa) and fast reaction kinetics, has a considerably higher reduction temperature (1392 °C) and deactivates due to sintering[24].

Recently, Fe/Mn binary metal oxide systems have been proposed to improve on the performance of pure Fe and Mn metal oxides, providing for more efficient active redox materials. Block and Schmücker identified an iron–manganese oxide system as a high potential active material for thermochemical energy storage. [24] Furthermore, the effect of incorporation of Fe into manganese oxide on the redox reaction has been explored by Carrillo et al.[42] Based on their thermal analysis, doping manganese oxide with 20% Fe had the most rapid oxidation reaction and highest enthalpy among the rest of the Fe/Mn ratios that they investigated. In another work, they proposed rate law models for reduction and oxidation reactions of that iron–manganese oxide system.[73] In 2017, Wokon et al. selected iron–manganese oxide with Fe/Mn ratio of 1:3 as a suitable material for their thermochemical storage reactor.[62, 74] Recently, the effect of Fe addition to Mn-based oxide was studied by simultaneous thermogravimetric

[1] material in this chapter along with chapter 4 has been published in: M. Hamidi, A. Bayon, V.M. Wheeler, P. Kreider, M.A. Wallace, T. Tsuzuki, K. Catchpole, A.W. Weimer, "Reduction kinetics for large spherical 2:1 iron–manganese oxide redox materials for thermochemical energy storage" Chemical Engineering Science, 201 (2019) 74-81

analysis and calorimetry. The results showed that adding amounts of Fe more than 15% increased the reversibility and cyclability of the mixture.[75]

The binary system of iron–manganese oxide with the molar ratio of Fe/Me 2:1 forms the reactive and stable cubic spinel of $MnFe_2O_4$ during its reduction. This combination of manganese oxide and iron oxide has previously been used for chemical-looping combustion (CLC) applications because of its capability to release considerable amounts of oxygen.[2, 76, 77] It has also been considered an active material in water splitting to produce hydrogen.[3] However, this mixture has not been investigated as a potential TCES material.

In this work, iron–manganese oxide particle with the molar ratio of Fe/Me 2:1 is proposed as a potential TCES material. The synthesis process of the particles, equilibrium composition analysis of the material, cyclability of the redox reaction, and physical and chemical properties of the particles are described in this chapter.

3.2 Material synthesis

Granular iron–manganese oxide powder was synthesized at the University of Colorado Boulder, by mixing Mn_3O_4 (US Research Nanomaterials) and Fe_2O_3 (Sigma Aldrich) powders (both < 30μm particle diameter) with an Fe/Mn molar ratio of 2:1, together in an Eirich intensive mixer, using corn starch, for 1.5 minutes at a mixer rotor speed of 7.5 m s^{-1} and a mixer pan speed of 30 Hz. Subsequently, 50 wt% maltodextrin solution organic binder was added at the same mixer rotation settings, and the contents were allowed to mix for 1 additional minute after liquid addition was complete. Following liquid addition and mixing, the mixer rotor speed was increased to 25 m s^{-1} and held for 1 minute, facilitating the granulation of the particles. Particles were then recovered from the mixer and dried over a kiln vent for 24 hours. After drying, the particles were calcined in air using a clamshell furnace at 850 °C for 12 hours to burn away

organic binders. After calcination, particles were sieved to gain a cut of 0.5-1 mm. The Eirich intensive mixer as well as the prepared particles with the diameter size between 0.5 to 1 mm are shown in Figure 3.1.

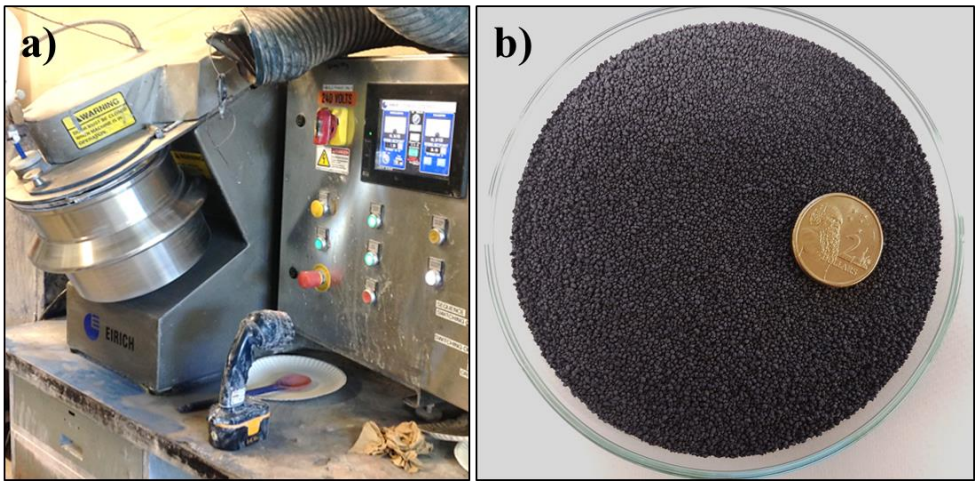

Figure 3.1 Eirich intensive mixer (at the University of Colorado, Boulder) and the prepared iron–manganese oxide particles

3.3 Thermodynamic analysis

FactSage[78] thermochemical software is used to identify the effects of temperature and partial pressure of oxygen on the equilibrium composition of the mixed metal oxide. The FactPs and FTmisc databases are used, along with the FToxid database for oxides and solid solutions. Figure 3.2 shows the calculated phase diagram for the Mn-Fe-O system under inert and air atmospheres. The total pressure is 1 atm for both cases. Four solid phases are considered in this system; cubic spinel $(Fe,Mn)_3O_4$, tetragonal spinel $(Mn,Fe)_3O_4$, corundum $(Fe,Mn)_2O_3$ and bixbyite $(Mn,Fe)_2O_3$. The slag (molten oxide) phases are included in calculations but are not discussed here since they appear at temperatures much higher than our operational temperatures. As can be seen, the behaviour of the mixed oxide strongly depends on the system composition. The ratio of Fe/Mn in the proposed mixture is 2 to 1, therefore Mn/(Mn+Fe) is equal to 0.33. The vertical dashed lines on the figures identify this ratio.

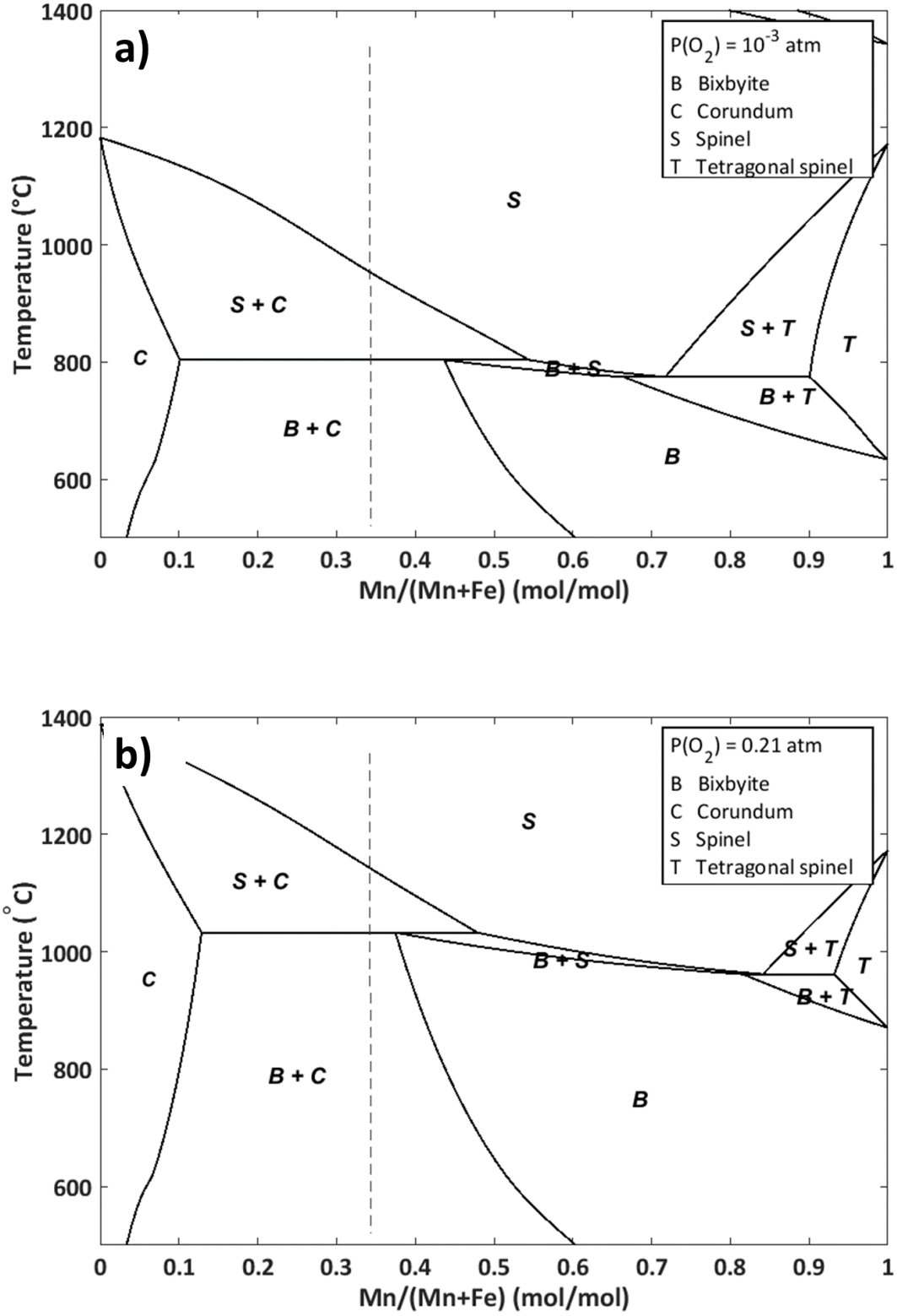

Figure 3.2 Mn-Fe-O phase diagram in a) inert and b) air atmosphere at 1atm

In the proposed mixture, bixbyite and corundum phases are favoured at lower temperatures for both inert and air atmospheres. Upon increasing the temperature, the bixbyite phase (Mn^{3+}, Fe^{3+})$_2O_3$ that has a higher amount of Mn compared to the corundum phase, becomes a spinel solution (Mn^{2+}, Fe^{2+})(Mn^{3+}, Fe^{3+})$_3O_4$. Further increasing the temperature, the corundum phase (Fe^{3+}, Mn^{3+})$_2O_3$ (Fe_2O_3 dissolving Mn^{3+}) also becomes a spinel solution. The reason that the bixbyite phase reduces to the spinel before the corundum phase can be explained by the fact that manganese oxide has a lower reduction temperature than iron oxide. The transition temperatures are not the same for different atmospheres. Under the inert atmosphere, bixbyite and corundum become spinel at 800 °C and ~950 °C, respectively. The first phase transition occurs at ~1000 °C and the second one completes at 1140 °C for the air atmosphere.

3.4 Stability and cyclability of the material

Stability and cyclability are key factors of metal oxide candidates for redox reactions in TCES technology. The capability of the synthesized iron-manganese oxide particles to withstand several charge/discharge cycles is tested by carrying out 10 redox cycles in a TGA instrument. Air with gas flow rate of 100 ml min^{-1} is used in this experiment. In each cycle, the sample (35 mg of oxidized iron-manganese oxide particles) is heated to 1200 °C (T_{max}) and cooled to 650 °C (T_{min}) with a heating rate of 10 °C min^{-1}. A 90 min dwell is used at the oxidation step with the aim of reaching the complete conversion. Figure 3.3 shows the results. It can be observed that the synthesized iron–manganese oxide particles present redox reversibility, stability and cyclability.

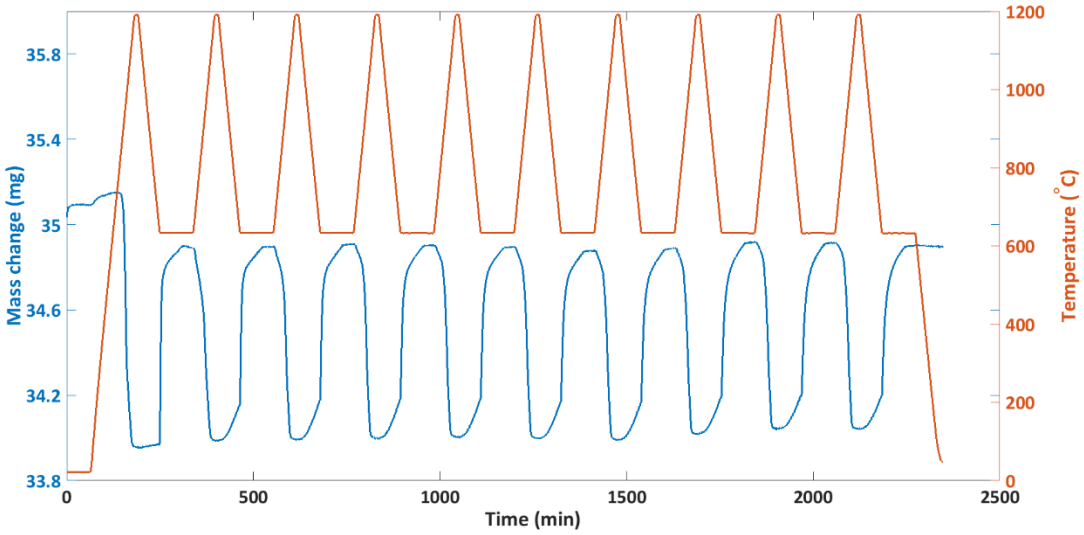

Figure 3.3 Cycling performance of the 0.5-1 mm particles subjected to 10 consecutive thermal cycles

3.5 Physical and chemical characterization

Physical and chemical characteristics of the metal oxide particles are investigated at reduced and oxidized forms. To obtain the reduced form of the mixed metal oxide, particles were reduced in a tube furnace at 1200 °C for 8 hours under nitrogen atmosphere (BOC, 99.5%). Then, the reduced particles were oxidized in a box furnace under atmospheric conditions for 8 hours at 750 °C to obtain the fully oxidized form of the particles. Both the reduced and oxidized particles were ground into powder using mortar and pestle before XRD analysis.

3.5.1 XRD and ICP-AES results

Powder X-ray diffraction (XRD) analysis was done employing a Bruker system (XRD, D2 Phaser diffractometer) using CuKα radiation $\lambda = 1.54178\,\text{Å}$ at a scanning rate of 0.2 °s^{-1}. The elemental analysis was carried out using a Varian Vista Pro Axial ICP-AES (Inductively-Coupled Plasma Atomic Emission Spectrometer) to investigate the ratio of Fe and Mn in the granules.

The crystalline phase composition of the material at reduced and oxidized forms is presented in Figure 3. The XRD patterns show a bixbyite phase (cubic Mn_2O_3; PDF#41-1442) for the oxidized sample, and a spinel jacobsite phase (cubic $MnFe_2O_4$; PDF#74-2403) for the reduced sample. It should be mentioned that the differentiation between the bixbyite Mn_2O_3 and bixbyite $(Fe,Mn)_2O_3$ structures is not possible based only on XRD because of the very close atomic size of Mn and Fe. Therefore, to confirm the presence of Fe in the oxidized form of the sample, Inductively Coupled Plasma Atomic Emission Spectroscopy (ICP-AES) was applied. The ICP-AES analysis revealed the presence of Mn and Fe elements at atomic ratio of Fe:Mn 1.99:1, verifying the target molar ratio of 2:1. Based on the Fe-Mn-O phase diagram, the oxidized form of the material should also have a corundum phase. This phase is not seen in the XRD results. It is likely that rapid cooling of the sample after the oxidation reaction led to a non-equilibrium state at the low temperature.

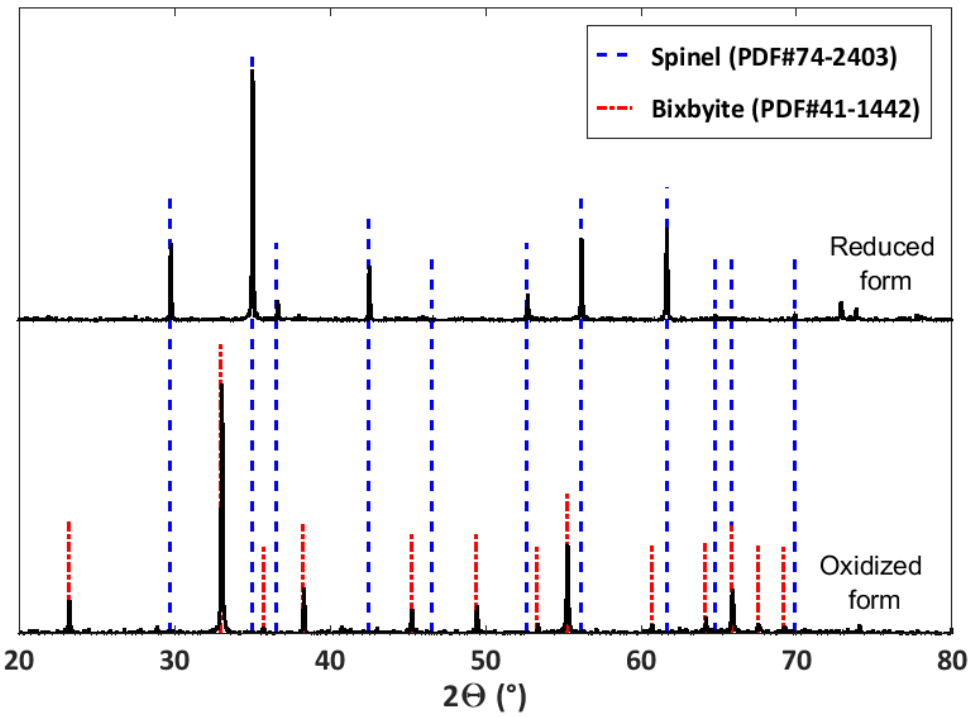

Figure 3.4 X-ray diffraction patterns of the iron–manganese oxide in the oxidized and reduced forms

3.5.2 BET results

The specific surface area was determined by nitrogen absorption-desorption analysis at -196 °C by applying the multi-point Brunauer–Emmett–Teller (BET) method and using a surface and porosity analyzer (TriStar II 3020, Micromeritics). Samples were degassed at 350 °C under vacuum for 4 hours before the measurement. The total pore volume was estimated using the t-plot method.

The BET analysis revealed a specific surface area and pore volume of 0.3880 $m^2 g^{-1}$ and ~0.001 $cm^3 g^{-1}$ for the synthesized iron–manganese particles, respectively. The BET results indicate that the synthesized particles have a very low porosity (less than 0.1%).

3.5.3 SEM results

Scanning electron microscopy (SEM) was conducted using an FEI Quanta microscope with secondary electron imaging operating at 5 kV accelerating voltage to obtain information on particle size and morphology.

Figure 3.5 a and b show the SEM images of two different iron–manganese oxide particles at their oxidized and reduced forms, respectively. The first images show the size and shape of the particles and prove that the particles are in the size range of 0.5 to 1 mm. The second images indicate that the surface of the particles has very few and small holes. BET analysis also confirmed the low porosity of particles. The size of the grains of the particles can be seen in the last two images. These images show that the grain size remains the same after the reaction, suggesting that the morphology of the particles does not change significantly after the first redox cycle.

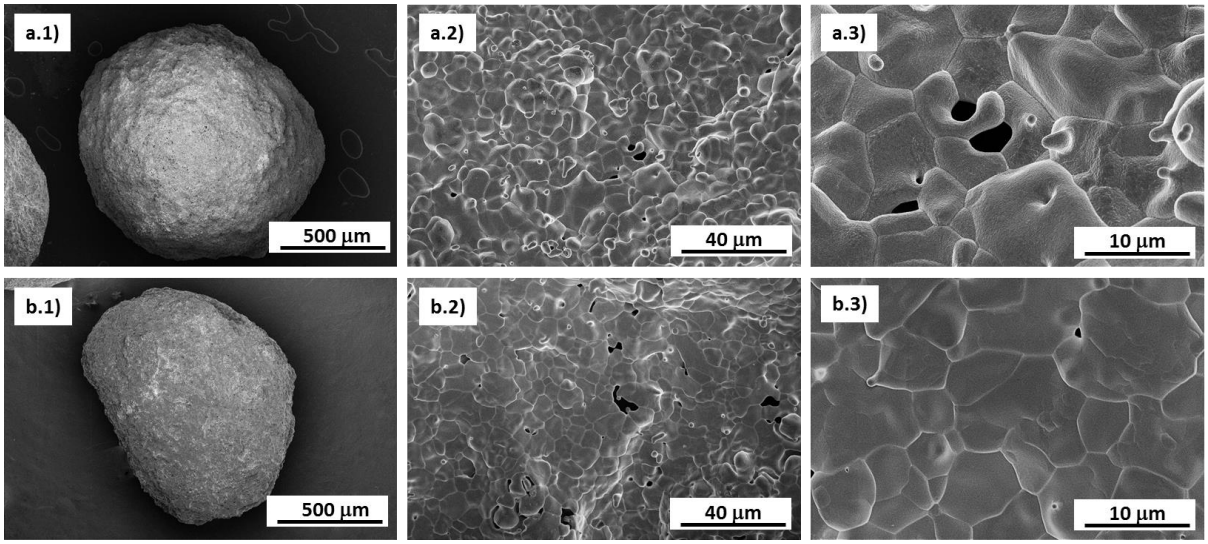

Figure 3.5 SEM micrographs of a) oxidized and b) reduced form of iron-manganese oxide particles (two different particles)

3.6 Summary

Large spherical iron–manganese oxide with the particle size of 0.5-1 mm was investigated for solar thermochemical energy storage in this chapter. The particles were prepared from inexpensive and non-toxic iron oxide and manganese oxide using the intensive mixing technique. The metal oxide mixture was thermodynamically studied first. Then, the stability and cyclability of the particles were tested under 10 cycles using a TGA instrument. Finally, the physical and chemical characteristics of the particles at oxidized and reduced forms were investigated using XRD, ICP-AES, BET and SEM.

4 Reduction reaction kinetics and enthalpy [1]

4.1 Introduction

Spherical 0.5 to 1 mm iron–manganese oxide with the Fe/Mn molar ratio of 2:1 is investigated in this work as a potential TCES material. The material synthesis was described in chapter 3. The cyclability test also in that chapter showed that this material is capable of being used as redox storage material.

For the iron–manganese oxide binary system, the thermodynamic analysis in section 3.3 indicated the presence of $(Mn,Fe)_2O_3$ at low temperatures and $(Mn,Fe)_3O_4$ at high temperatures. Therefore, the redox reaction of the synthesized mixture that has Fe to Mn ratio of 2:1 stores and releases energy based on the following reaction

$$6(Mn_{0.33}Fe_{0.67})_2O_3(s)+\Delta H_r \leftrightarrow 4(Mn_{0.33}Fe_{0.67})_3O_4(s)+O_2(g), \quad (4.1)$$

where $(Mn_{0.33}Fe_{0.67})_2O_3$ is the fully oxidized material and $(Mn_{0.33}Fe_{0.67})_3O_4$ is the fully reduced material which is the cubic spinel of $MnFe_2O_4$.

In this chapter, the reaction kinetics and enthalpy of the forward reaction of the redox process of (4.1) is studied. The thermal reduction is carried out under both argon and air atmospheres. The analysis is performed by non-linear regression applied to non-isothermal data recorded using thermogravimetric analysis (TGA) at four heating rates along with differential scanning calorimetry (DSC). A shrinking core model is used to fit the kinetic data for the large spherical

[1] Material in this chapter along with chapter 3 has been published in: M. Hamidi, A. Bayon, V.M. Wheeler, P. Kreider, M.A. Wallace, T. Tsuzuki, K. Catchpole, A.W. Weimer, "Reduction kinetics for large spherical 2:1 iron–manganese oxide redox materials for thermochemical energy storage" Chemical Engineering Science, 201 (2019) 74-81

particles. The model itself is of theoretical interest as it allows for better understanding of the role of oxygen diffusion in iron–manganese oxide particles during the thermal reduction. The resulting reaction rate expression and reaction enthalpy obtained in this chapter will be used in reactor modelling in chapter 6.

4.2 Experimental procedure

The thermal reduction of $(Mn_{0.33}Fe_{0.67})_2O_3$ was studied by thermogravimetric analysis (TGA) using a SETSYS Evolution 1750® (Setaram) machine. In each experiment, ~30 mg of $(Mn_{0.33}Fe_{0.67})_2O_3$ with the particle size of 0.5-1 mm was placed in a 90 μL alumina crucible in the TGA system.

Initially, the samples were heated to 150 °C and held for 30 min to remove any possible moisture from the particles. Then, the active mixed oxide was heated up to 1350 °C at different heating rates of 2.5, 5, 10, and 20 °C min^{-1} followed by an isothermal period of 10 min. The experiments were carried out under ultra-high purity Argon (BOC, 99.999%) and synthetic air (BOC, industrial grade) with a 100 ml min^{-1} gas flowrate. Blanks were run for each gas flow and heating rate and used as a baseline to mitigate the effects of buoyancy and momentum due to changing temperatures.

Furthermore, differential scanning calorimetry (DSC) was carried out under similar conditions using the same amount of the material as for TGA analysis. The DSC signal was evaluated by the CALISTO® processing software. The reaction enthalpy was determined for the reduction reactions under both argon and air atmospheres.

4.3 Results and discussion

4.3.1 Experimental results

The non-isothermal experimental mass change curves at four different heating rates obtained from TGA measurements are shown in Figure 4.1 for both argon and air atmospheres. According to the stoichiometry of reaction (4.1), theoretical mass loss for complete conversion of $(Mn_{0.33}Fe_{0.67})_2O_3$ to $(Mn_{0.33}Fe_{0.67})_3O_4$ is 3.35%. Based on the experimental data, all samples under the four heating rates and two atmospheres (argon and air) reached complete conversion.

The reduction reaction starts at ~800 °C in argon and ~1000 °C in air, in agreement with the thermodynamic phase diagrams found in Figure 3.2. The reaction temperature is higher in air due to the higher partial pressure of oxygen in the atmosphere, and the reaction proceeds faster in the air atmosphere than in argon because of the higher reaction temperature. This effect of partial pressure of oxygen on the reaction temperature and reaction rate has been seen before in prior work.[74] The onset temperature of reaction clearly increases with the heating rate for the argon case as well as the air case but is less prominent in the latter. The thermal reduction of the active redox particles seems to occur in a single step in an argon atmosphere while a two-step mechanism is apparent in an air atmosphere. The two-step reduction reaction has not been seen for other mixtures of iron–manganese.[73, 74] These mechanisms will be further explored in a later section.

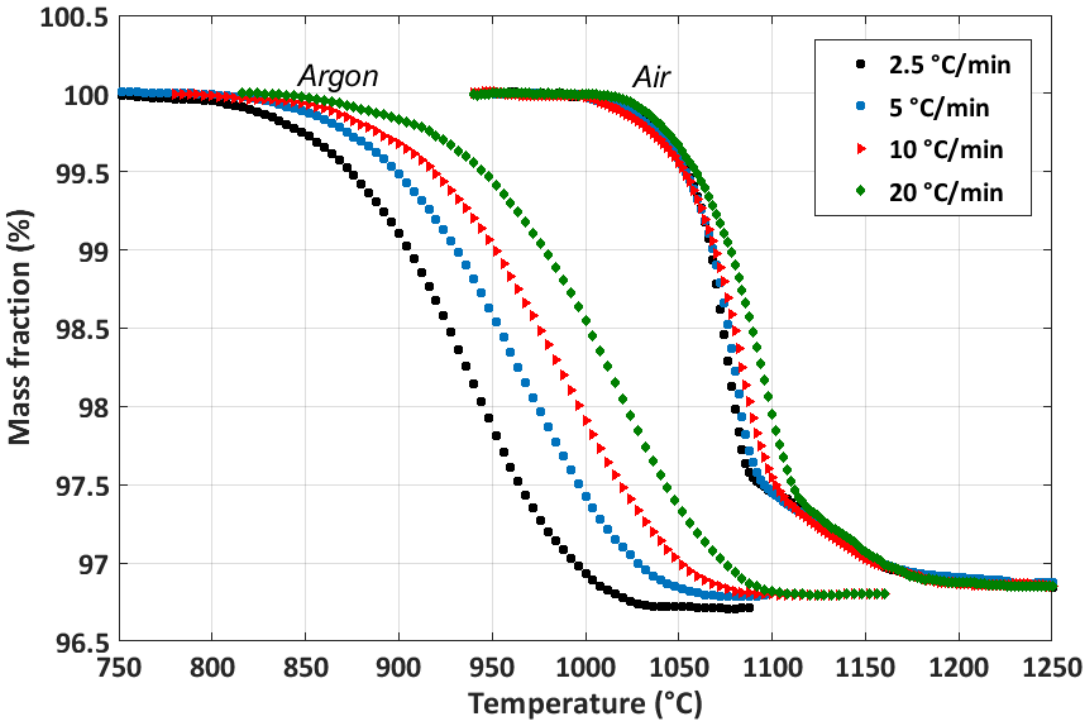

Figure 4.1 Experimental TGA curves of the thermal reduction of $(Mn_{0.33}Fe_{0.67})_2O_3$ at different heating rates in argon and air

The heat storage during the reduction reaction in argon and air was measured using DSC. Results are shown in Figure 4.2. As expected, the heat flow curves show endothermic peaks during the heating for both reactions.

For the reduction reaction in argon, the onset of endothermic reaction in the DSC curve is at 840 °C which corresponds to the start of reaction, i.e. mass loss. This temperature is slightly higher than the reaction temperature from the thermodynamic equilibrium analysis. The reason for this difference is the high heating rate used in this experiment (10 °C min^{-1}). High heating rates lead to delay in the reaction, as the 0.5 to 1 mm particles need more time to reach the setpoint temperature. The offset of endothermic reaction in the DSC curve is where the mass change stops.

Two separate endothermic peaks can be seen for the reduction in air. The onset of the second endothermic reduction reaction in the DSC signal is recorded at ~1120 °C, and that is where the trend of the TG signal starts to vary. The reaction at temperatures higher than 1120 °C is slow compared to the initial lower temperature reduction, and the enthalpy associated with this region of reduction is also relatively small. Therefore, it is recommended to operate below 1120 °C for the reduction reaction in air for thermochemical energy storage.

By integrating the DSC peaks over time, it is possible to calculate the stored particle energy. The area below the endothermic peaks is determined by tangential-sigmoidal integration. The calculated reduction enthalpy for the particles is 200.0 ± 8.3 J g^{-1} and 199.6 ± 14.2 J g^{-1} for the reactions under argon and air atmospheres, respectively. Note that DSC measurements were carried out in open crucibles which may lead to some heat losses due to the open system. The calculated reduction enthalpy is slightly higher than the reported enthalpy of pure manganese oxide (184 J g^{-1})[42] and lower than the reduction reaction enthalpy of pure iron oxide (560 J g^{-1}) [58]. The determined enthalpy values are also in agreement with the reported enthalpy values for iron–manganese oxide mixtures in recent papers. For instance, Andre et al. showed an average enthalpy of 187.7 J g^{-1} for mixtures with 20-50% iron in manganese oxide.[75]

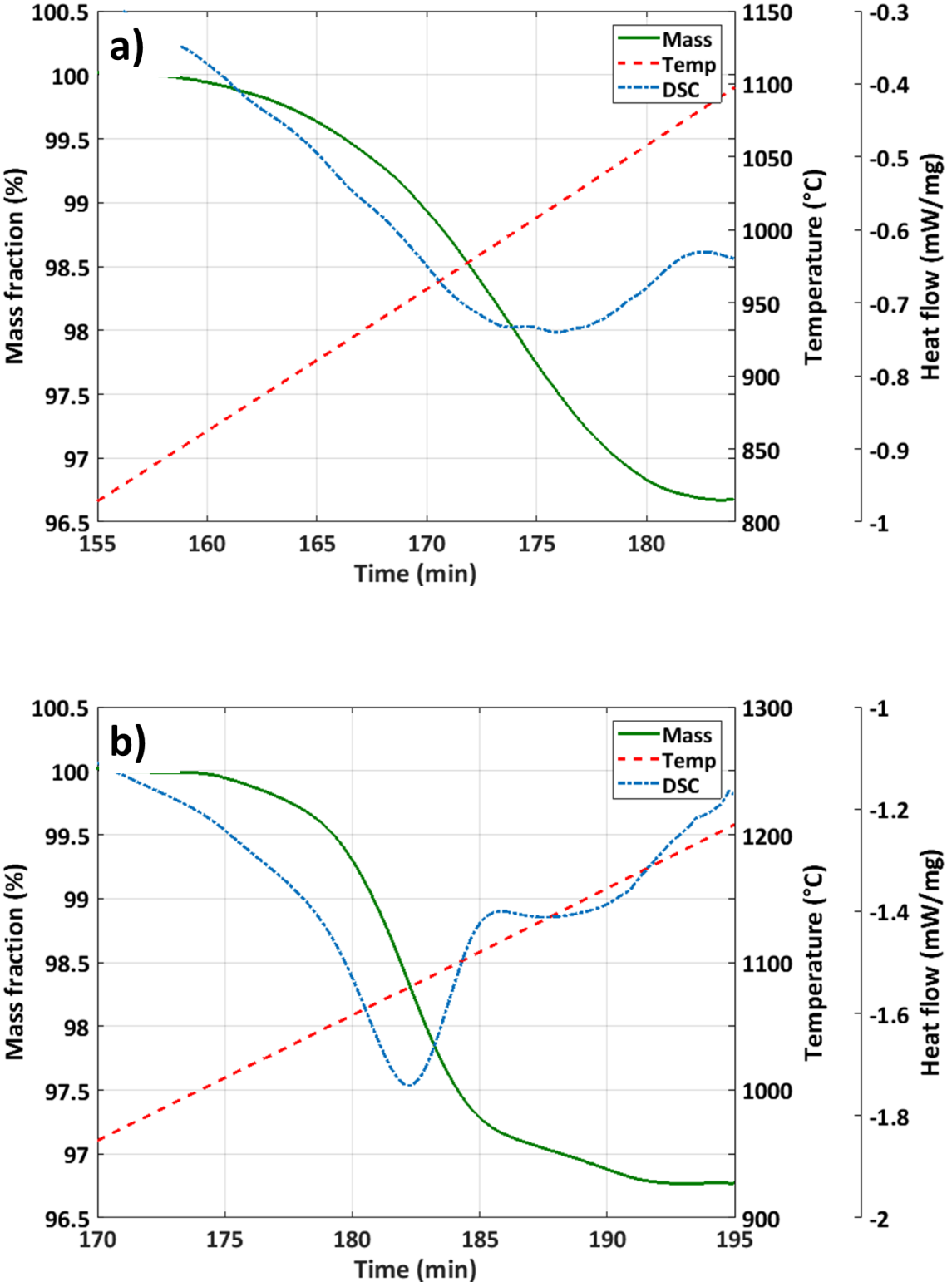

Figure 4.2 DSC and TGA curves for iron–manganese oxide reduction reaction under heating rate of 10 °C min^{-1} in a) argon and b) air

4.3.2 Kinetic modelling results

The general form of the solid–gas reaction rate (equation (2.7)) is considered here for thermal reduction of iron–manganese oxide particles. This reaction rate is assumed to be the product of the temperature-dependent kinetic constant $k(T)$, the pressure dependence $h(P)$, and the reaction model $f(\alpha)$, [67] We consider the Arrhenius model (equation (2.10)) for the kinetic constant here. Although the pressure term is usually neglected in the kinetic study, it can have a strong effect on the kinetic process. This term can adopt different mathematical expressions. For reversible solid–gas reactions, it is usually presented by partial pressure of the reaction gas and the corresponding pressure of the gas at thermodynamic equilibrium.[67] The pressure dependence term considered in this work is

$$h(P) = (1 - \frac{P_{o_2}}{P_{o_2,eq}})^m . \tag{4.2}$$

m is the order of pressure dependence which adjusts a suitable pressure term with the experimental data. The correlation between oxygen partial pressure (P_{O_2}) and oxygen partial pressure at equilibrium ($P_{O_2,eq}$) has been calculated using the FactSage thermochemical software

$$\ln(\frac{P_{O_2,eq}}{Pt}) = -34.54 \times \frac{1000}{T} + 26.27 , \tag{4.3}$$

where Pt is the total pressure and T is temperature in Kelvin.

Replacing the kinetic constant and pressure dependence terms into the general form of the solid–gas reaction rate (equation (2.7)) gives

$$\frac{\mathrm{d}\alpha}{\mathrm{d}t} = A\exp\left(-\frac{E}{RT}\right) f(\alpha)(1 - \frac{P_{o_2}}{P_{o_2,eq}})^m . \tag{4.4}$$

To describe the reaction progress, the reaction mechanism, the Arrhenius parameters and the order of pressure dependence need to be determined. The experimentally calculated Arrhenius parameters calculated here are not necessarily the intrinsic reaction parameters. Therefore, we term the parameters calculated in this section "effective" or "apparent" parameters.

Solid state reactions in particle systems can follow a volumetric or a shrinking core model. A volumetric model is used when the intrinsic reaction rate is relatively slow compared to the internal mass diffusion. For solid reactants that are nonporous or have a low porosity, the diffusion rate can be slower than the intrinsic reaction rate. In that case, the shrinking core model is often used.[79] When the overall size of the particles remains constant during the reaction and just the size of the unreacted core decreases, the shrinking core model is also called unreacted shrinking core model. [39, 40]

The synthesized iron–manganese particles have low pore volume and a very low porosity (less than 0.1%) (Section 3.5.2, BET results). Therefore, the shrinking core model is used to describe the reaction of these spherical 0.5 to 1 mm particles. Considering the shrinking core model[80], thermal reduction of iron–manganese oxide particles occurs via three steps (processes) as there is no gaseous reactant involved in the reaction.[79] First, the chemical reaction occurs on the surface of the unreacted core in the particle. During this step, $(Mn_{0.33}Fe_{0.67})_2O_3$ converts to $(Mn_{0.33}Fe_{0.67})_3O_4$ and oxygen is produced. Then, the produced oxygen diffuses through the reacted zone of particle and reaches the surface. After that, the oxygen molecules on the particle surface diffuse through the gaseous layer surrounding the particle. Depending on the characteristics of particles and the reaction conditions, one of these steps is the slowest and controls the rate of reaction process.

To investigate which one of these three mechanisms (chemical reaction, internal diffusion, and external diffusion) is the controlling step for the reaction, each mechanism was fitted to the

experimental data separately. By using this technique not only are we able to verify the best fit, but also it enables us to obtain unique Arrhenius parameters corresponding to each mechanism. The reaction model for each step of the shrinking core model for thermal reduction of iron–manganese oxide particles is described in Table 4.1.

Table 4.1 Reaction model for each step of the shrinking core model

Process step	Chemical reaction	Internal diffusion	External diffusion
Reaction model	$f(\alpha)=3(1-\alpha)^{2/3}$	$f(\alpha)=\frac{3(1-\alpha)^{2/3}}{2\left[1-(1-\alpha)^{1/3}\right]}$	$f(\alpha)=1$

Non-linear regression has been employed here as the fitting tool to determine the model parameters (equation (2.20)). Linear regression has also been to find initial values for the non-linear regression (equation (2.19)).

The fitting is done for conversions between $0.05 < \alpha < 0.95$ for argon and air atmospheres. The fitting results show that 3D internal diffusion (Jander diffusion)[69] predicts the reaction in an argon atmosphere better than chemical reaction and external diffusion mechanisms. For the reaction in air, the internal diffusion fits best up to 70-80% conversion (depending on the heating rate). The effective reaction rate for the reduction of $(Mn_{0.33}Fe_{0.67})_2O_3$ along with the calculated *E*, *A* and *m* parameters is

$$\frac{d\alpha}{dT}=\frac{8.85\times10^{15}\frac{1}{\min}}{\beta}\exp\left(-\frac{426.13\frac{kJ}{mol}}{RT}\right)\frac{3(1-\alpha)^{2/3}}{2\left[1-(1-\alpha)^{1/3}\right]}\left(1-\frac{P_{O_2}}{P_{O_2,eq}}\right)^{25.01} \qquad (4.5)$$

Equation (4.5) is valid for the reaction in argon between conversions $0.05 < \alpha < 0.95$ and reaction in air in the conversion range of $0.05 < \alpha < 0.8$. Partial pressure of oxygen is

considered to be zero and 21 kPa for argon and air atmospheres, respectively. The effect of partial pressure of the produced oxygen is neglected in this work.

For the reduction reaction in air at higher conversions ($0.8 < \alpha < 0.95$), our modelling results showed that external diffusion is the rate limiting mechanism.

The predicted conversion values versus the experimental data for thermal reduction of iron–manganese oxide under argon atmosphere are shown in Figure 4.3. The small deviation of the predicted values from the experimental data can be explained by the fact that chemical reaction and external diffusion are also occurring during the process.

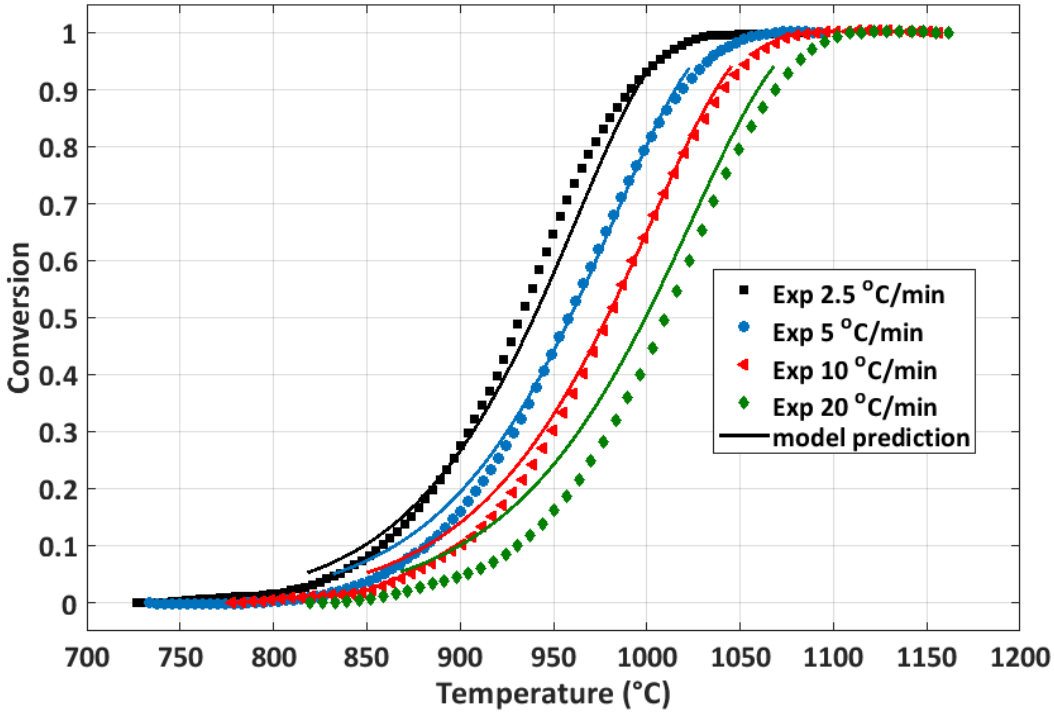

Figure 4.3 Modelling result for the reduction reaction in argon

The model prediction for the reduction reaction in air is shown in Figure 4.4. Similar to the reaction in argon, the small deviation from the experimental data in the first part of the reaction

might be due to the chemical reaction and external diffusion occurring simultaneously with the internal diffusion. For the second part of the reaction where the external diffusion fits the best amongst the other steps, the process is not affected by the heating rate. For that reason, the model is independent of the heating rate and shows one single curve for different heating rates. Further explanation of the physics of the external diffusion will be discussed later.

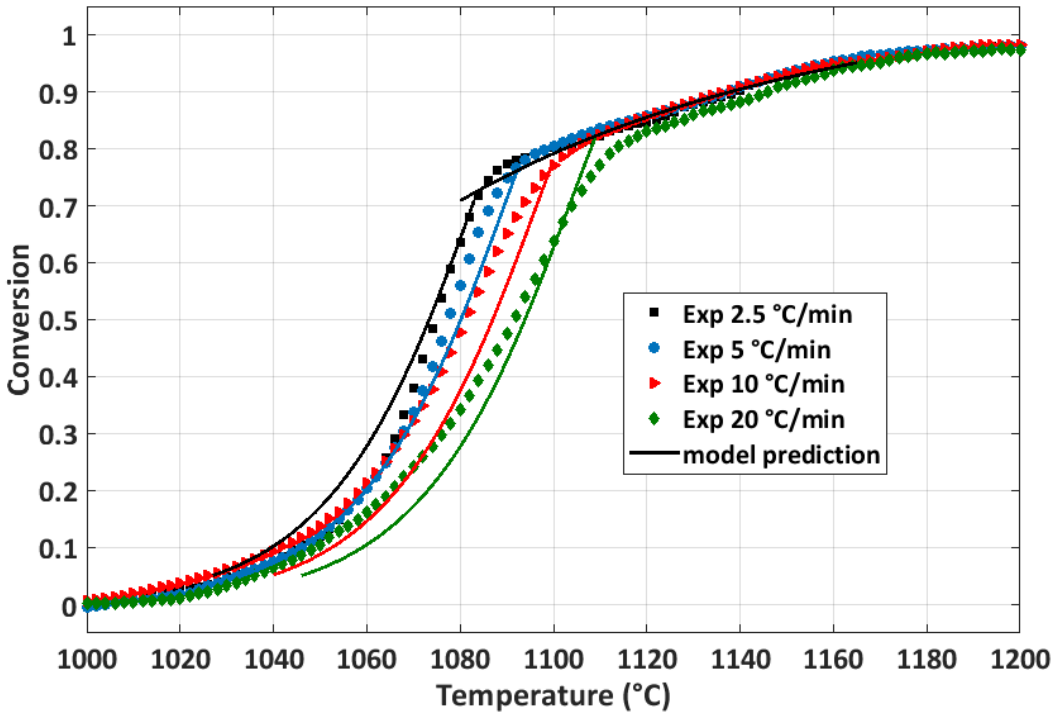

Figure 4.4 Modelling result for the reduction reaction in air

Based on the shrinking core model considered for the thermal reduction of spherical 0.5 to 1 mm diameter iron–manganese oxide particles and the results from the model fitting, we propose the following for reaction mechanism: for the reduction reaction in an argon atmosphere, the internal diffusion of oxygen through the reacted zone of the particle is the controlling step for the entire reaction (Jander diffusion). In air, however, the oxygen internal diffusion controls the process up to 70-80% conversion. Subsequently, external diffusion

becomes the controlling step of the reaction and the reaction rate becomes slower. High partial pressure of oxygen in the gaseous layer around the particles is most likely the reason of this change in reaction behaviour. From the modelling results we can suggest that at the start of the reaction, the difference between the concentration of oxygen on the surface of the particles and in the gaseous layer is high, which means the driving force for external diffusion is high. Therefore, the external diffusion is fast compared to other steps. As the reaction proceeds, more and more oxygen is produced. This oxygen diffuses through the reacted zone of the particle, reaches the surface and diffuses through the gaseous layer. The concentration of oxygen in the gaseous layer becomes high at higher conversions while the concentration of oxygen on the particle surface remains constant, thereby reducing the transport of oxygen out of the particle and limiting the reaction.

Comparing the results of our kinetic modelling with the reaction kinetics reported in literature for other mixtures of iron–manganese oxide is not an easy task. The reason is that the material properties such as morphology, particle size and surface area affect the reaction behaviour of these materials.[39, 75] Different synthesis methods also affect the reaction kinetics since they lead to variation in the obtained physical properties of the material. For instance, Wokon et al.[74] investigated the redox reaction of manganese–iron oxide particles with Fe/Mn molar ratio of 1:3, prepared using a build-up granulation technique. They chose an empirical kinetic model of Avrami–Erofeev for the reduction reaction of their particles. In another work, Botas et al.[81] investigated the kinetics of the reduction reaction of commercial pure manganese oxide. They stated that the reduction reaction can be first order or follow a contraction mechanism. The reaction models suggested in other studies for thermal reduction of iron–manganese oxide mixtures have also been tested here with our experimental TG data. Previous reaction models were less accurate than the current shrinking core model presented here.

Previous studies have found that the activation energy for the reduction reaction of iron–manganese oxide systems increases with iron content (254.14 kJ mol^{-1} for a mixture with 0% iron[81] and 355.72 kJ mol^{-1} for a mixture with 25% iron [74]). The activation energy calculated here is 426.13 kJ mol^{-1} for the mixture with 67% iron, which agrees with this trend.

4.4 Summary

The results from thermal analysis using TGA and DSC showed that the reduction reaction of this material is complete under both inert and air atmospheres with the reaction enthalpy of ~200 J g^{-1}, which is higher than the reaction enthalpy of pure manganese oxide. A three-step shrinking core model was used to study effective kinetics of this reduction reaction. Our modelling results show that the oxygen internal diffusion is the controlling step of the reaction in an argon atmosphere. In air, internal diffusion controls the reaction only up to 80% conversion. After that, the reaction rate is most likely controlled by the external diffusion of oxygen in the gas film surrounding the particle.

5 Heat transfer study in the packed-bed reactor [1]

5.1 Introduction

The physical and chemical characteristics and the reduction reaction kinetics of the synthesized iron–manganese oxide mixture as a TCES material candidate were studied in chapter 3 and chapter 4, respectively. To have a realistic understand of how this material would perform in a solar driven reactor, a lab-scale packed-bed reactor is designed and fabricated as part of this doctoral thesis. The designed reactor is directly exposed to an external source of high-flux infrared radiation (IR) which simulates the solar radiation.

In this chapter, the fabricated packed-bed reactor is described first. Then, the heat transfer in the packed bed is studied in the temperature range of 800 to 1100°C when no chemical reaction is occurring during the heating. A two-dimensional transient heat transfer model considering conduction, convection and radiation heat transfer is developed to simulate the temperature profile in the reactor. The effective heat transfer parameters—effective thermal conductivity and wall heat transfer coefficient—are the outcomes of this heat transfer study. They are determined as functions of temperature—at fixed particle size, porosity and Reynolds number—by solving an inverse problem using the model at steady-state and comparing with the experimental data. The validity of calculated effective parameters is checked by employing the parameters in a transient model and comparing the predicted temperature profile with transient experimental data and by comparison with existing correlations found in the literature.

[1] Material in this Chapter has been published in: M. Hamidi, V.M. Wheeler, P. Kreider, K. Catchpole, A.W. Weimer, "Effective thermal conductivity of a bed packed with granular iron–manganese oxide for thermochemical energy storage" 2019, Chemical Engineering Science, 207 (2019) 490–494

The heat transfer parameters derived here are necessary for overall TCES system modeling and process scale-up.

The thermochemical performance of the packed-bed reactor will be discussed in chapter 6.

5.2 Experimental description

An electric IR furnace (P4C-VHT, Advance Riko) is used as the heating source in this setup. The furnace is composed of 4 IR lamps (2kw each) with a 40 mm opening diameter and heating length of 100 mm. A quartz tube is always used for protection of the IR lamps against thermal degradation. The packed-bed reactor will be placed in the centre of this furnace. A schematic diagram of the top view of the furnace is shown in Figure 5.1.

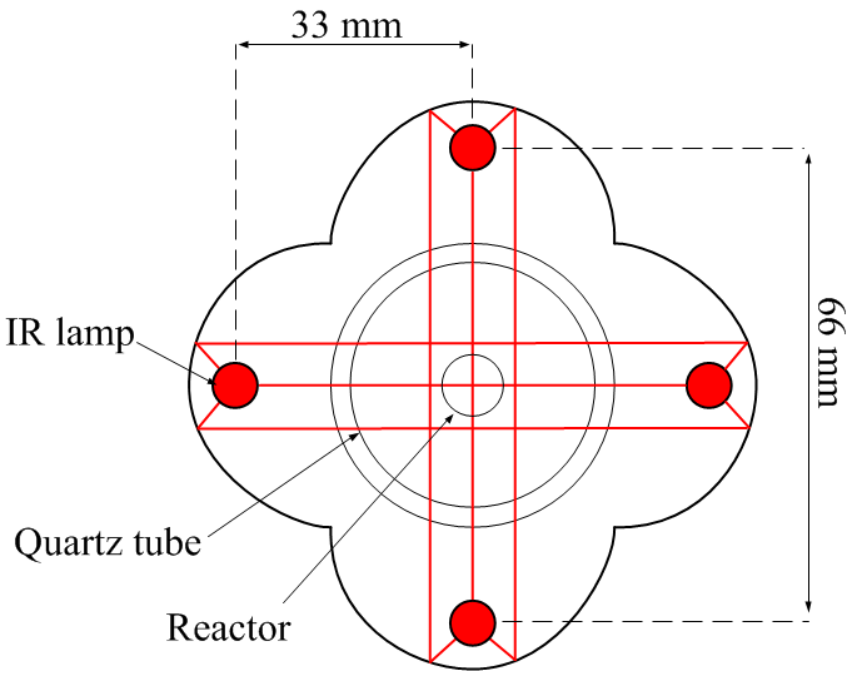

Figure 5.1 Schematic diagram of top view of IR furnace

The reactor is composed of a vertical tube packed with spherical active particles to a height of 3 cm. The tube is made of alumina (extruded alumina > 99.7%, Ceramic Oxide Fabricators) and has outer and inner diameters of 26 mm and 21 mm, respectively. The particles are placed

on top of an alumina disc which is supported by another tube with outer and inner diameters of 20 mm and 15 mm, respectively. The alumina disc has 3 holes of 2 mm diameter for the insertion of thermocouples. The disc also has 18 small holes of 0.86 mm diameter to let the gas pass through the bed. A thin layer of zirconia felt is placed on top of the disc to prevent particle loss. Figure 5.2 shows different parts of the reactor as well as the mounted reactor.

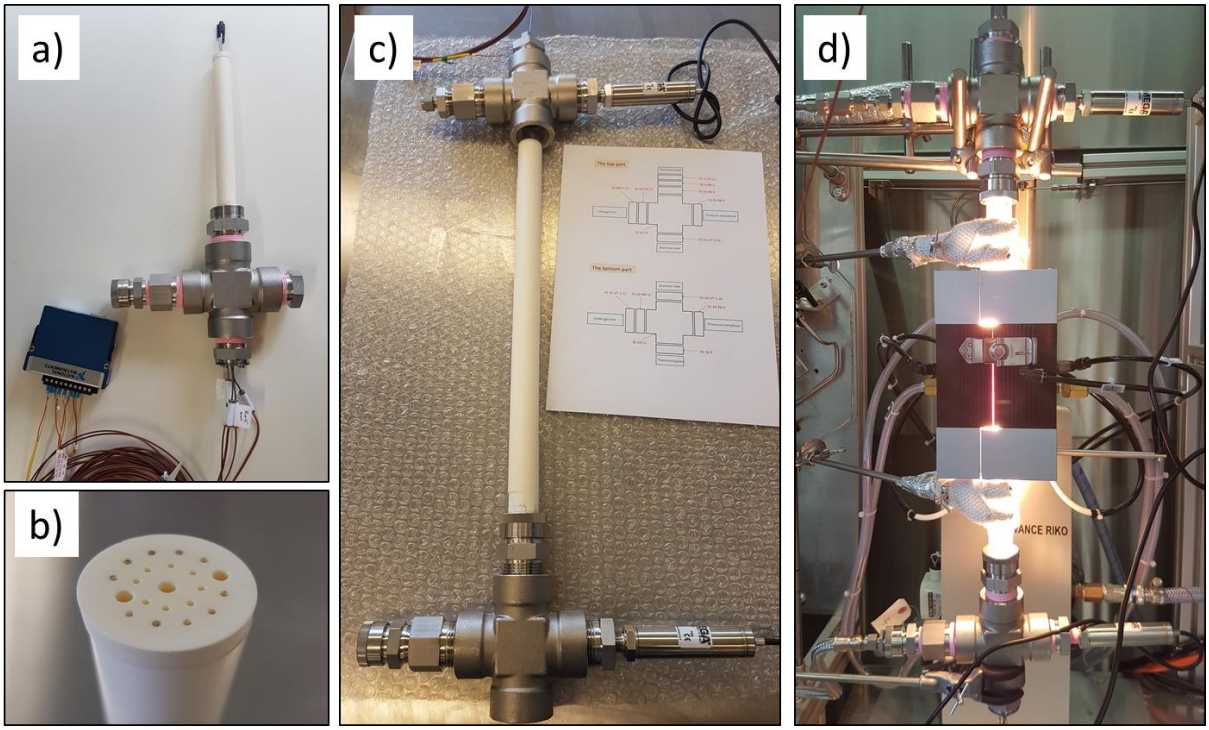

Figure 5.2 Experimental setup: a) inner tube b) alumina disc, c) outer tube, and d) mounted reactor in the IR furnace

Argon gas (COREGAS grade 5.0) with a flowrate of 100 ml/min flows through the bed from top to the bottom. The reactor is initially purged of air under pure argon at room temperature to prevent reactions from occurring during the heating of the bed. The gas flow is regulated by a mass flow controller (F-201CV, Bronkhorst) before being delivered to the tube. Three type K thermocouples (Inconel 600, 1.5 mm diameter, Temperature Controls) are installed in the packed bed. One of the thermocouples measures the tube wall temperature at the height of 1.5 cm from the disc. The wall temperature is used as the setpoint temperature for the furnace. The other two thermocouples are installed at the centre of the packed bed (r=0) and 5 mm from the

centre (r=5mm). The thermocouples are adjustable in the axial direction which allows temperature measurement at different heights of the packed bed (z=1, 2 and 3 cm from the disc). The temperature of the disc is also measured in an experimental run using one of the adjustable thermocouples. Temperature measurement locations are indicated by red dots in Figure 5.3.

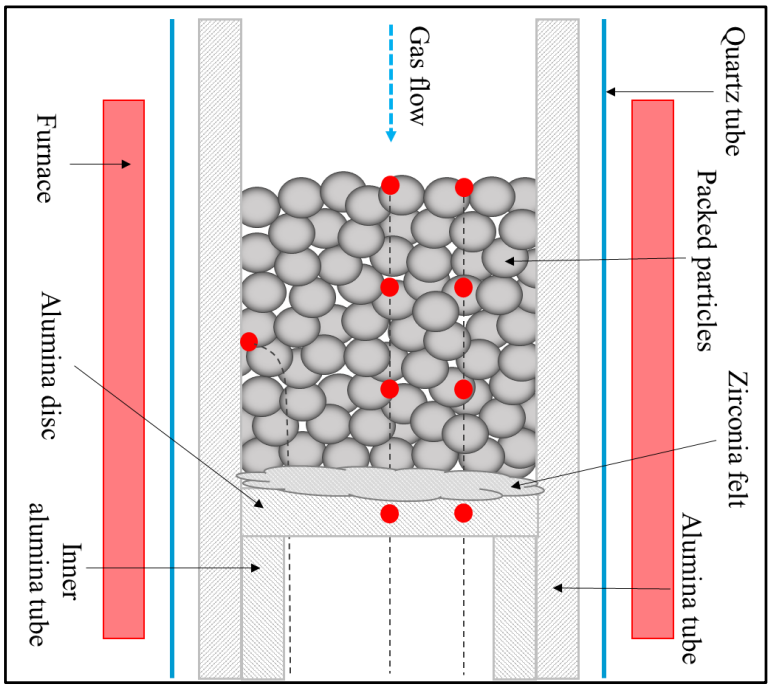

Figure 5.3 Schematic diagram showing a cross section of the experimental setup

The reduced form of iron–manganese oxide particles is used in this work to prevent any reduction reaction at high temperatures (800-1100 °C) under argon atmosphere. To obtain the reduced form, particles were reduced in a tube furnace at 1200 °C for 8 hours under a nitrogen atmosphere (BOC, 99.5%).

5.3 Heat transfer model

A general, dynamic, pseudo-homogenous, two-dimensional model for a vertical packed-bed reactor has been developed in this work (Appendix B). The local thermal equilibrium (LTE) condition has been assumed for this system after checking its validity using the criterion proposed by Kim and Jang.[82] Consult Appendix C for details on the LTE assumption. For the case where there is no chemical reaction in the bed and the effective thermal conductivity is the same in axial and radial directions, the governing equations reduce to a single statement of conservation of energy in terms of temperature, T:

$$-\rho_g c_{p,g} u_z^s \frac{\partial T}{\partial z} + \frac{\partial}{\partial z}(k_{eff} \frac{\partial T}{\partial z}) + \frac{1}{r}\frac{\partial}{\partial r}(k_{eff} r \frac{\partial T}{\partial r}) = (\varepsilon_b \rho_g c_{p,g} + (1-\varepsilon_b)\rho_s c_{p,s}) \frac{\partial T}{\partial t}, \qquad (5.1)$$

where ρ and c_p are mass density and specific heat capacity; *z* and *r* are the axial and radial coordinates, respectively; *t* is the time; ε_b is void fraction of the bed; and u_z^s is superficial gas velocity in *z* direction equal to the volumetric flow rate of the gas divided by the cross sectional area of the bed. Subscripts *s* and *g* represent solid and gas phase, respectively. The effective thermal conductivity of the bed is denoted as k_{eff} where "effective" identifies the apparent thermal conductivity accounting for transport phenomena in a homogenized, multi-phase media: conduction in the solid and gas phases, convection, and radiation.

Temperature is uniform at all radial and axial points and equal to the room temperature at the initial time,

$$T(r, z, 0) = T_0 \quad \text{at} \quad t = 0. \qquad (5.2)$$

The boundary condition on the top surface is mainly controlled by the radiative heat flux emitted by the surface and the radiative heat flux from the wall absorbed by the surface,

$$\rho_g c_{p,g} u_z^s T - k_{eff} \frac{\partial T}{\partial z} = A_2 F_{21} \sigma \varepsilon_{r,w} T_w^4 / A_1 - \varepsilon_{r,s} \sigma T^4 \quad \text{at} \quad z = L . \tag{5.3}$$

The emissivity of the wall and solid are given by $\varepsilon_{r,w}$ and $\varepsilon_{r,s}$, respectively; σ is the Stefan-Boltzmann constant; and T_w is the wall temperature. The first term on the right-hand side of Equation (5.3) represents the radiation from the tube wall above the bed that is absorbed by the top surface. F_{21} is the fraction of energy leaving the wall and reaching the surface of the bed. The second term on the right-hand side of the Equation (5.3) is the radiation emitted by the top surface.

At the bottom of the packed area, the temperature is assumed to be the same as the alumina disc temperature,

$$T = T_{disc} \quad \text{at} \ z = 0 . \tag{5.4}$$

At the packed-bed wall, the boundary condition is

$$-k_{eff} \frac{\partial T}{\partial r} = h_w (T - T_w) \quad \text{at} \quad r = R , \tag{5.5}$$

where h_w is the effective wall heat transfer coefficient and T_w is the wall temperature that is measured via a thermocouple.

A symmetry boundary condition is enforced at the centreline of the bed,

$$\frac{\partial T}{\partial r} = 0 \quad \text{at} \ r = 0 . \tag{5.6}$$

Equation (5.1) along with the initial and boundary conditions given by Equations (5.2)–(5.6) are solved if k_{eff} and h_w are known. However, these quantities are not simple constants.

5.4 Methodology for effective heat transfer parameter extraction

The effective thermal conductivity represents a number of transport phenomena parameters. Prior literature considered these parameters to be constants and found good agreement with experiment.[10, 83, 84] However, thermal transport in high temperature packed-bed reactors can not necessarily be modeled with constant thermal transport parameters over a wide range of temperatures due to the onset of nonlinearities in the effective thermal conductivity.[10] Therefore, effective parameters in this work are assumed to be functions of temperature. Radiation is a particularly strong contributor to the thermal transport at high temperatures. The unit cell technique is widely used to describe the effective thermal conductivity due to radiation.[85] For this method, radiation is treated as a local effect that takes place between boundary surfaces of a unit cell and neighbor particle surfaces and neglects long range radiative transport.[86] The optical density of the iron–manganese oxide particles makes this simplification acceptable for the present model. The general form of this parameter for a unit cell in a packed bed is given by

$$k_{eff}^{r} = 4F_{E}^{*}\sigma d_{p}T^{3}, \tag{5.7}$$

where k_{eff}^{r} is effective thermal conductivity due to radiation, F_{E}^{*} is the radiation exchange factor, and d_{p} is the diameter of the particles. Thus, we expect a third order temperature term in the effective thermal conductivity. The non-radiative part of the effective thermal conductivity of a packed bed is generally a function of the Reynolds number, thermal conductivity of the solid and fluid, and in some cases the Prandtl number.[10] Here we consider only a single Reynolds number for the flow so the effective thermal conductivity is expected to take the form:

$$k_{eff} = aT^{3} + bT^{2} + cT + d, \tag{5.8}$$

where T is the temperature in Kelvin and the first- and second-order terms account for any nonlinearities in the thermal conductivity of the gas and solid phase.

A first-order polynomial function is assumed for the wall heat transfer coefficient,

$$h_w = a'T_w + b', \tag{5.9}$$

where T_w is in Kelvin. This form of the effective wall coefficient has been considered before.[87]

Non-linear regression has been employed as the fitting tool to deduce the coefficients in the effective thermal conductivity and effective wall heat transfer coefficient: a, b, c, d, a' and b'. The residual sum of squares, *S*, defines the objective function to be minimized,

$$S(a,b,c,d;a',b') = \sum_{i=1}^{n}\left(T_i - \hat{T}_i(a,b,c,d;a',b')\right)^2 = \min, \tag{5.10}$$

to be minimized where n is the number of data points. Here T_i is an experimentally measured temperature, and $\hat{T}_i$ is the corresponding temperature predicted by a solution to the model described by Equations (5.1)–(5.6). A least-squares fitting routine results in a minimum *S* corresponding to the effective parameter coefficients that best predict the measured temperatures.

5.5 Results and discussion

The aim of this chapter is to determine temperature-dependent expressions for the effective thermal conductivity and wall heat transfer coefficient in a bed packed with iron–manganese oxide particles under high flux radiation when no chemical reaction is occurring during the heating. To make sure no chemical reaction occurs during the heating, XRD has been done before and after the thermal analysis of the system. Based on XRD patterns, Figure 5.4, the particles have remained in their reduced form (spinel, PDF#74-2403) after the thermal analysis.

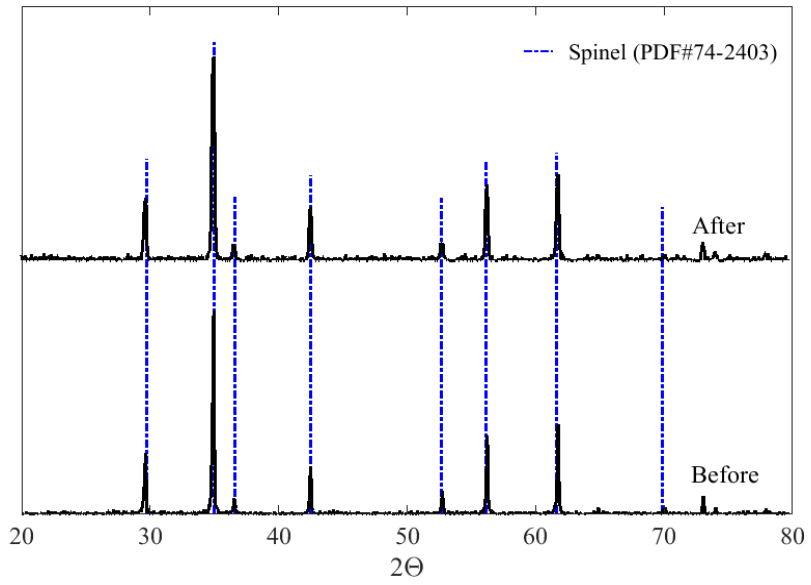

Figure 5.4 XRD patters of iron–manganese oxide before and after thermal analysis

Both the steady-state and transient heat transfer behaviour of the bed are investigated experimentally. For the transient analysis, the reactor is heated from the ambient room temperature to 1100 °C at a heating rate of 10 °C/min. For the steady state experiments, a dwell of 10 min is used at seven different wall temperatures: 800, 850, 900, 950, 1000, 1050, and 1100 °C. This dwell time is sufficient for the system to reach a steady-state condition. Figure 5.5 and Figure 5.6 present some parts of the steady-state measurements.

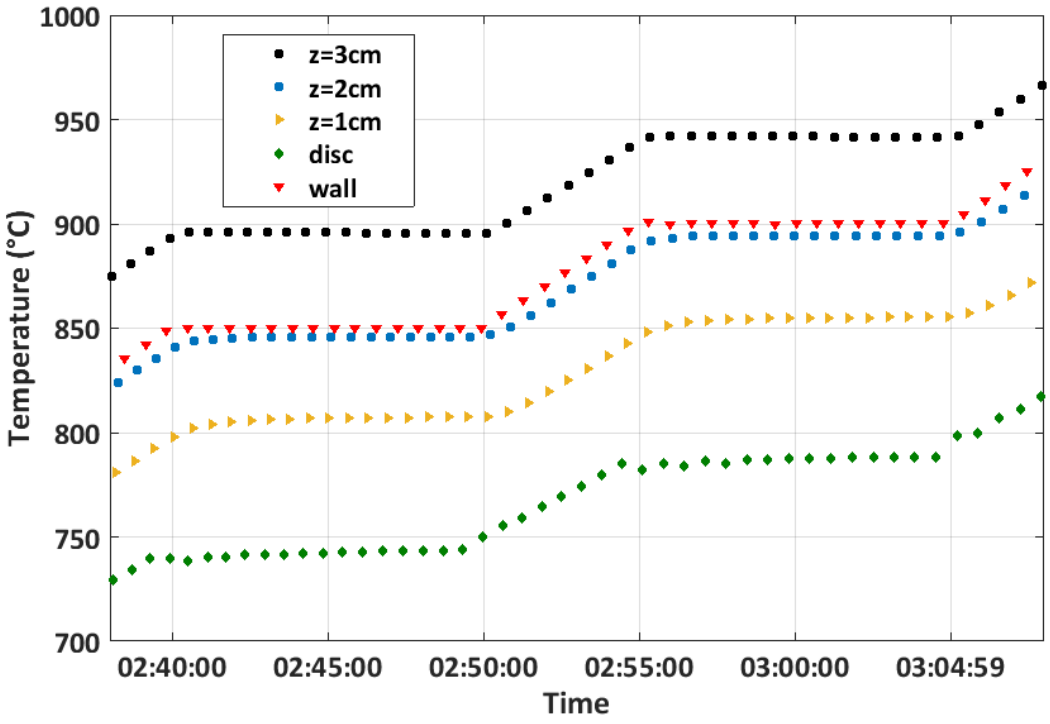

Figure 5.5 Measured temperatures at r=0 at wall temperatures of 850 and 900 °C for study state analysis

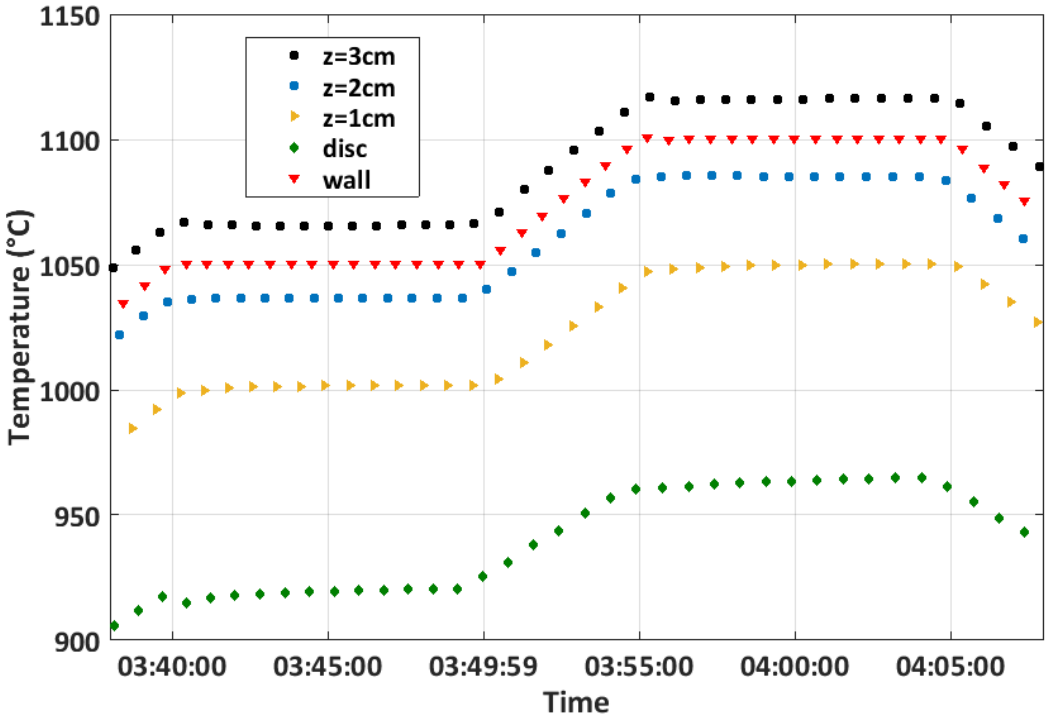

Figure 5.6 Measured temperatures at r=0.5 cm for at temperatures of 1050 and 1100 °C for steady state analysis

The data sets from the seven dwell temperatures were fit simultaneously for the coefficients defining the effective thermal conductivity and wall heat transfer coefficient, i.e. Equations (5.8) and (5.9), using the fitting routine described above. The specifications of the packed bed, particles, and the flowing gas are given in Table 5.1. The calculated coefficients for the temperature-dependent effective heat transfer parameters are shown in Table 5.2. In this table, the fitting error indicated in the parameters corresponds to the standard deviation.

Table 5.1 Packed bed, particle, and gas specifications

Parameter	**Value/correlation**	**Reference**
Particle diameter (mm)	$0.5-1$	
Particle BET surface area (m^2/g)	0.338	
Bed length (cm)	3	
Bed diameter (cm)	2.1	
Bed void fraction (-)	$0.383+0.254\frac{D}{d_p}^{-0.923}.\frac{1}{(0.723\frac{D}{d_p}-1)^{0.5}}$	Roshani [88]
Heat capacity of particle (J/mol.k)	$-1853512\times T^{-2}+144.76640$ $+8.593936\times10^{-2}\times T$	Bale et al.[51]
Heat capacity of argon (J/mol.k)	20.786	Bale et al. [51]
Density of argon gas (kg/m^3)	PM/RT	
Density of particle (kg/m^3)	5×1000	
Thermal conductivity of particle (W/m.K)	3.2	Takeda et al[89]
Thermal conductivity of argon (mW/m.K)	$5.465+0.04729*T-$ $0.1111*10^{-4}*T^2+0.1599*10^{-8}*T^3$	Saxena[90]
Superficial gas velocity (m/s)	$\dot{V}/A$	

Table 5.2 Effective heat transfer parameters and fitting errors

Effective heat transfer parameter	coefficient	value	error
k_{eff}, W/m^2.K	a	2.94×10^{-10}	0.14×10^{-10}
	b	-1.59×10^{-7}	0.06×10^{-7}
	c	3.87×10^{-4}	0.19×10^{-4}
	d	0.11	3.76×10^{-3}
h_w, W/ m.K	a'	0.109	0.29×10^{-2}
	b'	-1.13×10^{2}	0.03×10^{2}

The coefficients identified in Table 5.2 were used in the steady-state model. A solution of the model when the wall temperature is 1000 °C is shown in Figure 5.7a. The temperature gradient is much larger in the axial direction than the radial direction since the top boundary is exposed to radiation from the tube above the bed while the bottom boundary is shielded by zirconia felt and an alumina disc. The predicted axial temperature distribution at the bed centre (r=0) under steady-state conditions when wall temperature is 800, 950, and 1100 °C is shown in Figure 5.7b. The predicted temperature distribution agrees very well with the measurements.

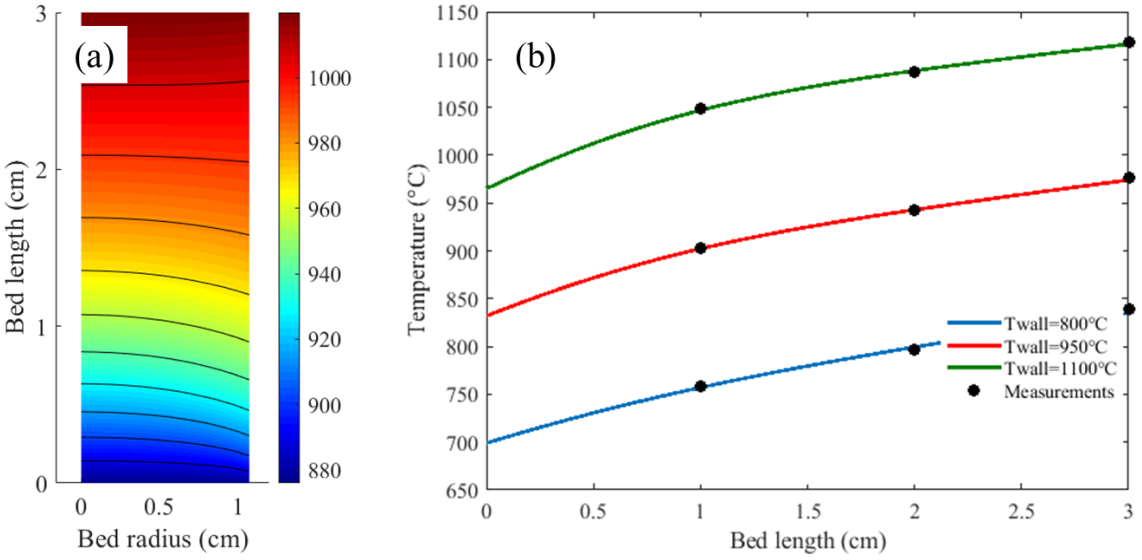

Figure 5.7 Steady state heat transfer modelling results. (a) Spatial distribution of temperature at T_w 1000 °C. (b) Comparison between the predicted axial temperature distributions with measurements for T_{wall} = 800, 950, and 1100 °C

Figure 5.8 shows the difference between the predicted temperatures and the measured temperatures in both axial and radial directions for 7 steady state conditions. The model is overpredicting the temperature at the location r = 0.5 cm and z = 2 cm the most with a maximum error of 4.7 °C, which is only 0.59%. On the other hand, the most underprediction of the model belongs to the location r = 0 cm and z = 3 cm with the maximum error of -3.6 °C. As can be seen, there is no pattern among these errors. We believe that the errors are mainly the experimental errors caused by reading the temperatures at not exact r and z locations.

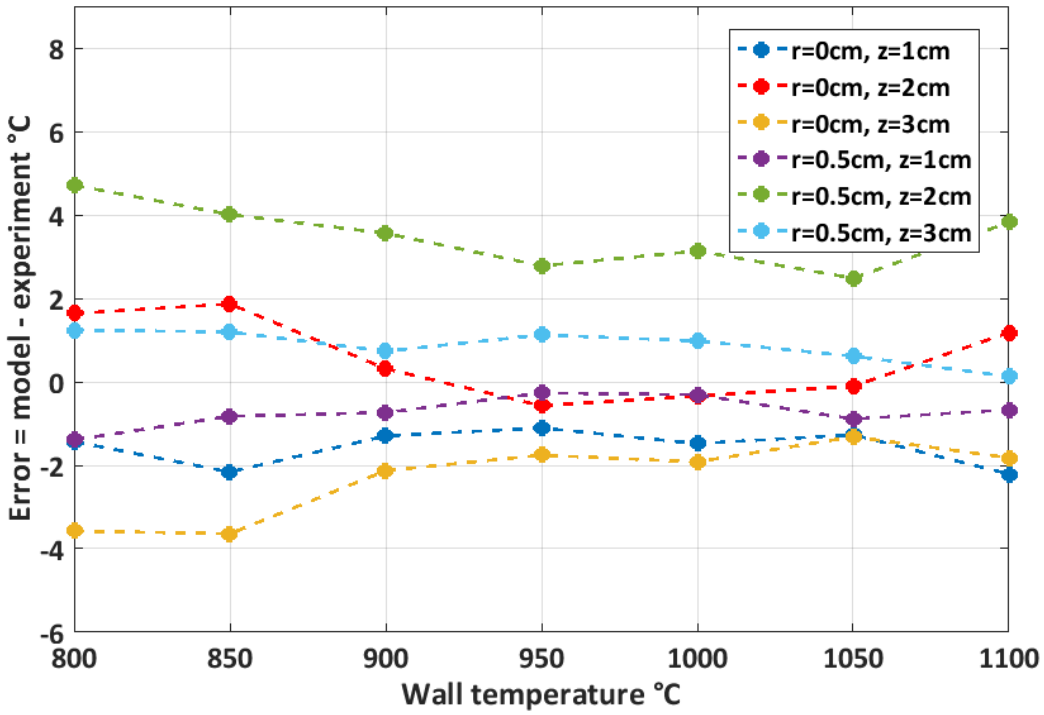

Figure 5.8 The difference between the predicted and the measured temperatures under steady state conditions

The effective heat transfer parameters in Table 5.2 are also used to predict the *transient* behaviour of the bed by solving Equation (5.1) with the transient term. An independent data set of transient temperature data at two locations in the centre of the bed (1 and 3 cm from the disc) is taken with the wall temperature increasing from 900 °C to 1100 °C and a heating rate of 10 °C/min. Very close agreement between the transient model and experimental data is

shown in Figure 5.9. This agreement gives strong evidence that the derived effective heat transfer parameters are valid for the simulation of the system under steady-state or transient conditions and with any heating procedure in the considered temperature range.

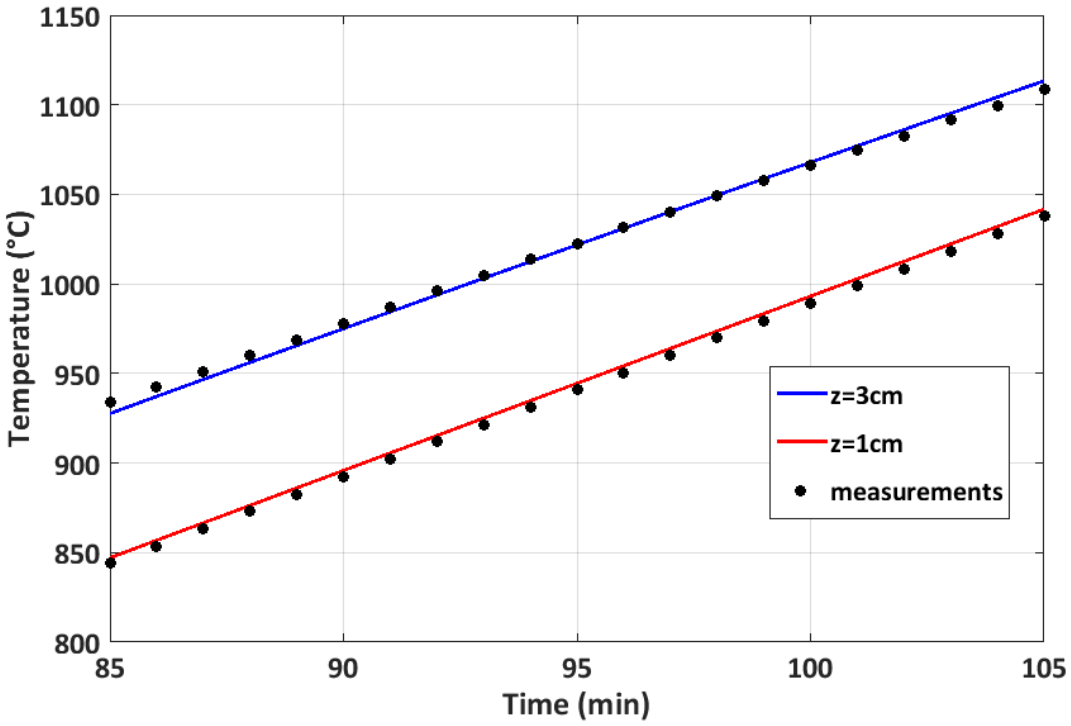

Figure 5.9 Comparison between the predicted axial temperature distributions using transient model with measurements at the bed centre

The calculated temperature-dependent effective thermal conductivity is compared with a number of correlations reported in the literature to ensure that it is within the range previously reported values. For any porous media arrangement, Deissler and Boegli[91] (D&B) proposed maximum and minimum bounds for the effective thermal conductivity. The derived effective thermal conductivity is inside of this range as shown in Figure 5.10. Two more effective thermal conductivity correlations are included in the figure for comparison with this work. The first is due to Breitbach and Barthels[92] (B&B) who used the unit cell approach, as described by Equation (5.7), with a derived expression for the radiation exchange parameter. The second comes from Kunii and Smith[93] (K&S) who used a lumped parameter model. See Appendix E

for additional details. The effective thermal conductivity determined here compares well with those calculated with more complex models by B&B and K&S. Both models are defined for stagnant fluid, so the contribution of fluid mixing and turbulence is not considered. These phenomena could be important in the present system and may explain the slightly higher values for effective thermal conductivity reported here compared to those from the other two models.

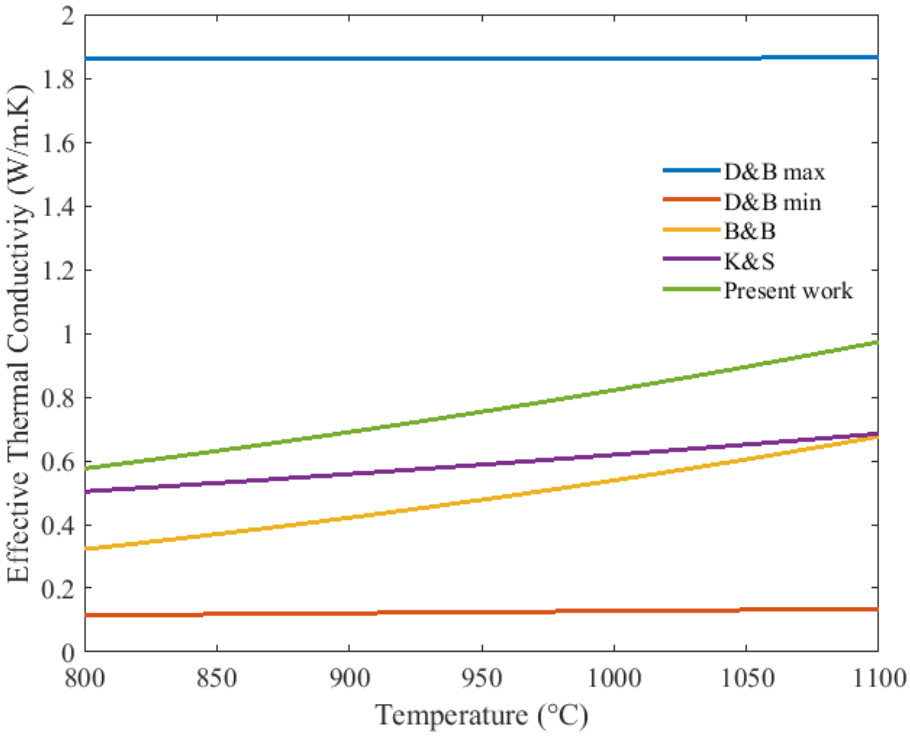

Figure 5.10 Comparison of the proposed effective thermal conductivity with published correlations

5.6 Summary

In this chapter, an experimental study was carried out for heat transfer at temperatures between 800 and 1100 °C in a lab-scale reactor that is directly heated by an electrical IR furnace. The reactor was packed with spherical 0.5 to 1 mm iron–manganese oxide particles having an

Fe/Mn molar ratio of 2:1. Both steady-state and transient heat transfer behaviour of the bed were investigated where no chemical reaction occurs during the heating. Non-linear regression was used to calculate the effective heat transfer parameters of the packed bed under steady-state conditions using a 2D model. The modelling results showed that the calculated effective parameters are capable of predicting the transient temperatures obtained experimentally. Furthermore, the temperature-dependent effective thermal conductivity derived here is in good agreement with a number of correlations reported in the literature.

6 Thermochemical performance of the packed-bed reactor [1]

6.1 Introduction

In this chapter, the thermochemical performance of the packed-bed reactor during the reduction reaction is investigated. The reactor model consists of heat transfer (conduction, convection, and radiation), mass transfer, and thermochemical reaction kinetics. The experimental data consist of continuous measurements of gas concentrations exiting the reactor.

To simulate the reduction reaction of iron–manganese oxide particles in the packed-bed reactor, reliable kinetic model and transport parameters are required. The reduction reaction kinetics and the reaction enthalpy of iron–manganese oxide particles were achieved in Chapter 4. Furthermore, the effective heat transfer parameters of the reactor—effective thermal conductivity and wall heat transfer coefficient—were calculated in Chapter 5.

The simulation is performed using a transient two-dimensional pseudo-homogenous model. The temperature distribution, conversion, reaction rate, and concentration variations with time are analysed. The modelling results are validated with the experimental data.

6.2 Experimental description

6.2.1 Experimental setup

The reactor is composed of a vertical tube packed with spherical active particles to a height of 3 cm. The tube is made of alumina (extruded alumina > 99.7%, Ceramic Oxide Fabricators) and has outer and inner diameters of 26 mm and 21 mm, respectively. The particles are placed

[1] Material in this Chapter has been internally reviewed and is ready for submission: M. Hamidi, V.M. Wheeler, X. Gao, J. Pye, K. Catchpole, A.W. Weimer., "Reduction of iron-manganese oxide particles in a lab-scale packed-bed reactor for thermochemical energy storage", *Chemical Engineering Science*

on top of an alumina disc which is supported by another tube with outer and inner diameters of 20 mm and 15 mm, respectively. A thin layer of zirconia felt is placed on top of the disc to prevent particle loss. The tube is placed in the centre of an electric IR furnace (P4C-VHT, Advance Riko) and surrounded by a quartz tube to protect the IR lamps against thermal degradation. The furnace is composed of 4 IR lamps (2kw each) with a 40 mm opening diameter and heating length of 100 mm. Two type K thermocouples (Inconel 600, 1.5 mm diameter, Temperature Controls) are installed in the reactor. One of the thermocouples measures the tube wall temperature at the height of 1.5 cm from the disc. The wall temperature is used as the setpoint temperature for the furnace. The other thermocouple measures the temperature of the alumina disc.

Figure 6.1 illustrates a photograph of the experimental setup and the process flowsheet. Gas flowrates are adjusted by means of two mass flow controllers (F-201CV, Bronkhorst) before being delivered to the top of the reactor. A quadrupole mass spectrometer (OmniStarTM GSD 320, Pfeiffer Vacuum) is used to record the concentration of oxygen of downstream the reactor in order to track the reaction progress. The oxygen gas component is calibrated in the mass spectrometer using standard mixtures of oxygen in the carrier gas of argon.

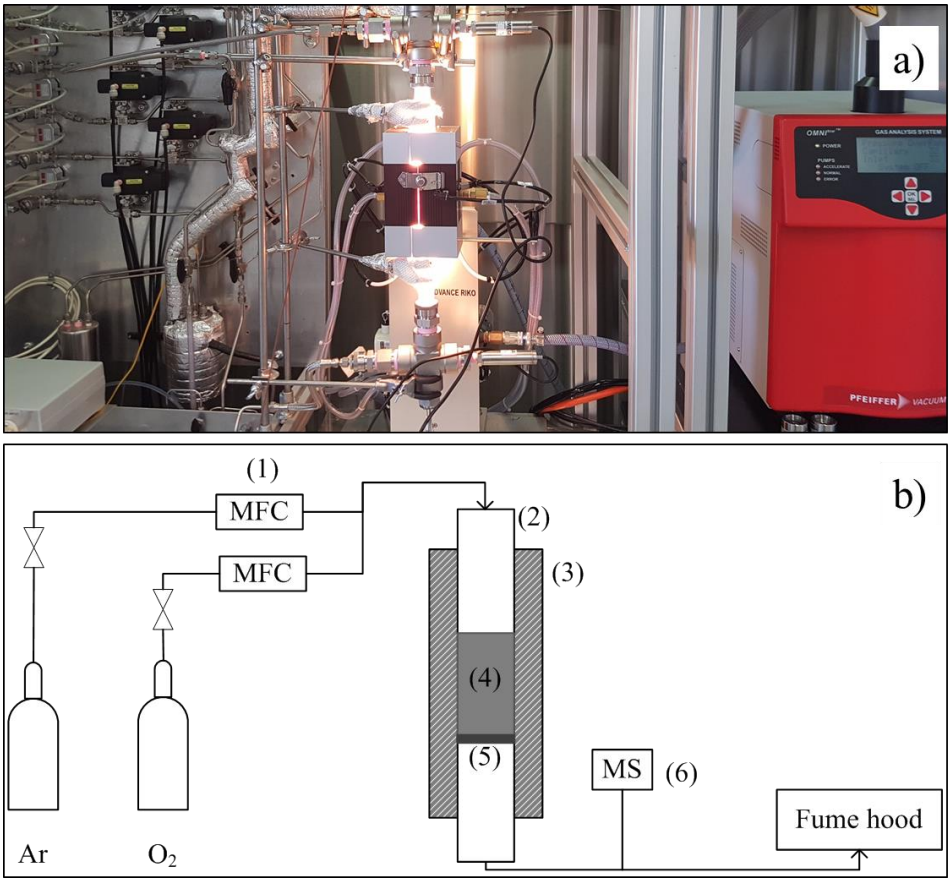

Figure 6.1 a) photograph of physical setup, and b) process flowsheet: (1) mass flow controller, (2) alumina tube, (3) furnace, (4) packed particles, (5) alumina disc, and (6) mass spectrometer

6.2.2 Experimental procedure

The setup is initially purged of air under pure argon (COREGAS grade 5.0) at room temperature. The reactor is then heated from the ambient room temperature to 1200 °C at a heating rate of 10 °C/min while argon gas with a flowrate of 100 mL/min is flowing through the bed from top to the bottom. The maximum temperature of 1200 °C is chosen based on the thermodynamic and kinetic study of iron–manganese oxide particles in Chapter 4. During heating, the exit gas is continuously analysed by the MS. After heating, the reactor is cooled to room temperature at 50 °C/min using an external cooling system under argon gas. Finally, the reacted particles are collected from the reactor for XRD test.

6.3 Reactor modelling

The packed-bed reactor model is based on general conservation relations for mass and energy considering effective transport parameters. A dynamic, two-dimensional, pseudo-homogenous model based on a shell balance method has been developed (Appendices B and D). The model used is given as follows:

Energy balance for the solid–gas mixture

$$-\rho_g c_{p,g} u_z^s \frac{\partial T}{\partial z} + \frac{\partial}{\partial z}(k_{eff} \frac{\partial T}{\partial z}) + \frac{1}{r}\frac{\partial}{\partial r}(k_{eff} r \frac{\partial T}{\partial r}) - \rho_s (1-\varepsilon_b) r_{O_2} \Delta H = (\varepsilon_b \rho_g c_{p,g} + (1-\varepsilon_b)\rho_s c_{p,s}) \frac{\partial T}{\partial t}$$

(6.1)

Mole balance for oxygen in the gas phase

$$-u_z^s \frac{\partial C_{O_2}}{\partial z} + \varepsilon_b \frac{\partial}{\partial z}(D_{eff} \frac{\partial C_{O_2}}{\partial z}) + \varepsilon_b \frac{1}{r}\frac{\partial}{\partial r}(rD_{eff} \frac{\partial C_{O_2}}{\partial r}) + \rho_s (1-\varepsilon_b) r_{O_2} = \varepsilon_b \frac{\partial C_{O_2}}{\partial t} \qquad (6.2)$$

Mole balance for argon in the gas phase

$$-u_z^s \frac{\partial C_{Ar}}{\partial z} + \varepsilon_b \frac{\partial}{\partial z}(D_{eff} \frac{\partial C_{Ar}}{\partial z}) + \varepsilon_b \frac{1}{r}\frac{\partial}{\partial r}(rD_{eff} \frac{\partial C_{Ar}}{\partial r}) = \varepsilon_b \frac{\partial C_{Ar}}{\partial t} \qquad (6.3)$$

where ρ and c_p are mass density and specific heat capacity; *z* and *r* are the axial and radial coordinates, respectively; *t* is the time; ε_b is void fraction of the bed; and u_z^s is superficial gas velocity in *z* direction which is equal to the volumetric flow rate of the gas divided by the cross sectional area of the bed. Subscripts *s* and *g* represent solid and gas phase, respectively. k_{eff} and D_{eff} are effective thermal conductivity and effective diffusivity where "effective" identifies the apparent parameters accounting for transport phenomena in a homogenized, multi-phase

media. r_{O_2} and ΔH are the reaction rate of oxygen generation and the enthalpy of reaction, respectively.

The corresponding initial and boundary conditions are

$$\text{at} \quad t=0 \quad T(r,z,0)=T_0 \quad C_{O_2}(r,z,0)=0 \quad C_{Ar}(r,z,0)=C_{Ar,0} \tag{6.4}$$

$$\text{at} \quad z=L \quad \rho_g c_{p,g} u_z^s T - k_{eff}\frac{\partial T}{\partial z} = A_2 F_{21}\sigma\varepsilon_{r,w}T_w^4 / A_1 - \varepsilon_{r,s}\sigma T^4 \quad C_{O_2}=0 \quad C_{Ar}=C_{Ar,in} \tag{6.5}$$

$$\text{at} \quad z=0 \quad T=T_{disc} \quad \frac{\partial C_{O_2}}{\partial z}=0 \quad \frac{\partial C_{Ar}}{\partial z}=0 \tag{6.6}$$

$$\text{at} \quad r=R \quad -k_{eff}\frac{\partial T}{\partial r}=h_w(T-T_w) \quad \frac{\partial C_{O_2}}{\partial r}=0 \quad \frac{\partial C_{Ar}}{\partial r}=0 \tag{6.7}$$

$$\text{at} \quad r=0 \quad \frac{\partial T}{\partial r}=0 \quad \frac{\partial C_{O_2}}{\partial r}=0 \quad \frac{\partial C_{Ar}}{\partial r}=0. \tag{6.8}$$

The emissivity of the wall and solid particles are given by $\varepsilon_{r,w}$ and $\varepsilon_{r,s}$, respectively; σ is the Stefan-Boltzmann constant; and T_w is the wall temperature. The first term on the right-hand side of Equation (6.5) represents the radiation from the tube wall above the bed that is absorbed by the top surface. F_{21} is the fraction of energy leaving the wall and reaching the surface of the bed. The second term on the right-hand side of the Equation (6.5) is the radiation emitted by the top surface. In equation (6.7), h_w is the effective wall heat transfer coefficient.

The reaction rate of iron–manganese oxide reduction was developed in Chapter 4. The reaction rate based on generation of oxygen in equation (6.9) is valid under inert atmosphere

$$r_{O_2}=\frac{33.5}{M_{O_2}}(1.475\times10^{14}\frac{1}{s})\exp(-\frac{426.13\frac{\text{kJ}}{\text{mol}}}{RT})\frac{3(1-\alpha)^{2/3}}{2\left[1-(1-\alpha)^{1/3}\right]}, \tag{6.9}$$

where M_{O_2} is the molecular weight of oxygen, R is the universal gas constant, and α is the reaction conversion (reaction extent).

Table 6.1 presents the parameters and auxiliary correlations used for simulations displayed in this study. The reactor specifications are the same as those used to obtain observations in absence of reaction.

Table 6.1 Packed bed, particle, and gas specifications

Parameter	**Value/correlation**	**Reference**
Particle diameter (mm)	$d_p = (0.5-1)\times10^{-3}$	
Bed height (m)	$H = 3\times10^{-2}$	
Bed diameter (m)	$D = 2.1\times10^{-2}$	
Bed void fraction (-)	$\varepsilon_b = 0.383 + 0.254\left(\frac{D}{d_p}\right)^{-0.923} . \frac{1}{(0.723\frac{D}{d_p}-1)^{0.5}}$	Roshani[88]
Heat capacity of particle (J/mol.k)	$c_{p,s} = -1853512\times T^{-2} + 144.76640 + 8.593936\times10^{-2}\times T$	Bale et al.[51]
Heat capacity of argon (J/mol.k)	$c_{p,g} = 20.786$	Bale et al. [51]
Density of particle (kg/m^3)	$\rho_s = 5\times1000$	
Reaction enthalpy (J/mol)	$\Delta H = 1.9104\times10^5$	Chapter 4
Effective thermal conductivity (W/m.K)	$k_{eff} = 2.94\times10^{-10}T^3 - 1.59\times10^{-7}T^2 + 3.87\times10^{-4}T + 0.11$	Chapter 5
Wall heat transfer coefficient (W/m^2.K)	$h_w = 0.109T_w - 1.13\times10^2$	Chapter 5

Diffusivity for binary A-B gas mixture (cm^2/s)	$\frac{pD_{AB}}{(p_{cA}p_{cB})^{1/3}(T_{cA}T_{cB})^{5/12}(1/M_A+1/M_B)^{1/2}} = a\left(\frac{T}{\sqrt{T_{cA}T_{cB}}}\right)^b$	Bird et al.[94]
Effective diffusivity (m^2/s) (Due to tortuosity)	$D_{eff} = \frac{\varepsilon_b}{1-\ln \varepsilon_b / 2} D_{AB} \times 10^{-4}$	

6.4 Results and discussion

To ensure that the reduction reaction has been completed in the packed-bed reactor, XRD is performed on the particles before and after the experiment. The crystalline phase composition is presented in Figure 6.2. The XRD patterns show a bixbyite phase (cubic Mn_2O_3; PDF#41-1442) for the initial material, and a spinel jacobsite phase (cubic $MnFe_2O_4$; PDF#74-2403) for the material after reaction. No trace of Bixbyite phase in the XRD pattern after reaction confirms that the particles are fully reduced and that the reaction has been completed. A scanning electron micrograph (SEM) showing the shape and size of the particles is also presented in this figure.

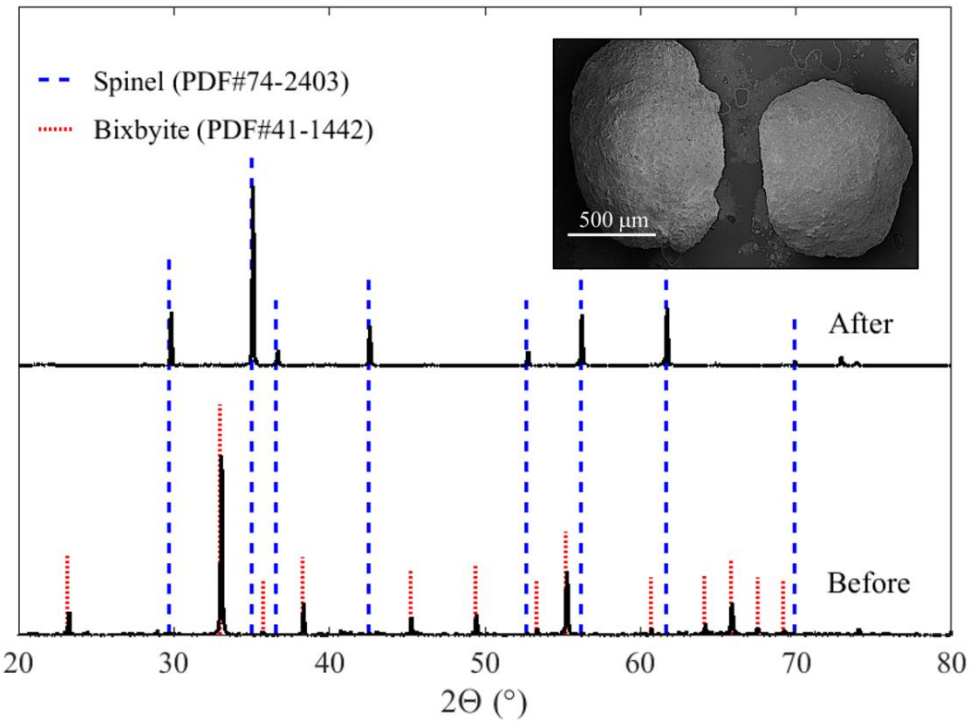

Figure 6.2 XRD patterns of particles before and after reduction in the packed-bed reactor and SEM image of the initial material

The transient 2D governing equations (6.1), (6.2), and (6.3) along with their boundary conditions and auxiliary equations have been solved in a MATLAB environment. A solution of the model at time equals to 100 min is shown in Figure 6.3. The temperature gradient is much larger in the axial direction than the radial direction since the top boundary is exposed to radiation from the tube above the bed while the bottom boundary is shielded by zirconia felt and an alumina disc. More details about heat transfer of the reactor can be found in Chapter 5. As we were expecting, conversion is directly correlated with temperature, higher yields at higher temperatures. The reaction rate is the highest at around 70% of conversion. More details about the reaction kinetics of iron-manganese oxide particles can be found in Chapter 4. Concentration of oxygen in the gas phase increases from top to the bottom of the reactor due to the gas flow in this direction (convective mass transfer).

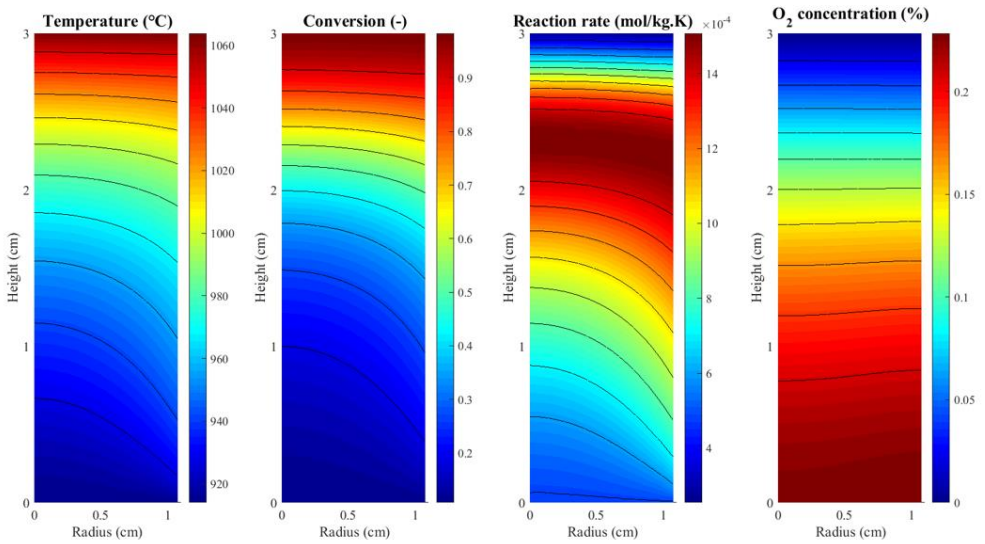

Figure 6.3 Spatial distribution of temperature, conversion reaction rate, and O_2 concentration at time = 100 min depicted as 2D colour maps.

A comparison for the temperature predictions with and without reaction is presented in Figure 6.4. As we expected, temperature decreases noticeably with the presence of chemical reaction due to its endothermic nature. The gap between the two temperature profiles is the highest when the reaction rate is at its maximum, at approximately 70% conversion (Figure 6.4b).

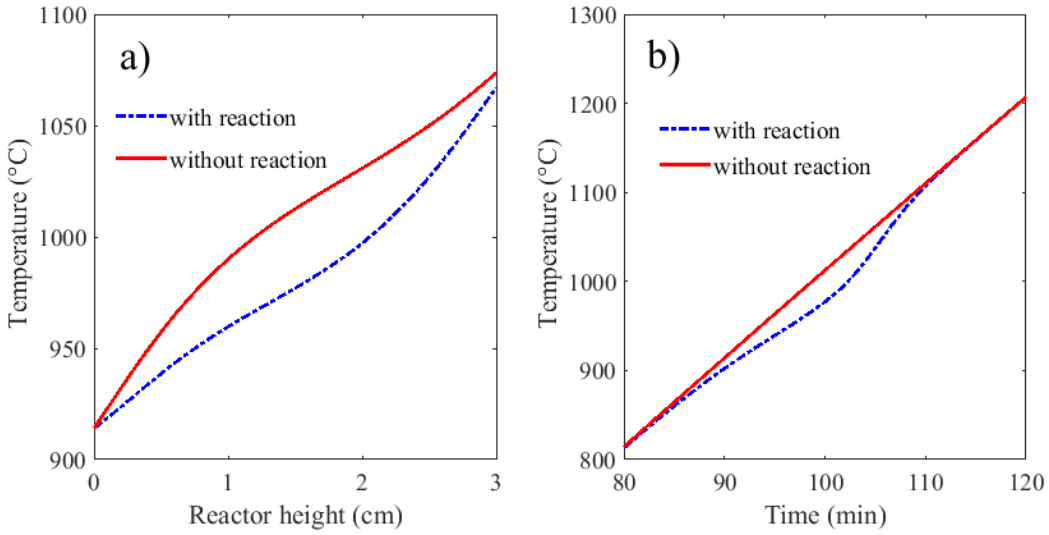

Figure 6.4 Temperature profiles with and without reaction a) along the reactor center at time=100 min, and b) at the location r=0, z=1.5 cm versus time

The modeling results for the concentration of oxygen in the gas phase at different times is shown in Figure 6.5. As observed, oxygen concentration first increases and then decreases with time in both figures. Oxygen concentration is zero at the reactor inlet (z = 3cm) and increases along the reactor (Figure 6.5a). The slope of the concentration profile is higher at a time of 100 min compared to a time of 90 min, indicative of greater oxygen production. At a time of 110 min, the oxygen concentration is zero from the reactor entrance to approximately the middle of the reactor. Thereafter, the concentration increases since the particles at the bottom of the reaction zone are reacting.

Oxygen concentration remains almost uniform along the reactor radius (Figure 6.5b).

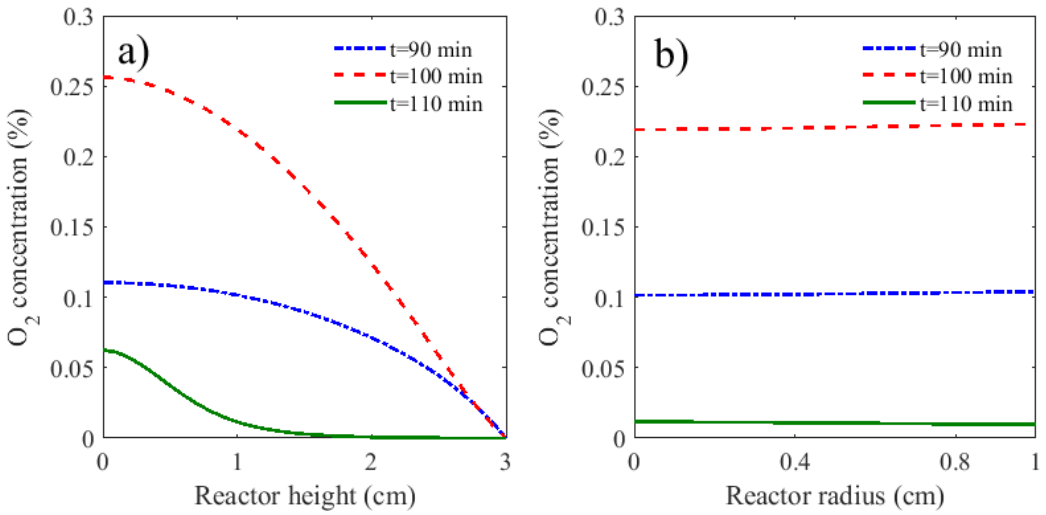

Figure 6.5 O_2 concentration in percentage a) along the reactor center and b) versus reaction radius at z=0.5 cm for different times

Validity of the model was verified by comparing the modelled oxygen concentration at the reactor exit with the experimental values measured downstream of the reactor using a MS (Figure 6.6). The thermochemical performance of the reactor predicted by the model is in

agreement with the experimental data, except at the very beginning of the reaction. We believe that the under-prediction of oxygen concentration by the model at the beginning of the reaction is due to the high flux of infrared radiation on the top surface of the bed being emitted from the alumina tube. Iron-manganese oxide particles could be semitransparent to radiation at these wavelengths, which means the radiation can penetrate the particles and cause a volumetric heat generation within them. This semitransparency effect of the particles is not included in the transport model or the kinetic model—a shrinking core model—and could lead to a more localized heating at the surface before conduction becomes the dominant thermal transport mechanism. The small reactor size and also the heating zone that extends above the bed used here makes this effect prominent. However, in larger reactors—as would be deployed at industrial scale—the size of the bed would be larger and the heating zone could be controlled to not irradiate outside of the bed, so this phenomenon should become negligible. Both model and the experimental data show 100% conversion at the end of the reaction. Both the model and experimental data show 100% conversion at the end of the reaction.

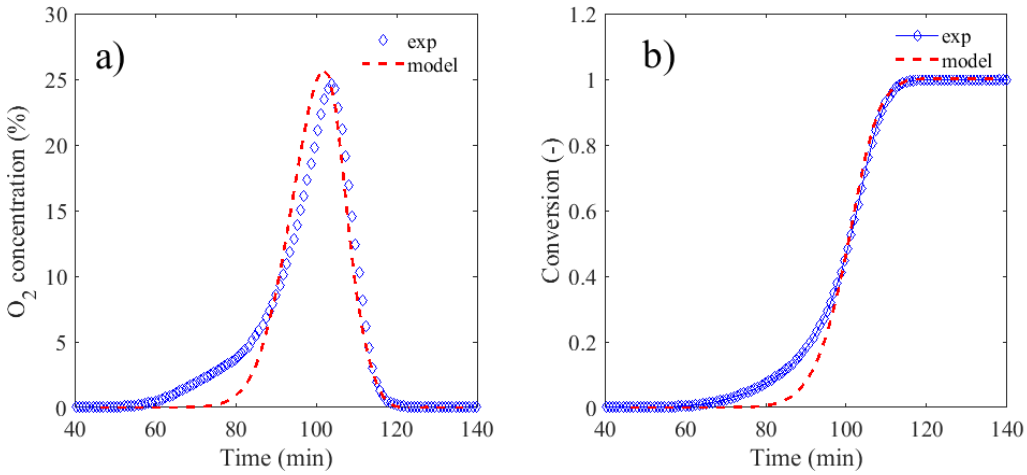

Figure 6.6 Measured and modelled a) O_2 concentration (%) at the reactor exit and b) total conversion of the reactor

6.5 Summary

This Chapter presented the reduction reaction of iron–manganese oxide particles in a directly heated packed-bed reactor, supported by both experimental and modelling results. A transient, two-dimensional, pseudo-homogenous model was established for the reactor. The model was comprised of heat transfer (conduction, convection, and radiation), mass transfer, and thermochemical reaction. The experimental data consisted of the reactor effluent measurements, which was recorded continuously using a mass spectrometer. The validation of the reactor model with experimental data demonstrated that the previously derived temperature-dependent heat transfer parameters, reaction enthalpy, and reaction rate expression from Chapters 4 and 5 are capable of predicting the performance of a real-world pilot reactor.

7 Conclusions and future work

To meet the worldwide electricity demand using renewable sources, technologies must be developed that can both harvest and store the abundance of solar energy. Thermochemical energy storage systems based on metal oxides present an attractive solution. These systems have operating temperatures that are compatible with concentrated solar energy power plants. Furthermore, they are environmentally benign and plentiful, ensuring a sustainable energy solution.

Research efforts have identified promising metal oxides and corresponding proof-of-concept reactor designs. To move towards commercializing solar thermochemical energy storage, this work has involved the design and construction of a directly heated packed-bed reactor. Coupled to a well-studied metal oxide, we studied the reactor's thermochemical performance. A computational code in MATLAB environment was developed to solve governing equations of the system. This enabled analysis of the thermal reduction step in the thermochemical cycle, which provided insights into the dynamics of the temperature, reaction rate, and mass fraction throughout the reactive medium. To develop a reactor model, reliable kinetic model and heat transfer parameters were obtained experimentally. To this end, the solid–gas reaction model was developed, and the thermal performance of the reactor was evaluated. The shrinking core model consists of chemical reaction, internal diffusion, and external diffusion steps could describe the reaction of large spherical iron-manganese oxide particles. Through this, the reaction rate expression was developed and compared with experimental data for the non-isothermal reduction of iron–manganese oxide.

Heat transfer in the packed-bed reactor was studied within the temperature range of 800 to 1100 °C without reaction. A pseudo-homogenous two-dimensional model along with temperature-dependent heat transfer parameters—effective thermal conductivity and wall heat transfer coefficient—were found to predict the experimental data very well. Comparing the computed parameters with existing correlations found in the literature also further proved the validity of the parameters.

The developed reaction and reactor models in this work can be readily extended to other configurations, operating conditions, and solid–gas reactions. Therefore, many opportunities exist to continue and/or expand this work. Within the context of solid–gas reactions for solar thermochemical energy storage, the effect of different operating conditions and particle morphology should be further explored to gain a better understanding of the iron-manganese oxide reaction. For example, particle size is an important parameter that can affect the reaction rate. In this work, inert and air atmospheres were the only conditions where reaction kinetics was investigated. Exploring the effect of atmospheres with different partial pressure of oxygen would give improved estimates to the reaction rate. The focus of this work was only on the reduction step of the cycle. Therefore, the oxidation step of the thermochemical redox reaction should also be studied in the near future.

Based on the findings of this study, temperature-dependent heat transfer parameters can predict the thermal performance of the reactor for specific operating conditions. In addition to collecting more experimental data in the packed area closer to the wall, the use of two-phase heat transfer simulation may further improve the model.

Appendices

Appendix A, solid-gas reaction kinetics

A.1 Isoconversional methods

Isoconversional approaches are reliable methods to calculate activation energy of a solid–gas reaction without making any assumptions about the reaction model.[95, 96] All isoconversional methods require determination of temperatures at equivalent reaction extents for various heating rates.[96] These methods are based on the isoconversional principle, which states that, at a constant conversion, reaction rate is just a function of temperature.[67] This principle can be demonstrated by taking natural logarithms on both sides of equation (2.9)

$$\ln\left(\frac{\mathrm{d}\alpha}{\mathrm{d}t}\right) = \ln\left(k\left(T\right)\right) + \ln\left(f\left(\alpha\right)\right). \tag{A.1}$$

Then, differentiating respect to $1/T$ assuming constant conversion gives

$$\left[\frac{\partial}{\partial T^{-1}}\ln\left(\frac{\mathrm{d}\alpha}{\mathrm{d}t}\right)\right]_{\alpha} = \left[\frac{\partial \ln\left(k\left(T\right)\right)}{\partial T^{-1}}\right]_{\alpha} + \left[\frac{\partial \ln\left(f\left(\alpha\right)\right)}{\partial T^{-1}}\right]_{\alpha}. \tag{A.2}$$

The second term on the right side is zero since α is constant and $f(\alpha)$ is just a function of conversion

$$\left[\frac{\partial}{\partial T^{-1}}\ln\left(\frac{\mathrm{d}\alpha}{\mathrm{d}t}\right)\right]_{\alpha} = \left[\frac{\partial \ln\left(k\left(T\right)\right)}{\partial T^{-1}}\right]_{\alpha}. \tag{A.3}$$

Replacing the Arrhenius function (equation (2.10)) in the above equation we have

$$\left[\frac{\partial}{\partial T^{-1}}\ln\left(\frac{\mathrm{d}\alpha}{\mathrm{d}t}\right)\right]_{\alpha}=\left[\frac{\partial}{\partial T^{-1}}\ln\left(A\exp\left(-\frac{E}{RT}\right)\right)\right]_{\alpha}=\ln A-\frac{E}{RT}. \tag{A.4}$$

Therefore,

$$\left[\frac{\partial}{\partial T^{-1}}\ln\left(\frac{\mathrm{d}\alpha}{\mathrm{d}t}\right)\right]_{\alpha}=-\frac{E}{R}. \tag{A.5}$$

This equation states that by having the isoconversional reaction rate as a function of temperature, the activation energy can be evaluated without assuming any specific reaction model. That is why isoconversional methods are also called “model-free” methods.

E is usually calculated in the range of $\alpha=0.05-0.09$, with a step of not larger than 0.05. The calculated activation energy is a function of conversion in the isoconversional methods. If the value of E changes significantly with α, it indicates that the reaction is kinetically complex and a single-step reaction rate cannot describe the whole process.

Isoconversional methods are divided into two categories: differential and integral. In differential isoconversional methods, there is no mathematical approximation while most of integral isoconversional methods are based on approximations for the temperature integral.[95, 96]

Friedman equation is an example of differential isoconversional methods. Although this simple computational method is applicable to a wide range of temperature programs, this method is unfortunately rarely used in actual kinetic studies.[67] By taking natural logarithm from equation (2.11) and applying the isoconversional principle we have

$$\ln\left(\frac{\mathrm{d}\alpha}{\mathrm{d}t}\right)_{\alpha,i}=\ln\left(A\exp\left(-\frac{E}{RT_{\alpha,i}}\right)\right)+\ln\left(f\left(\alpha\right)\right). \tag{A.6}$$

where the subscript α states that values are at constant conversion, and i is the index representing each temperature program. Simplifying and rearranging the equation above

$$\ln\left(\frac{\mathrm{d}\alpha}{\mathrm{d}t}\right)_{\alpha,i} = \ln\left[A_\alpha f(\alpha)\right] - \frac{E}{RT_{\alpha,i}}. \tag{A.7}$$

The value of activation energy at each conversion is determined from the slope of the plot $\ln\left(\mathrm{d}\alpha/\mathrm{d}t\right)_{\alpha,i}$ versus $1/T_{\alpha,i}$. Friedman equation often changes to the form below for linear non-isothermal processes[81, 96, 97]

$$\ln\left(\beta_i \frac{\mathrm{d}\alpha}{\mathrm{d}T}\right)_{\alpha,i} = \ln\left[A_\alpha f(\alpha)\right] - \frac{E_\alpha}{RT_{\alpha,i}}, \tag{A.8}$$

where β_i is the heating rate of the ith run.

Differential isoconversional methods have the advantage that they do not use approximation. Nevertheless, these methods are not accurate when the reaction heat changes with the heating rate and they require numerical differentiation on the experimental data which may introduce noise in the reaction rate values.

Integral isoconversional methods originate from the application of the isoconversionasl principle into integral form of the reaction rate (equation (2.13)). The challenge of these methods is that the integral in the left side of the equation (2.13) does not have an analytical solution when the temperature program is not isothermal. For non-isothermal experiments with constant heating rate, a number of integral isoconversional methods that are based on various approximations have been proposed. Almost all of these approximations lead to a linear equation with the form

$$\ln\left(\frac{\beta_i}{T_{\alpha,i}^{B}}\right) = const - C\left(\frac{E}{RT_\alpha}\right), \tag{A.9}$$

where B and C are the parameters that depend on the approximation method. Three known examples of integral isoconversional methods for non-isothermal experiments with constant heating rates are presented here.

Flynn-Wall-Ozawa method [67, 96-98] is also known as Ozawa method. Values of B and C in equation (A.9) are zero and 1.052, respectively in this method. Due to poor approximation considered for the temperature integral, this method is the least accurate integral isoconversional method

$$\ln\left(\beta_i\right) = const - 1.052\left(\frac{E}{RT_\alpha}\right). \tag{A.10}$$

Kissinger-Akahira-Sunose method [67, 97, 98 95] is also known as KAS. In this equation, B is 2 and C is 1. This equation is sometimes called the generalized Kissinger method and is identical to the method described by Vyazovkin and co-workers[96]

$$\ln\left(\frac{\beta_i}{T_{\alpha,i}^{2}}\right) = const - \frac{E}{RT_\alpha}. \tag{A.11}$$

Starink method[67, 95, 96] in which B is 1.92 and C is 1.0008. This method is the most accurate integral isoconversional method based on approximation

$$\ln\left(\frac{\beta_i}{T_{\alpha,i}^{1.92}}\right) = const - 1.0008\left(\frac{E}{RT_\alpha}\right). \tag{A.12}$$

The accuracy of integral isoconversional methods can be further increased by calculating the activation energy numerically instead of using approximation. This method is non-linear and

has been generally used less frequently compared to the other methods due to its mathematical complexity.[96] Vyazovkin proposed an approach to calculate the activation energy numerically by minimizing the following function[67, 71]

$$\Phi(E) = \sum_{i=1}^{n} \sum_{j \neq i}^{n} \frac{I(E, T_{\alpha,i}) \beta_j}{I(E, T_{\alpha,j}) \beta_i}, \tag{A.13}$$

where the temperature integral is solved numerically and is

$$I(E, T_\alpha) = \int_0^{T_a} \exp(\frac{-E}{RT}) dT . \tag{A.14}$$

Vyazovkin showed that by using this method, the relative error in activation energy is lower than approximation methods. Equation (A.13) can be only used for the non-linear experiments with constant heating rate. Nonetheless, this approach has the capability of being used for any other temperature programs when the numerical integration is with respect to time instead of temperature. For a series of runs conducted under different temperature programs

$$\Phi(E) = \sum_{i=1}^{n} \sum_{j \neq i}^{n} \frac{J(E, T_i(t_\alpha))}{J(E, T_j(t_\alpha))} , \tag{A.15}$$

where the integral with respect to time is

$$J(E, T(t_\alpha)) = \int_0^{t_a} \exp\left(\frac{-E}{RT(t)} \right) dt . \tag{A.16}$$

A.2 Kissinger method

Kissinger method is another technique for activation energy calculation. This method is based on the assumption that the maximum rate of the reactions occurs approximately at a specific conversion.[96] Kissinger equation is derived from equation (2.11) by considering the assumption that the maximum reaction rate happens where the second derivative is zero

$$\frac{d^2\alpha}{dt^2} = \left[\frac{E\beta}{RT_m^2} + Af'(\alpha_m)\exp\left(\frac{-E}{RT_m}\right)\right]\left(\frac{d\alpha}{dt}\right)_m = 0, \quad \text{(A.17)}$$

where subscript m denotes the values related to the maximum rate and $f'(\alpha) = df(\alpha)/d\alpha$. By simplifying and rearranging equation (A.17)

$$\frac{E\beta}{RT_m^2} = -Af'(\alpha_m)\exp\left(\frac{-E}{RT_m}\right). \quad \text{(A.18)}$$

Taking natural logarithm of the equation above

$$\ln\left(\frac{\beta}{T_{m,i}^2}\right) = \ln\left(-\frac{AR}{E}f'(\alpha_m)\right) - \frac{E}{RT_{m,i}}. \quad \text{(A.19)}$$

The activation energy can be simply obtained by plotting $\ln(\beta/T_m^2)$ versus $1/T_m$. Kissinger method has limitations that includes the computation of just a single value for activation energy for any reaction and being only applicable to the temperature programs with constant heating rates. Despite the limitations this method has, it has been applied often in the literature because of its ease of use.[67]

A.3 Kinetic compensation effect method

Kinetic compensation effect[67, 70, 99, 100] (also known as method of invariant kinetic parameters) states that for a single experimental run, there is a linear correlation between the activation energy and the pre-exponential factor computed based on different reaction functions of i

$$\ln A_i = aE_i + b. \quad \text{(A.20)}$$

This relationship is called “compensation” because a change in the activation energy or the pre-exponential factor is compensated by a change in the other. Substituting different reaction models into the rate equation and applying model fitting (linear or nonlinear) gives different

pairs of E and $\ln A$. Although the values of these parameters vary significantly with $f_i(\alpha)$, they all can fit in the equation (A.20) with the constant values of a and b. Therefore, the parameters a and b are independent of the reaction function while they depend on the heating rate.

Each heating rate gives a unique pair of a and b. Employing all these pairs from different heating rates β_j, a unique pair of E and $\ln A$ can be obtained.

$$b_j = \ln A + Ea_j \tag{A.21}$$

Although this method gives E and $\ln A$ values simultaneously, it is rarely used as it requires more computations compared to other methods.

A.4 Master plots

Master plots are theoretical curves used to determine the mechanism of solid–gas reactions. They detect the reaction mechanism by comparing experimental master curves with theoretical master curves of various kinetic models. To use the master plot technique, the activation energy of the reaction needs to be known. Isoconversional methods can be used to determine this parameter. The value of activation energy should not vary much with conversion since the average value of E will be employed in master plot. Master plots can be used for isothermal data, linear non-isothermal data, and non-linear non-isothermal data. In this section, the focus is on linear non-isothermal data.

Master Plot methods come in the form of three types, based on the form of reaction rate equation that is used; they can have integral form, differential form, or the combination of differential and integral forms of the reaction rate.

Master plot type 1 originates from the differential form of reaction rate. By rearranging equation (2.11)

$$Af(\alpha) = \frac{\mathrm{d}\alpha}{\mathrm{d}t}\exp\left(\frac{E}{RT}\right). \tag{A.22}$$

Since the pre-exponential factor is unknown in the equation above, both sides of the equation are divided by a reference point (here $\alpha = 0.5$ is used) to obtain a correlation which is independent of pre-exponential factor. Then

$$z_1(\alpha) = \frac{f(\alpha)}{f(0.5)} = \frac{\mathrm{d}\alpha/\mathrm{d}t}{(\mathrm{d}\alpha/\mathrm{d}t)_{\alpha=0.5}} \frac{\exp(E/RT)}{\exp(E/RT_{\alpha=0.5})}. \tag{A.23}$$

By plotting theoretical (left side) and experimental (right side) values of $z_1(\alpha)$ versus α, the best reaction model matched with experimental data can be identified. A series of experimental $z_1(\alpha)$ can be plotted for different heating rates. These plots should not demonstrate a significant deviation for different heating rates.

Master plot type 2 originates from the integral form of reaction rate. From equation (2.13)

$$g(\alpha) = A\int_0^t \exp\left(-\frac{E}{RT}\right)\mathrm{d}t. \tag{A.24}$$

As was mentioned before, the integral part in the right-hand side of the equation above does not have an analytical solution for non-isothermal processes. For linear non-isothermal data, the integral part can be calculated using approximation methods

$$\int_0^t \exp\left(-\frac{E}{RT}\right)\mathrm{d}t = \frac{1}{\beta}\int_0^T \exp\left(-\frac{E}{RT}\right)\mathrm{dT} = \frac{E}{R\beta}\int_x^\infty \frac{\exp(-x)}{x^2}dx = \frac{E}{R\beta}p(x), \tag{A.25}$$

where $x = E/RT$. Then

$$g(\alpha) = \frac{AE}{R\beta} p(x) . \tag{A.26}$$

Similar to master plot type 1, both sides of this equation are divided by a reference value to make this correlation independent of the pre-exponential factor.

$$Z_2(\alpha) = \frac{g(\alpha)}{g(0.5)} = \frac{p(x)}{p(0.5)} . \tag{A.27}$$

Different series have been suggested for the approximation of $p(x)$ function. Here, we use the fourth rational approximation of Senum and Yang, corrected by Flynn[101]

$$p(x) = \frac{\exp(-x)}{x} \pi(x) , \tag{A.28}$$

where

$$\pi(x) = \frac{x^3 + 18x^2 + 86x + 96}{x^4 + 20x^3 + 120x^2 + 240x + 120} . \tag{A.29}$$

The third type of master plots is derived by combining integral and differential forms of the reaction rate

$$z_3(\alpha) = g(\alpha) f(\alpha) = \frac{AE}{R\beta} p(x) \frac{1}{A} \left(\frac{\mathrm{d}\alpha}{\mathrm{d}t} \right) \exp\left(\frac{E}{RT} \right) . \tag{A.30}$$

Replacing $p(x)$ from equation (A.28)

$$z_3(\alpha) = g(\alpha) f(\alpha) = \left(\frac{\mathrm{d}\alpha}{\mathrm{d}t} \right) \frac{T}{\beta} \pi(x) . \tag{A.31}$$

The experimental values of $z_3(\alpha)$ (right side of the equation above) should be plotted as a function of α and compared with the theoretical plots of $z_3(\alpha)$ (left-hand side of the equation above). The reaction model that best fits the experimental data is identified as the reaction

mechanism. The main advantage of the master plot type 3 over type 1 and 2 is that it does not have a pre-exponential term in it. Therefore, it does not require a reference value or normalization, thus gives a more accurate result.

Appendix B, 2D heat transfer model derivation for a packed-bed reactor

A shell balance method is employed to derive a dynamic pseudo-homogenous two-dimensional heat transfer model for a vertical packed-bed reactor. Figure B.1 shows a schematic diagram of the element

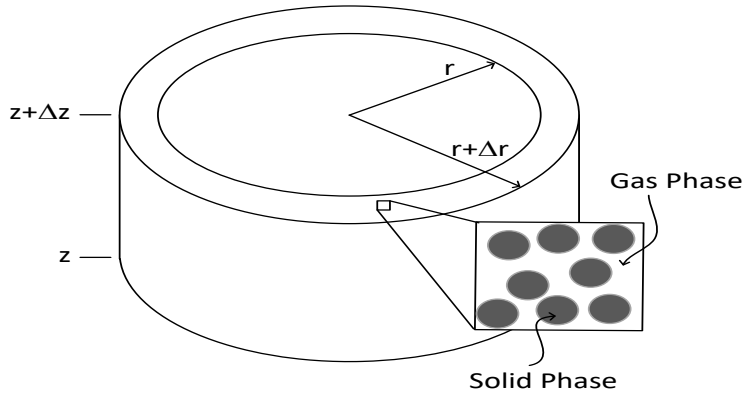

Figure B.1 Schematic diagram of elemental volume of the packed-bed reactor

Based on this element

Area normal to r direction: $A_r = 2\pi r\Delta z$

Area normal to z direction: $A_z = 2\pi r\Delta r$

Volume of the element: $\Delta V = 2\pi r\Delta r\Delta z$

Figure B.2 shows the energy transport in the elemental volume where q, q' and q'' are conductive, convective and radiative heat flux, respectively.

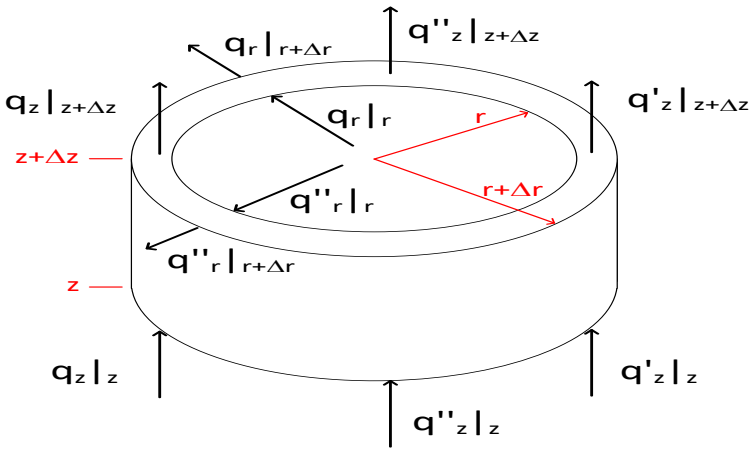

Figure B.2 Energy transport in the packed-bed reactor element

Applying the law of conservation of energy to the elemental volume for a dynamic system we have

$$\left\{\begin{matrix}\text{rate of energy in by}\\ \text{convective transport}\end{matrix}\right\}-\left\{\begin{matrix}\text{rate of energy out by}\\ \text{convective transport}\end{matrix}\right\}+\left\{\begin{matrix}\text{rate of energy in by}\\ \text{molecular transport}\end{matrix}\right\}-\left\{\begin{matrix}\text{rate of energy out by}\\ \text{molecular transport}\end{matrix}\right\}$$
$$+\left\{\begin{matrix}\text{rate of energy in by}\\ \text{radiation}\end{matrix}\right\}-\left\{\begin{matrix}\text{rate of energy out by}\\ \text{radiation}\end{matrix}\right\}+\left\{\begin{matrix}\text{rate of energy addition}\\ \text{by chemical reaction}\end{matrix}\right\}=\left\{\begin{matrix}\text{rate of increace}\\ \text{of energy}\end{matrix}\right\}$$

(B.1)

Based on the conservation of energy in equation (B.1) and inputs and outputs shown in Figure B.1, and assuming that the reaction occurs just in the solid phase, we get the following equation for heat transfer in the packed-bed reactor

$$q'_z\varepsilon_b A_z|_z - q'_z\varepsilon_b A_z|_{z+\Delta z} + q_z A_z|_z - q_z A_z|_{z+\Delta z} + q_r A_r|_r - q_r A_r|_{r+\Delta r}$$
$$+q''_z A_z|_z - q''_z A_z|_{z+\Delta z} + q''_r A_r|_r - q''_r A_r|_{r+\Delta r} - \sum_{i=1}^{N} r_i \Delta H_i \rho_s (1-\varepsilon_b)\Delta V = \frac{\partial E}{\partial t}, \qquad \text{(B.2)}$$

where ε_b is bed void fraction, E is internal energy of the element (consists of both solid and gas) and ρ_s is the density of particles. A_z and A_r are the areas normal to z and r coordinates. Substituting corresponding values of A_z, A_r, ΔV and E

$$\begin{aligned} &q'_z\varepsilon_b(2\pi r\Delta r)|_z - q'_z\varepsilon_b(2\pi r\Delta r)|_{z+\Delta z} + q_z(2\pi r\Delta r)|_z - q_z(2\pi r\Delta r)|_{z+\Delta z} + q_r(2\pi r\Delta z)|_r \\ &- q_r(2\pi r\Delta z)|_{r+\Delta r} + q''_z(2\pi r\Delta r)|_z - q''_z(2\pi r\Delta r)|_{z+\Delta z} + q''_r(2\pi r\Delta z)|_r - q''_r(2\pi r\Delta z)|_{r+\Delta r} \\ &- \sum_{i=1}^{N} r_i\Delta H_i\rho_s(1-\varepsilon_b)(2\pi r\Delta z\Delta r) = \frac{\partial(2\pi r\Delta z\Delta r(\varepsilon_b\rho_g c_{p,g} + (1-\varepsilon_b)\rho_s c_{p,s})T)}{\partial t} \end{aligned} \quad \text{(B.3)}$$

where ρ_g and ρ_s are gas and solid particle densities, $c_{p,g}$ and $c_{p,s}$ are specific heat capacity of the gas and solid at constant pressure. Considering densities, specific heats, and void fraction to be constant in z and r directions and dividing the equation above by $2\pi r\Delta r\Delta z$

$$\begin{aligned} &\varepsilon_b\frac{q'_z|_z - q'_z|_{z+\Delta z}}{\Delta z} + \frac{q_z|_z - q_z|_{z+\Delta z}}{\Delta z} + \frac{1}{r}\frac{q_r r|_r - q_r r|_{r+\Delta r}}{\Delta r} + \frac{q''_z|_z - q''_z|_{z+\Delta z}}{\Delta z} \\ &+ \frac{1}{r}\frac{q''_r r|_r - q''_r r|_{r+\Delta r}}{\Delta r} - \sum_{i=1}^{N} r_i\Delta H_i\rho_s(1-\varepsilon_b) = (\varepsilon_b\rho_g c_{p,g} + (1-\varepsilon_b)\rho_s c_{p,s})\frac{\partial T}{\partial t}. \end{aligned} \quad \text{(B.4)}$$

Taking limits and allowing the dimensions of the volume element to become infinitesimally small for each term we have

$$\begin{aligned} &\lim_{\Delta z\to 0}\frac{q'_z|_z - q'_z|_{z+\Delta z}}{\Delta z} = -\frac{\partial q'_z}{\partial z},\ \lim_{\Delta z\to 0}\frac{q_z|_z - q_z|_{z+\Delta z}}{\Delta z} = -\frac{\partial q_z}{\partial z},\ \lim_{\Delta r\to 0}\frac{q_r r|_r - q_r r|_{r+\Delta r}}{\Delta r} = -\frac{\partial(q_r.r)}{\partial r} \\ &\lim_{\Delta z\to 0}\frac{q''_z|_z - q''_z|_{z+\Delta z}}{\Delta z} = -\frac{\partial q''_z}{\partial z},\ \lim_{\Delta r\to 0}\frac{q''_r r|_r - q''_r r|_{r+\Delta r}}{\Delta r} = -\frac{\partial(q''_r.r)}{\partial r} \end{aligned}$$

(B.5)

Substituting into equation (B.4), we have the differential form of the energy equation

$$\begin{aligned} &-\varepsilon_b\frac{\partial q'_z}{\partial z} - \frac{\partial q_z}{\partial z} - \frac{1}{r}\frac{\partial(q_r.r)}{\partial r} - \frac{\partial q''_z}{\partial z} - \frac{1}{r}\frac{\partial(q''_r.r)}{\partial r} - \sum_{i=1}^{N} r_i\Delta H_i\rho_s(1-\varepsilon_b) \\ &= (\varepsilon_b\rho_g c_{p,g} + (1-\varepsilon_b)\rho_s c_{p,s})\frac{\partial T}{\partial t}. \end{aligned} \quad \text{(B.6)}$$

Convective heat transfer is considered to be $q' = \rho c_p u T$. For the conductive heat transfer, Fourier's law is used ($q = -k_c.\nabla T$). In terms of the radiative heat transfer, a simple but accurate approximation called the diffusion approximation (also called Rosseland approximation)[102] is employed as we are dealing with an optically thick medium. Based on this approximation, $q'' = -k_r.\nabla T$, where k_r is radiative conductivity. Therefore

$$-\varepsilon_b \rho_g c_{p,g} u_z \frac{\partial T}{\partial z} + \frac{\partial}{\partial z}[(k_{c,z} + k_{r,z})\frac{\partial T}{\partial z}] + \frac{1}{r}\frac{\partial}{\partial r}[(k_{c,r} + k_{r,r}) r \frac{\partial T}{\partial r}] - \sum_{i=1}^{N} r_i \Delta H_i \rho_s (1-\varepsilon_b) = (\varepsilon_b \rho_g c_{p,g} + (1-\varepsilon_b)\rho_s c_{p,s})\frac{\partial T}{\partial t}. \quad \text{(B.7)}$$

$k_{c,z}$ and $k_{r,z}$ are thermal conductivity due to conduction and radiation in z direction, $k_{c,r}$ and $k_{r,r}$ are thermal conductivity due to conduction and radiation in r direction. It should be mentioned that all of these parameters are effective parameters since they are defined for a porous medium with the assumption that solid particles and the gas phase is considered a homogenous continuum medium.

To simplify the energy equation, we introduce a total effective thermal conductivity term (k_{eff}) which includes thermal conductivity due to both radiation and conduction. For a system with constant bed properties in r and z directions, this term can be considered the same in both directions. Furthermore, superficial gas velocity is usually used instead of real gas velocity ($u_z^s = \varepsilon_b u_z$)

$$-\rho_g c_{p,g} u_z^s \frac{\partial T}{\partial z} + \frac{\partial}{\partial z}(k_{eff}\frac{\partial T}{\partial z}) + \frac{1}{r}\frac{\partial}{\partial r}(k_{eff} r \frac{\partial T}{\partial r}) - \sum_{i=1}^{N} r_i \Delta H_i \rho_s (1-\varepsilon_b) = (\varepsilon_b \rho_g c_{p,g} + (1-\varepsilon_b)\rho_s c_{p,s})\frac{\partial T}{\partial t}. \quad \text{(B.8)}$$

Appendix C, local thermal equilibrium (LTE) assumption

In this thesis we have assumed local thermal equilibrium (LTE)—the solid and gas are the same temperature at every location. The LTE assumption is valid only when the temperature difference between the solid phase and the gas phase in an elementary volume is much smaller than that occurring over the system dimension [82, 103]; we believe this to be satisfied at all times except the very early transients of the experiment since a temperature difference of over 100 °C is established in the bed. Further, a general criterion for the validity of the LTE assumption in terms of engineering parameters including the Darcy number, the Prandtl number, the Nusselt number, and the Reynolds number has been proposed by Kim and Jang [82],

$$\mathrm{Pr}.\mathrm{Re}.\mathrm{Da}^{1/2}.\frac{\varepsilon}{\mathrm{Nu}} << 1, \tag{C.1}$$

where the dimensionless numbers are defined as

$$\mathrm{Pr} = \frac{\nu}{\alpha}, \qquad \mathrm{Re} = \frac{u d_p}{\nu}, \qquad \mathrm{Da} = \frac{d_p^2}{L^2}, \qquad \mathrm{Nu} = \frac{h_{sg} d_p}{k_g}. \tag{C.2}$$

The definitions of these quantities and estimates or precise values for them are given in a table below. The solid–gas heat transfer coefficient represents the value with the most uncertainty of the values needed to check equation (C.1). It was estimated by $h_{sg} = \frac{k_g}{d_p}(2 + 0.6\,\mathrm{Re}^{1/2}.\mathrm{Pr}^{1/3})$ [104].

We believe this to represent a conservative choice. A value of 1.4×10^{-4} has been calculated for the left-hand side of equation (C.1) using the values in the table; LTE is clearly satisfied for the system.

Equation (C.1) shows that the validity of LTE depends on the characteristics of the gas, solid, and the reactor. If Re, Pr, or Da numbers increase enough, or Nu decreases enough, the LTE condition may not apply anymore.

The maximum Reynolds number allowed for the system under the LTE assumption has been calculated as 130 by considering the left-hand side of equation (C.1) equal to 0.1. The corresponding gas flow rate would be 100000 mL/min, 1000 times more than the current gas flow rate.

Table C.1: Values of the parameters in equation (C.1)

Symbol	Meaning	Value	Source
d_p	particle diameter (m)	$(0.5-1)\times10^{-3}$	measurement
h_{sg}	solid-gas heat transfer coefficient (W/m^2.K)	216.3	Bird et al. [104]
k_g	gas thermal conductivity (W/m.K)	$(45-55)\times10^{-3}$	Saxena [90]
L	characteristic length scale of the system (m)	3×10^{-2}	measurement
u	velocity (m/s)	$(16-22)\times10^{-3}$	Bird et al. [104]
ρ_s	mass density of the solid phase (kg/m^3)	5×1000	measurement
ε	bed void fraction (-)	0.39	Roshani [88]
α	gas thermal diffusivity (m^2/s)	$(1.2-2.6)\times10^{-4}$	Saxena [90]
ν	gas kinematic viscosity (m^2/s)	$(1.5-2.3)\times10^{-4}$	engineeringtoolbox.com

Appendix D, 2D mass transfer model derivation for a packed-bed reactor

A shell balance method is employed to derive a dynamic pseudo-homogenous two-dimensional mass transfer model for a vertical packed-bed reactor. Figure D.1 shows mass transport of component i in the gas phase, where j_i and j_i' are diffusive (molecular) and convective molar fluxes for component i, respectively:

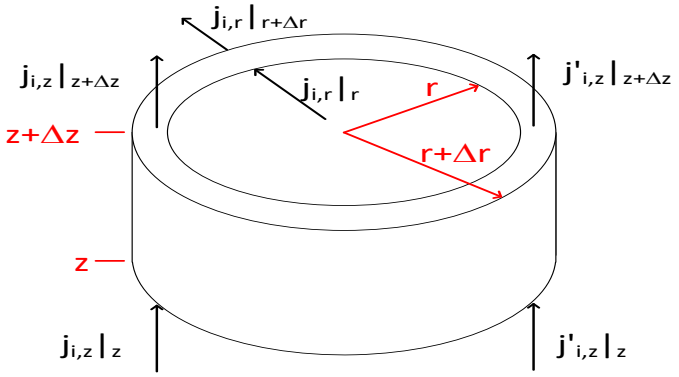

Figure D.1 Mass transport in the packed-bed reactor element

Applying the law of conservation of mass to the elemental volume for a dynamic system, for component i, per unit volume we have

$$\left\{\begin{matrix}\text{rate of mole of } i \text{ in by}\\ \text{convective transport}\end{matrix}\right\}-\left\{\begin{matrix}\text{rate of mole of } i \text{ out by}\\ \text{convective transport}\end{matrix}\right\}+\left\{\begin{matrix}\text{rate of mole of } i \text{ in by}\\ \text{molecular transport}\end{matrix}\right\}$$
$$-\left\{\begin{matrix}\text{rate of mole of } i \text{ out by}\\ \text{molecular transport}\end{matrix}\right\}+\left\{\begin{matrix}\text{rate of mole of } i \text{ added}\\ \text{by chemical reaction}\end{matrix}\right\}=\left\{\begin{matrix}\text{rate of increace}\\ \text{of mole of } i\end{matrix}\right\} \qquad \text{(D.1)}$$

Based on the conservation of mass in equation (D.1) and inputs and outputs shown in Figure D.1

$$j'_{i,z}\varepsilon_b A_z\,|_z - j'_{i,z}\varepsilon_b A_z\,|_{z+\Delta z} + j_{i,z}\varepsilon_b A_z\,|_z - j_{i,z}\varepsilon_b A_z\,|_{z+\Delta z} + j_{i,r}\varepsilon_b A_r\,|_r - j_{i,r}\varepsilon_b A_r\,|_{r+\Delta r}$$
$$+\rho_s \Delta V_s r_i = \frac{\partial\left(C_i \Delta V_g\right)}{\partial t} \qquad \text{(D.2)}$$

where ε_b is bed void fraction, ρ_s is the density of particles, V_s and V_g are the volume of solid and gas in the element, r_i is the reaction rate for component i, and C_i is concentration of component i in the gas phase.

Substituting corresponding values of A_z, A_r, ΔV_s and ΔV_g

$$j'_{i,z}\varepsilon_b(2\pi r\Delta r)|_z - j'_{i,z}\varepsilon_b(2\pi r\Delta r)|_{z+\Delta z} + j_{i,z}\varepsilon_b(2\pi r\Delta r)|_z - j_{i,z}\varepsilon_b(2\pi r\Delta r)|_{z+\Delta z}$$
$$+ j_{i,r}\varepsilon_b(2\pi r\Delta z)|_r - j_{i,r}\varepsilon_b(2\pi r\Delta z)|_{r+\Delta r} + \rho_s(1-\varepsilon_b)2\pi r\Delta r\Delta z r_j = \frac{\partial(C_i\varepsilon_b 2\pi r\Delta r\Delta z)}{\partial t} \quad \text{(D.3)}$$

Considering void fraction to be constant in both z and r directions and dividing the equation above by $2\pi r\Delta r\Delta z$

$$\varepsilon_b\frac{j'_{i,z}|_z - j'_{i,z}|_{z+\Delta z}}{\Delta z} + \varepsilon_b\frac{j_{i,z}|_z - j_{i,z}|_{z+\Delta z}}{\Delta z} + \varepsilon_b\frac{1}{r}\frac{j_{i,r}r|_r - j_{i,r}r|_{r+\Delta r}}{\Delta r} + \rho_s(1-\varepsilon_b)r_j = \varepsilon_b\frac{\partial C_i}{\partial t} \quad \text{(D.4)}$$

Taking limits and allowing the dimensions of the volume element to become infinitesimally small

$$\lim_{\Delta z\to 0}\frac{j'_{i,z}|_z - j'_{i,z}|_{z+\Delta z}}{\Delta z} = -\frac{\partial j'_{i,z}}{\partial z},\ \lim_{\Delta z\to 0}\frac{j_{i,z}|_z - j_{i,z}|_{z+\Delta z}}{\Delta z} = -\frac{\partial j_{i,z}}{\partial z},$$
$$\lim_{\Delta r\to 0}\frac{j_{i,r}r|_r - j_{i,r}r|_{r+\Delta r}}{\Delta r} = -\frac{\partial(j_{i,r}.r)}{\partial r} \quad \text{(D.5)}$$

Substituting into equation (D.4), we have the differential form of the mass equation

$$-\varepsilon_b\frac{\partial j'_{i,z}}{\partial z} - \varepsilon_b\frac{\partial j_{i,z}}{\partial z} - \varepsilon_b\frac{1}{r}\frac{\partial(j_{i,r}.r)}{\partial r} + \rho_s(1-\varepsilon_b)r_j = \varepsilon_b\frac{\partial C_i}{\partial t} \quad \text{(D.6)}$$

Convective mass transfer is considered to be $j'_i = uC_i$. For molecular mass transfer, Fick's law is used ($j_i = -D_{im}.\nabla C_i$). Therefore,

$$-\varepsilon_b\frac{\partial(u_z C_i)}{\partial z} - \varepsilon_b\frac{\partial(-D_{im}\frac{\partial C_i}{\partial z})}{\partial z} - \varepsilon_b\frac{1}{r}\frac{\partial(-D_{im}\frac{\partial C_i}{\partial r}.r)}{\partial r} + \rho_s(1-\varepsilon_b)r_j = \varepsilon_b\frac{\partial C_i}{\partial t} \quad \text{(D.7)}$$

Where D_{im} is diffusivity of component *i* in the gas mixture. Using superficial gas velocity instead of real gas velocity ($u_z^s = \varepsilon_b u_z$) and assuming it to be constant

$$-u_z^s \frac{\partial C_i}{\partial z} + \varepsilon_b \frac{\partial}{\partial z}(D_{im} \frac{\partial C_i}{\partial z}) + \varepsilon_b \frac{1}{r} \frac{\partial}{\partial r}(r D_{im} \frac{\partial C_i}{\partial r}) + \rho_s (1-\varepsilon_b) r_j = \varepsilon_b \frac{\partial C_i}{\partial t} \qquad \text{(D.8)}$$

Appendix E, effective thermal conductivity correlations from literature

Deissler and Boegli[91]

maximum effective thermal conductivity

$$\frac{k_{eff}^{\max}}{k_g} = \varepsilon_b + (1-\varepsilon_b)K \qquad \text{(E.1)}$$

and minimum effective thermal conductivity

$$\frac{k_{eff}^{\min}}{k_g} = \frac{1}{\varepsilon_b + (1-\varepsilon_b)/K} \ , \qquad \text{(E.2)}$$

where $K = \frac{k_s}{k_g}$.

Breitbach and Barthels (1980)[92]

$$F_E^* = \left(1-\sqrt{1-\varepsilon_b}\right)\varepsilon_b + \frac{\sqrt{1-\varepsilon_b}}{\frac{2}{\varepsilon_{r,s}}-1} \times \frac{B+1}{B} \times \frac{1}{1+\frac{1}{\left(\frac{2}{\varepsilon_{r,s}}-1\right)\Lambda_f}} \ , \qquad \text{(E.3)}$$

where

$$B = 1.25\left((1-\varepsilon_b)/\varepsilon_b\right)^{10/9} \qquad \text{(E.4)}$$

and Λ_f is a dimensionless solid conductivity

$$\Lambda_f = k_s / 4 d_p \sigma T^3 . \tag{E.5}$$

Kunii and Smith (1960)[93]

$$\frac{k_{eff}}{k_g} = \varepsilon_b \left[1 + \beta \frac{h_{rv} . d_p}{k_g} \right] + \frac{\beta (1 - \varepsilon_b)}{\dfrac{1}{\dfrac{1}{\Phi} + \dfrac{d_p . h_{rs}}{k_g}} + \dfrac{\gamma}{K}} , \tag{E.6}$$

where h_{rs} is the particle to particle radiative heat transfer coefficient

$$h_{rs} = 4 \sigma T^3 \left[\frac{\varepsilon_{r,s}}{2 - \varepsilon_{r,s}} \right], \tag{E.7}$$

and h_{rv} is void to particle heat transfer coefficient

$$h_{rv} = 4 \sigma T^3 / \left[1 + \frac{\varepsilon_b}{2(1 - \varepsilon_b)} \frac{(1 - \varepsilon_{r,s})}{\varepsilon_{r,s}} \right]. \tag{E.8}$$

β is a factor defined as the ratio of the average length between the centres of two neighbouring particles to the particle diameter. This parameter ranges from 0.9 to 1 for almost all actual packed beds. Due to the random packing of the particles, a value of 0.9 is assumed. γ is the ratio of the length of solid affected by thermal conductivity to particle diameter and has a value of 2/3.

The empirical constant Φ is a function of the number of contacts responsible for the heat transfer

$$\Phi = \Phi_2 + (\Phi_1 - \Phi_2) \frac{\varepsilon_b - \varepsilon_{b,2}}{\varepsilon_{b,1} - \varepsilon_{b,2}} . \tag{E.9}$$

Φ_1 and Φ_2 represents two extreme cases of the void fraction where $\varepsilon_{b,1} = 0.476$ and $\varepsilon_{b,2} = 0.26$.

$$\Phi_i = \frac{0.5(\frac{K-1}{K})^2 \sin^2 \theta_i}{\ln(K-(K-1)\cos\theta_i) - \frac{K-1}{K}(1-\cos\theta_i)} - \frac{2}{3K} \qquad \text{(E.10)}$$

with $K = k_s / k_g$ and $\sin^2 \theta_i = 1/n_i$. n is the number of the contact points of a particle with $n_1 = 1.5$ and $n_2 = 4\sqrt{3}$.

References

1. Esence, T.; Bruch, A.; Molina, S.; Stutz, B.; Fourmigué, J.-F., A review on experience feedback and numerical modeling of packed-bed thermal energy storage systems. *Solar Energy* **2017,** 153, 628-654.

2. Rydén, M.; Leion, H.; Mattisson, T.; Lyngfelt, A., Combined oxides as oxygen-carrier material for chemical-looping with oxygen uncoupling. *Applied Energy* **2014,** 113, 1924–1932.

3. Go, K. S.; Son, S. R.; Kim, S. D., Reaction kinetics of reduction and oxidation of metal oxides for hydrogen production. *International Journal of Hydrogen Energy* **2008,** 33, (21), 5986-5995.

4. Chueh, W. C.; Falter, C.; Abbott, M.; Scipio, D.; Furler, P.; Haile, S. M.; Steinfeld, A., High-Flux Solar-Driven Thermochemical Dissociation of CO_2 and H_2O Using Nonstoichiometric Ceria. *Science* **2010,** 330, (6012), 1797-1801.

5. Furler, P.; Scheffe, J.; Gorbar, M.; Moes, L.; Vogt, U.; Steinfeld, A., Solar Thermochemical CO_2 Splitting Utilizing a Reticulated Porous Ceria Redox System. *Energy & Fuels* **2012,** 26, (11), 7051-7059.

6. Keunecke, M.; Meier, A.; Palumbo, R., Solar thermal decomposition of zinc oxide: an initial investigation of the recombination reaction in the temperature range 1100–1250K. *Chemical Engineering Science* **2004,** 59, (13), 2695-2704.

7. Abanades, S.; Flamant, G., Thermochemical hydrogen production from a two-step solar-driven water-splitting cycle based on cerium oxides. *Solar Energy* **2006,** 80, (12), 1611-1623.

8. Romero, M.; Steinfeld, A., Concentrating solar thermal power and thermochemical fuels. *Energy & Environmental Science* **2012,** 5, (11), 9234-9245.

9. Castillo-Araiza, C. O.; Jiménez-Islas, H.; López-Isunza, F., Heat-Transfer Studies in Packed-Bed Catalytic Reactors of Low Tube/Particle Diameter Ratio. *Industrial & Engineering Chemistry Research* **2007,** 46, (23), 7426-7435.

10. Wen, D.; Ding, Y., Heat transfer of gas flow through a packed bed. *Chemical Engineering Science* **2006,** 61, (11), 3532-3542.

11. Lipiński, W.; Bader, R.; Pye, J.; Coventry, J.; Steinfeld, A.; Weimer, A.; Lovegrove, K., High-temperature solar thermal energy storage via manganese-oxide based redox cycling. In Australian Renewable Energy Agency: 2014.

12. Al-Shankiti, I. A.; Ehrhart, B. D.; Ward, B. J.; Bayon, A.; Wallace, M. A.; Bader, R.; Kreider, P.; Weimer, A. W., Particle design and oxidation kinetics of iron-manganese oxide redox materials for thermochemical energy storage. *Solar Energy* **2019,** 183, 17-29.

13. Goswami, D. Y., *Principles of Solar Engineering*. 3rd ed.; Taylor and Francis Group: 2015.

14. Holman, J. P., *Heat Transfer*. 10th ed.; McGraw-Hill: 2010.

15. Romero, M.; González-Aguilar, J., Solar thermal CSP technology. *Wiley Interdisciplinary Reviews: Energy and Environment* **2014,** 3, (1), 42–59.

16. Blanco, M. J.; Santigosa, L. R., *Advances in Concentrating Solar Thermal Research and Technology*. Woodhead Publishing: 2017.

17. Lovegrove, K.; Stein, W., *Concentrating Solar Power Technology*. Woodhead Publishing: 2012.

18. Chen, X.; Zhang, Z.; Qi, C.; Ling, X.; Peng, H., State of the art on the high-temperature thermochemical energy storage systems. *Energy Conversion and Management* **2018,** 177, 792-815.

19. Liu, D.; Xin-Feng, L.; Bo, L.; Si-quan, Z.; Yan, X., Progress in thermochemical energy storage for concentrated solar power: A review. *International Journal of Energy Research* **2018,** 42, (15), 4546-4561.

20. Prieto, C.; Cooper, P.; Fernández, A. I.; Cabeza, L. F., Review of technology: Thermochemical energy storage for concentrated solar power plants. *Renewable and Sustainable Energy Reviews* **2016,** 60, 909–929.

21. Nithyanandam, K.; Stekli, J.; Pitchumani, R., 10 - High-temperature latent heat storage for concentrating solar thermal (CST) systems. In *Advances in Concentrating Solar Thermal Research and Technology*, Blanco, M. J.; Santigosa, L. R., Eds. Woodhead Publishing: 2017; pp 213-246.

22. Irwin, L.; Stekli, J.; Pfefferkorn, C.; Pitchumani, R., 11 - Thermochemical energy storage for concentrating solar thermal (CST) systems. In *Advances in Concentrating Solar Thermal Research and Technology*, Blanco, M. J.; Santigosa, L. R., Eds. Woodhead Publishing: 2017; pp 247-267.

23. Wu, S.; Zhou, C.; Doroodchi, E.; Nellore, R.; Moghtaderi, B., A review on high-temperature thermochemical energy storage based on metal oxides redox cycle. *Energy Conversion and Management* **2018,** 168, 421-453.

24. Block, T.; Schmücker, M., Metal oxides for thermochemical energy storage: A comparison of several metal oxide systems. *Solar Energy* **2016,** 126, 195–207.

25. Agrafiotis, C.; Roeb, M.; Sattler, C., Exploitation of thermochemical cycles based on solid oxide redox systems for thermochemical storage of solar heat. Part 4: Screening of oxides for use in cascaded thermochemical storage concepts. *Solar Energy* **2016,** 139, 695-710.

26. Dizaji, H. B.; Hosseini, H., A review of material screening in pure and mixed-metal oxide thermochemical energy storage (TCES) systems for concentrated solar power (CSP) applications. *Renewable and Sustainable Energy Reviews* **2018,** 98, 9-26.

27. Wentworth, W. E.; Chen, E., Simple thermal decomposition reactions for storage of solar thermal energy. *Solar Energy* **1976,** 18, (3), 205-214.

28. Fahim, M. A.; Ford, J. D., Energy storage using the BaO_2 BaO reaction cycle. *The Chemical Engineering Journal* **1983,** 27, (1), 21-28.

29. Chadda, D.; Ford, J. D.; Fahim, M. A., Chemical energy storage by the reaction cycle CuO/Cu2O. *International Journal of Energy Research* **1989,** 13, (1), 63-73.

30. Carrillo, A. J.; Sastre, D.; Serrano, D. P.; Pizarro, P.; Coronado, J. M., Revisiting the BaO_2/BaO redox cycle for solar thermochemical energy storage. *Physical Chemistry Chemical Physics* **2016,** 18, (11), 8039-8048.

31. Agrafiotis, C.; Roeb, M.; Schmücker, M.; Sattler, C., Exploitation of thermochemical cycles based on solid oxide redox systems for thermochemical storage of solar heat. Part 1: Testing of cobalt oxide-based powders. *Solar Energy* **2014,** 102, 189-211.

32. Agrafiotis, C.; Roeb, M.; Schmücker, M.; Sattler, C., Exploitation of thermochemical cycles based on solid oxide redox systems for thermochemical storage of solar heat. Part 2: Redox oxide-coated porous ceramic structures as integrated thermochemical reactors/heat exchangers. *Solar Energy* **2015,** 114, 440-458.

33. Agrafiotis, C.; Tescari, S.; Roeb, M.; Schmücker, M.; Sattler, C., Exploitation of thermochemical cycles based on solid oxide redox systems for thermochemical storage of solar heat. Part 3: Cobalt oxide monolithic porous structures as integrated thermochemical reactors/heat exchangers. *Solar Energy* **2015,** 114, 459-475.

34. Block, T.; Knoblauch, N.; Schmücker, M., The cobalt-oxide/iron-oxide binary system for use as high temperature thermochemical energy storage material. *Thermochimica Acta* **2014,** 577, 25-32.

35. Pagkoura, C.; Karagiannakis, G.; Zygogianni, A.; Lorentzou, S.; Kostoglou, M.; Konstandopoulos, A. G.; Rattenburry, M.; Woodhead, J. W., Cobalt oxide based structured bodies as redox thermochemical heat storage medium for future CSP plants. *Solar Energy* **2014,** 108, 146-163.

36. Karagiannakis, G.; Pagkoura, C.; Halevas, E.; Baltzopoulou, P.; Konstandopoulos, A. G., Cobalt/cobaltous oxide based honeycombs for thermochemical heat storage in future concentrated solar power installations: Multi-cyclic assessment and semi-quantitative heat effects estimations. *Solar Energy* **2016,** 133, 394-407.

37. Schrader, A. J.; Muroyama, A. P.; Loutzenhiser, P. G., Solar electricity via an Air Brayton cycle with an integrated two-step thermochemical cycle for heat storage based on Co_3O_4/CoO redox reactions: Thermodynamic analysis. *Solar Energy* **2015,** 118, 485-495.

38. Karagiannakis, G.; Pagkoura, C.; Zygogianni, A.; Lorentzou, S.; Konstandopoulos, A. G., Monolithic Ceramic Redox Materials for Thermochemical Heat Storage Applications in CSP Plants. *Energy Procedia* **2014,** 49, 820-829.

39. Carrillo, A. J.; Serrano, D. P.; Pizarro, P.; Coronado, J. M., Thermochemical heat storage based on the Mn_2O_3/Mn_3O_4 redox couple: influence of the initial particle size on the morphological evolution and cyclability. *Journal of Materials Chemistry A* **2014,** 2, (45), 19435–19443.

40. Carrillo, A. J.; Moya, J.; Bayón, A.; Jana, P.; de la Peña O'Shea, V. A.; Romero, M.; Gonzalez-Aguilar, J.; Serrano, D. P.; Pizarro, P.; Coronado, J. M., Thermochemical energy storage at high temperature via redox cycles of Mn and Co oxides: Pure oxides versus mixed ones. *Solar Energy Materials and Solar Cells* **2014,** 123, 47–57.

41. Carrillo, A. J.; Serrano, D. P.; Pizarro, P.; Coronado, J. M., Manganese oxide-based thermochemical energy storage: Modulating temperatures of redox cycles by Fe–Cu co-doping. *Journal of Energy Storage* **2016,** 5, 169–176.

42. Carrillo, A. J.; Serrano, D. P.; Pizarro, P.; Coronado, J. M., Improving the Thermochemical Energy Storage Performance of the Mn_2O_3/Mn_3O_4 Redox Couple by the Incorporation of Iron. *ChemSusChem* **2015,** 8, (11), 1947–1954.

43. Droege, P.; Carrillo, A. J.; Serrano, D. P.; Pizarro, P.; Coronado, J. M., 9th International Renewable Energy Storage Conference, IRES 2015Thermochemical Heat Storage at High Temperatures using Mn_2O_3/Mn_3O_4 System: Narrowing the Redox Hysteresis by Metal Co-doping. *Energy Procedia* **2015,** 73, 263–271.

44. Wong, B., thermochemical heat storage for concentrated solar power, Final Report for the US Department of Energy, San Diego, CA, USA. **2011**.

45. Alonso, E.; Pérez-Rábago, C.; Licurgo, J.; Fuentealba, E.; Estrada, C. A., First experimental studies of solar redox reactions of copper oxides for thermochemical energy storage. *Solar Energy* **2015,** 115, 297-305.

46. Babiniec, S. M.; Coker, E. N.; Miller, J. E.; Ambrosini, A., Doped calcium manganites for advanced high-temperature thermochemical energy storage. *International Journal of Energy Research* **2016,** 40, (2), 280-284.

47. Babiniec, S. M.; Coker, E. N.; Miller, J. E.; Ambrosini, A., Investigation of $La_xSr_{1-x}Co_yM_{1-y}O_{3-\delta}$ (M = Mn, Fe) perovskite materials as thermochemical energy storage media. *Solar Energy* **2015,** 118, 451-459.

48. Imponenti, L.; Albrecht, K. J.; Braun, R. J.; Jackson, G. S. In *Measuring thermochemical energy storage capacity with redox cycles of doped-$CaMnO_3$*, ECS Transactions, 2016; 2016; pp 11-22.

49. Zhang, Z.; Andre, L.; Abanades, S., Experimental assessment of oxygen exchange capacity and thermochemical redox cycle behavior of Ba and Sr series perovskites for solar energy storage. *Solar Energy* **2016,** 134, 494-502.

50. Agrafiotis, C.; Roeb, M.; Sattler, C., Exploitation of thermochemical cycles based on solid oxide redox systems for thermochemical storage of solar heat. Part 4: Screening of oxides for use in cascaded thermochemical storage concepts. *Solar Energy*, in press.

51. Bale, C. W.; Chartrand, P.; Decterov, S. A.; Eriksson, G.; Hack, K.; Ben Mahfoud, R.; Melançon, J.; Pelton, A. D.; Petersen, S., FactSage Thermochemical Software and Databases. *Calphad Journal* **2002,** 62, 189–228.

52. Marugán, J.; Botas, J. A.; Martín, M.; Molina, R.; Herradón, C., Study of the first step of the Mn_2O_3/MnO thermochemical cycle for solar hydrogen production. *International Journal of Hydrogen Energy* **2012,** 37, (8), 7017–7025.

53. Perkins, C.; Weimer, A. W., Likely near-term solar-thermal water splitting technologies. *International Journal of Hydrogen Energy* **2004,** 29, (15), 1587–1599.

54. Charvin, P.; Abanades, S.; Lemort, F.; Flamant, G., Hydrogen Production by Three-Step Solar Thermochemical Cycles Using Hydroxides and Metal Oxide Systems. *Energy & Fuels* **2007,** 21, (5), 2919–2928.

55. Grundy, A. N.; Hallstedt, B.; Gauckler, L. J., Assessment of the Mn-O system. *Journal of Phase Equilibria* **2003,** 24, (1), 21–39.

56. Kjellqvist, L.; Selleby, M., Thermodynamic Assessment of the Fe-Mn-O System. *Journal of Phase Equilibria and Diffusion* **2010,** 31, (2), 113–134.

57. Crum, J. V.; Riley, B. J.; Vienna, J. D., Binary Phase Diagram of the Manganese Oxide–Iron Oxide System. *Journal of the American Ceramic Society* **2009,** 92, (10), 2378–2384.

58. M.W., C., NIST-JANAF thermochemical tables, 4th ed. **1998**.

59. Monazam, E. R.; Breault, R. W.; Siriwardane, R., Kinetics of magnetite (Fe3O4) oxidation to hematite (Fe2O3) in air for chemical looping combustion. *Industrial and Engineering Chemistry Research* **2014,** 53, (34), 13320-13328.

60. Solé, A.; Martorell, I.; Cabeza, L. F., State of the art on gas–solid thermochemical energy storage systems and reactors for building applications. *Renewable and Sustainable Energy Reviews* **2015,** 47, 386-398.

61. Pan, Z. H.; Zhao, C. Y., Gas–solid thermochemical heat storage reactors for high-temperature applications. *Energy* **2017,** 130, 155-173.

62. Wokon, M.; Kohzer, A.; Linder, M., Investigations on thermochemical energy storage based on technical grade manganese-iron oxide in a lab-scale packed bed reactor. *Solar Energy* **2017,** 153, 200-214.

63. Preisner, N. C.; Block, T.; Linder, M.; Leion, H., Stabilizing Particles of Manganese-iron Oxide with Additives for Thermochemical Energy Storage. *Energy Technology* **2018,** 6, (11), 2154-2165.

64. Zanganeh, G.; Pedretti, A.; Zavattoni, S.; Barbato, M.; Steinfeld, A., Packed-bed thermal storage for concentrated solar power – Pilot-scale demonstration and industrial-scale design. *Solar Energy* **2012,** 86, (10), 3084-3098.

65. Chung, J. D., Direct simulation of effective conductivity of porous silicon: Fourier treatments. *KSME International Journal* **1999,** 13, (10), 762-774.

66. Muhich, C. L.; Weston, K. C.; Arifin, D.; McDaniel, A. H.; Musgrave, C. B.; Weimer, A. W., Extracting Kinetic Information from Complex Gas–Solid Reaction Data. *Industrial & Engineering Chemistry Research* **2015,** 54, (16), 4113–4122.

67. Vyazovkin, S.; Burnham, A. K.; Criado, J. M.; Pérez-Maqueda, L. A.; Popescu, C.; Sbirrazzuoli, N., ICTAC Kinetics Committee recommendations for performing kinetic computations on thermal analysis data. *Thermochimica Acta* **2011,** 520, (1–2), 1–19.

68. Zhu, Y.; Al-ebbinni, N.; Henney, R.; Yi, C.; Barat, R., Extension to multiple temperatures of a three-reaction global kinetic model for methane dehydroaromatization. *Chemical Engineering Science* **2018,** 177, 132-138.

69. Khawam, A.; Flanagan, D. R., Solid-State Kinetic Models: Basics and Mathematical Fundamentals. *The Journal of Physical Chemistry B* **2006,** 110, (35), 17315–17328.

70. Vyazovkin, S.; Wight, C. A., Model-free and model-fitting approaches to kinetic analysis of isothermal and nonisothermal data. *Thermochimica Acta* **1999,** 340–341, 53–68.

71. Vyazovkin, S.; Dollimore, D., Linear and Nonlinear Procedures in Isoconversional Computations of the Activation Energy of Nonisothermal Reactions in Solids. *Journal of Chemical Information and Computer Sciences* **1996,** 36, (1), 42-45.

72. Ebrahimi-Kahrizsangi, R.; Abbasi, M. H., Evaluation of reliability of Coats-Redfern method for kinetic analysis of non-isothermal TGA. *Transactions of Nonferrous Metals Society of China* **2008,** 18, (1), 217-221.

73. Carrillo, A. J.; Serrano, D. P.; Pizarro, P.; Coronado, J. M., Understanding Redox Kinetics of Iron-Doped Manganese Oxides for High Temperature Thermochemical Energy Storage. *The Journal of Physical Chemistry C* **2016,** 120, (49), 27800-27812.

74. Wokon, M.; Block, T.; Nicolai, S.; Linder, M.; Schmücker, M., Thermodynamic and kinetic investigation of a technical grade manganese-iron binary oxide for thermochemical energy storage. *Solar Energy* **2017,** 153, 471-485.

75. André, L.; Abanades, S.; Cassayre, L., High-temperature thermochemical energy storage based on redox reactions using Co-Fe and Mn-Fe mixed metal oxides. *Journal of Solid State Chemistry* **2017,** 253, 6-14.

76. Azimi, G.; Leion, H.; Mattisson, T.; Lyngfelt, A., Chemical-looping with oxygen uncoupling using combined Mn-Fe oxides, testing in batch fluidized bed. *Energy Procedia* **2011,** 4, 370-377.

77. Bayon, A.; Bader, R.; Jafarian, M.; Fedunik-Hofman, L.; Sun, Y.; Hinkley, J.; Miller, S.; Lipiński, W., Techno-economic assessment of solid–gas thermochemical energy storage systems for solar thermal power applications. *Energy* **2018,** 149, 473-484.

78. Bale, C. W.; Chartrand, P.; Degterov, S. A.; Eriksson, G.; Hack, K.; Ben Mahfoud, R.; Melançon, J.; Pelton, A. D.; Petersen, S., FactSage thermochemical software and databases. *Calphad* **2002,** 26, (2), 189-228.

79. Amiri, A.; Ingram, G. D.; Maynard, N. E.; Livk, I.; Bekker, A. V., An Unreacted Shrinking Core Model for Calcination and Similar Solid-to-Gas Reactions. *Chemical Engineering Communications* **2015,** 202, (9), 1161-1175.

80. Levenspiel, O., *Chemical Reaction Engineering*. 3rd ed.; Wiley: New York, 1999.

81. Botas, J. A.; Marugán, J.; Molina, R.; Herradón, C., Kinetic modelling of the first step of Mn_2O_3/MnO thermochemical cycle for solar hydrogen production. *International Journal of Hydrogen Energy* **2012,** 37, (24), 18661–18671.

82. Kim, S. J.; Jang, S. P., Effects of the Darcy number, the Prandtl number, and the Reynolds number on local thermal non-equilibrium. *International Journal of Heat and Mass Transfer* **2002,** 45, (19), 3885-3896.

83. Gräf, I.; Ladenburger, G.; Kraushaar-Czarnetzki, B., Heat transport in catalytic sponge packings in the presence of an exothermal reaction: Characterization by 2D modeling of experiments. *Chemical Engineering Journal* **2016,** 287, 425-435.

84. Ferreira, L. n. M.; Castro, J. A. M.; Rodrigues, A. r. E., An analytical and experimental study of heat transfer in fixed bed. *International Journal of Heat and Mass Transfer* **2002,** 45, (5), 951-961.

85. van Antwerpen, W.; du Toit, C. G.; Rousseau, P. G., A review of correlations to model the packing structure and effective thermal conductivity in packed beds of mono-sized spherical particles. *Nuclear Engineering and Design* **2010,** 240, (7), 1803-1818.

86. Cheng, G. J.; Yu, A. B., Particle Scale Evaluation of the Effective Thermal Conductivity from the Structure of a Packed Bed: Radiation Heat Transfer. *Industrial & Engineering Chemistry Research* **2013,** 52, (34), 12202-12211.

87. Jorge, L. M. M.; Jorge, R. M. M.; Fojii, F.; Giudici, R., Evaluation of heat transfer in a catalytic fixed bed reactor at high temperatures. *Brazilian Journal of Chemical Engineering* **1999,** 16, 407-420.

88. Roshani, S. Elucidation of Local and Global Structural Properties of Packed Bed Configurations. The University of Leeds, 1990.

89. Takeda, M.; Onishi, T.; Nakakubo, S.; Fujimoto, S., Physical Properties of Iron-Oxide Scales on Si-Containing Steels at High Temperature. *MATERIALS TRANSACTIONS* **2009,** 50, (9), 2242-2246.

90. Saxena, S. C., Thermal conductivity of argon in the temperature range 350 to 2500 K AU - Chen, S.H.P. *Molecular Physics* **1975,** 29, (2), 455-466.

91. Deissler, R. G.; Boegli, J. S., An investigation of effective thermal conductivities of powders in various gases. *Trans. ASME* **1958,** 80, (7), 1417-1425.

92. Breitbach, G.; Barthels, H., Radiant heat transfer in the high temperature reactor core after failure of the afterheat removal systems. *Nuclear Technology* **1980,** 49, (3), 392-399.

93. Kunii, D.; Smith, J. M., Heat transfer characteristics of porous rocks. *AIChE Journal* **1960,** 6, (1), 71-78.

94. Bird, R.; Stewart, B. W. E.; Lightfoot, E. N., *Transport phenomena* 2nd ed.; John Wiley and Sons, Inc.: 2002.

95. Starink, M. J., Activation energy determination for linear heating experiments: deviations due to neglecting the low temperature end of the temperature integral. *Journal of Materials Science* **2007,** 42, (2), 483-489.

96. Starink, M. J., The determination of activation energy from linear heating rate experiments: a comparison of the accuracy of isoconversion methods. *Thermochimica Acta* **2003,** 404, (1–2), 163–176.

97. Aboulkas, A.; El Harfi, K., Study of the kinetics and mechanisms of thermal decomposition of moroccan tarfaya oil shale and its kerogen. *Oil Shale* **2008,** 25 (4), 426-443.

98. Noisong, P.; Danvirutai, C., Kinetics and Mechanism of Thermal Dehydration of KMnPO4·H2O in a Nitrogen Atmosphere. *Industrial & Engineering Chemistry Research* **2010,** 49, (7), 3146-3151.

99. Vyazovkin, S. V.; Lesnikovich, A. I., Estimation of the pre-exponential factor in the isoconversional calculation of effective kinetic parameters. *Thermochimica Acta* **1988,** 128, (Supplement C), 297-300.

100. Khawam, A.; Flanagan, D. R., Basics and Applications of Solid-State Kinetics: A Pharmaceutical Perspective. *Journal of Pharmaceutical Sciences* **2006,** 95, (3), 472-498.

101. Gotor, F. J.; Criado, J. M.; Malek, J.; Koga, N., Kinetic Analysis of Solid-State Reactions: The Universality of Master Plots for Analyzing Isothermal and Nonisothermal Experiments. *The Journal of Physical Chemistry A* **2000,** 104, (46), 10777–10782.

102. Howell, J. R.; Siegel, R.; Menguc, M. P., *Thermal Radiation Heat Transfer*. 5th ed.; Taylor and Francis Group: 2011.

103. Kaviany, M., *Principles of Heat Transfer in Porous Media*. Springer-Verlag: 1991.

104. Bird, R. B.; Stewart, W.; Lightfoot, E., *Transport phenomena*. 2nd ed.; Wiley: 2004.